One-Sided Ultrasonic Determination of Third Order Elastic Constants using Angle-Beam Acoustoelasticity Measurements

A Thesis
Presented to
the Academic Faculty

by

Dave D. Muir

In Partial Fulfillment
of the Requirements for the Degree
Doctor of Philosophy in the
School of Electrical and Computer Engineering

Georgia Institute of Technology
August 2009

One-Sided Ultrasonic Determination of Third Order Elastic Constants

using Angle-Beam Acoustoelasticity Measurements

Approved by:

Professor Thomas E. Michaels, Advisor
School of Electrical and Computer Engineering
Georgia Institute of Technology

Professor Jennifer E. Michaels, Co-Advisor
School of Electrical and Computer Engineering
Georgia Institute of Technology

Professor Massimo Ruzzene
School of Aerospace Engineering
Georgia Institute of Technology

Dr. Waymond R. Scott
School of Electrical and Computer Engineering
Georgia Institute of Technology

Dr. F. Levent Degertekin
School of Electrical and Computer Engineering
School of Mechanical Engineering
Georgia Institute of Technology

Professor Jianmin Qu
School of Mechanical Engineering
Georgia Institute of Technology

Date Approved: May 4, 2009

Dedicated to my step father (deceased) who did say I should go and do something big and believed in me. To my long time friend Arlene (deceased) who also encouraged me. Still have your text message! To all past teachers, and the glory of God.

ACKNOWLEDGEMENTS

This acknowledgement is going to be long. First I would like to thank our Lord and Savior Jesus Christ for providing the strength and many opportunities, surrounding me with the right people to see this thesis to completion. Special thanks to my dynamic advisor team of Professor Thomas E. Michaels and Professor Jennifer E. Michaels. Everyone says nice things about their advisors and you're like yeah yeah. But seriously it was a great opportunity to work with them and I've learnt a lot. They are admired in the community and I can see why as they showed great interest in my work and overall development and provided good leadership when I tended to go off on bunny trails as they say. One encouraging moment which stood out for me was after marking up a draft they took out their own old thesis and showed where they got marked up too and said it's ok and normal for this to happen. It was like wow!!! Recognise and thank the committee members who served and played an active role in completing this process. The Fulbright Program, the local chapter too who provided support and recreation. Those who sponsored my advisors and Angella Harvey of the US Embassy, Jamaica.

Overall the student experience at Georgia Tech was rich, rewarding, met all my expectations and more, and provided me with some kind of balance. I'm leaving with so much left on my "to do list!". ECE staff Marilou, Jackie, Luis of the workshop, third floor guys, Harry, facilities lady, Bob etc. thanks. Computer support and library staff whom I bothered a lot, Lori, Lauri. Loren of the student center, Tech caterers Kimberley Coates, Tech Police, etc., advice from Dr. Jin-Yeon Kim, those before me like David Stobbe who worked in the field. Standing on the shoulders of giants indeed!

My fellow lab partners, those who left before me and whom I'm leaving behind, for all the help in Matlab, etc. Thanks to Professor Michael Leamy and Professor Tom Gaylord for encouragement. Tech for lessons learnt in community service, sustainability, counseling center, fitness as a journey lifestyle. Success programs, Graduate Thesis Office, Sheila and the OIE, Prof. Kim for computer architecture help in prelims, also Prof. Elliot Moore for 3075, Matlab and FEM support from Rob Mathews. IEEE, HKN, Illumination, Society of Step, Students Organizing for Sustainability, Caribsa and Extensions. The GIFTED choir and Pastor Al are so nice. I look forward to go out and serve as I believe that to whom much is given much is also expected. So much to give thanks for!

Friends Ryan, Milap and entire group, Latoya, Keisha, Luc, George, Kevin, Andrea, Mahama, Onyi, Denise, Dhanaraj, Grant, Lindberg, Imona, Pasha, Nate, Pamela, Arun, Taneisha, Fulbright friends Marco, Andrea, etc., families that opened their homes to me, gave me their house and car, Stephen's family, Brother/Bishop M. Dwyer, Karla's family, Keisha. The landlord and house mates at 1100 Holly. Back home those checking up on me constantly, Shanti, Cornelius, Karen, Kadi and Family, Ann, Pat, Stacy, Jenine, Pooh, Instrument of Praise team for encouragement, Rodney, Ralph, David, Ellis and the BENG 2000 crew. Nadine and the long time plan for us both to be Drs. I'm waiting!

University of Technology, Jamaica (UTech) for the time off, UTech Engineering colleagues, lecturers who took my classes, Supervisor Thorpe, Technicians, Isiah, Heather and UTech HR for their patience. Long time friends like David (Dynamix), Stephen, Darren, Neil, Dayne, Mark, Christine and family whom I know always have my back, even lost friend Gregory, too.

Of course undying support from my family Karen and Davin, Mom (just in time for Mother's Day), Sis Dr. Roxanne R. Johnson (we did it!). You were all patient and assisted big time especially in that semester where I had to juggle work and writing up this thesis. Other sister Maxine Muir, VP in a world top 20 bank (Yes I'm spelling it out!) for long time support, you know waiting for the car to pass the house, other brothers and sisters in extended family on both step (Laverne and co.) and real dad (Raval and co.) sides too, Aunt Doreen and family, my vibrant cousin Jascinth, Aunt Joyce and family, Oneil etc., Halls and Fergusons. My real father who I learned was also looking out for me all this time, just didn't communicate so. Far back to Mr. Ivy, Smokey Joe (you know yourself!) at Cornwall College, Horace Lawrence, 10-5 crew. All Mobay high and Alvernia connections. Foundation gathered at UTech/CAST, the Instrument people (yes Powell!), 22 Gordon Town Road and so many of my own past students!

Newcastle University Prof. Finch, miss you cool girls, Jothi, Kat, Nav. Cable and Wireless telephone guys, and Mrs. Higgins for the UTech scholarship that started it all.

TABLE OF CONTENTS

Page

ACKNOWLEDGEMENTS i

LIST OF TABLES viii

LIST OF FIGURES xi

LIST OF ABBREVIATIONS xv

SUMMARY xvi

CHAPTER

1 INTRODUCTION 1

1.1 Problem Description 1

1.2 Overview of Approach 2

1.3 Principal Contributions 3

1.4 Organization of the Thesis 5

2 BACKGROUND 6

2.1 Overview of Nonlinear Ultrasonics 6

2.2 Third-Order Elastic Constants (TOECs) 9

2.3 Acoustoelasticity 11

2.4 Applications of Acoustolasticity 13

2.4.1 Traditional Acoustoelasticity Methods for TOEC Recovery 14

2.4.2 Stress Measurement 16

2.5 Non-Standard Ultrasonic Configurations for Acoustoelastcity Measurements 17

2.5.1 Bulk Wave Methods 18

2.5.2 Guided Wave Methods 20

2.6 Other Techniques in Acoustoelasticity and TOEC Recovery 21

2.7 Section Summary 23
3 THEORY DEVELOPMENT AND FORWARD PROBLEM 25
3.1 Ultrasonic Waves in Stressed Solids 26
3.2 Formulation of the Angle-Beam Acoustoelasticity Problem 31
3.2.1 Longitudinal Wave Acoustoelastic Constants 34
3.2.2 Shear Vertical Wave Acoustoelastic Constants 37
3.2.3 Shear Horizontal Wave Acoustoelastic Constants 38
3.2.4 Summary of Angle Beam Acoustoelastic Constants 39
3.3 Reconcilation with Prior Acoustoelastic Constants 41
3.3.1 Parallel and Perpendicular Propagation using Stress Derivatives 42
3.3.2 Oblique Propagation Constants in Literature 44
3.4 Forward Problem: Computation of Measured Time Shifts 47
3.4.1 Time Shift for Attached Transducer Configuration 47
3.4.2 Time Shift for Floating Transducer Configuration 48
3.5 Section Summary 50
4 INVERSE PROBLEM DEVELOPMENT 51
4.1 Required Measurements 51
4.2 TOEC Recovery Inverse Problem 52
4.2.1 Linearization of the Change in Time of Flight 53
4.2.2 Attached Transducers 54
4.2.3 Floating Transducers 57
4.2.4 Normal Incidence Case 57
4.3 Example Forward and Inverse Calculations 59
4.4 Sensitivity Analysis 62

4.5 Best Configuration for TOEC Recovery 64
4.5.1 Estimated Uncertainties of Input Variables.....64
4.5.2 Example Uncertainty Calculations 65
4.5.3 Common Refracted Angle Search.....66
4.5.4 Exhaustive Refracted Angle Search 72
4.5.5 Effect of Thickness.....81
4.5.6 Effect of V Paths 82
4.8 Section Summary.....83
5 EXPERIMENTS.....85
5.1 Overview.....85
5.2 Samples.....86
5.3 Loading Fixture.....87
5.4 Ultrasonic Instrumentation.....89
5.5 Waveform Acquisition Instrumentation 89
5.6 Measurement of Time Shifts.....90
5.7 Transducers and Angle-Beam Wedges.....91
5.7.1 Attached Configurations (Variable Separation Distance).....92
5.7.2 Floating Configurations (Fixed Separation Distance) 93
5.8 Fixed Transducer Configuration Measurement Procedure.....95
5.9 Floating Transducer Configuration Measurement Procedure.....98
5.10 Other Measurement Issues.....103
6 RESULTS: TOEC RECOVERY FOR ATTACHED TRANSDUCERS.....107
6.1 2L+1SV Forward Problem Results.....107
6.2 TOECs recovered using the 2L+1SV Solution.....110
6.3 Section Summary.....111

7 RESULTS: TOEC RECOVERY FOR FLOATING TRANSDUCERS 112
7.1 2L+1SV Forward Problem Results 112
7.1.1 Incremental Loading Method 114
7.1.2 Endpoint Loading Method 119
7.2 1L+1SV+1SH Forward Problem Results using Endpoint Loading Method 121
7.3 2L+1SH Forward Problem Results using Endpoint Loading Method 123
7.4 TOECs recovered from the 2L+1SV Configuration 123
7.4.1 Incremental Loading Method 124
7.4.2 Endpoint Loading Method 125
7.5 TOECs recovered from the 1L+1SV+1SH Configuration 126
7.6 TOECs recovered from the 2L+1SH Configuration 126
7.7 Section Summary 127
8 DISCUSSION 128
8.1 Review of Development Procedure 128
8.2 Evaluation of Numerical Exercises 131
8.3 Review of TOECs Recovered 132
9 CONCLUSIONS AND FUTURE WORK 136
9.1 Conclusions 136
9.2 Recommendations for Future Work 137
REFERENCES 140

LIST OF TABLES

Page

Table 2.1: Relationships among commonly used TOECs for isotropic solids 11

Table 3.1: Summary of acoustoelastic constants in natural and initial systems 40

Table 4.1: Possible wave mode combinations for TOEC recovery. 52

Table 4.2: Coefficients for expressing the time shift due to acoustoelasticity as a linear combination of TOECs $\left(\Delta TOF_A = a_0 + a_1 l + a_2 m + a_3 n\right)$. 56

Table 4.3: Input parameters for TOEC recovery examples 59

Table 4.4: Calculated time shifts for numerical examples.....60

Table 4.5: Recovered TOECs for the 2L+1SV configuration with L1=45º, L2=60 º and SV=45 º 60

Table 4.6: Recovered TOECs for the 2L+1SH configuration with L1=45º, L2=60 º and SH=70 º 61

Table 4.7: Recovered TOECs for the 1L+1SV+1SH configuration with L=60º, SV=45 º and SH=70 º.....61

Table 4.8: Recovered TOECs for the 1L+2SH configuration with L=60º, SH1=45 º and SH2=70 º 61

Table 4.9: Estimated uncertainties for all input parameters 64

Table 4.10: Uncertainties for the 2L+1SV configuration with attached transducers. 66

Table 4.11: Uncertainties for the 2L+1SV configuration with floating transducers 67

Table 4.12: Uncertainties for the 1L+1SV+1SH configuration with attached transducers 68

Table 4.13: Uncertainties for the 1L+1SV+1SH configuration with floating transducers 69

Table 4.14: Exhaustive search results for the 2L+1SV attached and floating configurations corresponding to minimum uncertainties in *l*, *m* and *n*.....74
Table 4.15: Exhaustive search results for the 2L+1SH attached and floating configurations corresponding to minimum uncertainties in *l*, *m* and *n*.....74
Table 4.16: Exhaustive search results for the 1L+1SV+1SH attached and floating configurations corresponding to minimum uncertainties in *l*, *m* and *n*.....75
Table 4.17: Exhaustive search results for the 1L+2SH attached and floating configurations corresponding to minimum uncertainties in *l*, *m* and *n*.....75
Table 5.1: Typical 5072PR pulser receiver settings 89
Table 5.2: Attached tests Perspex wedge angles 92
Table 5.3: Wedge angles and expected times-of-flight for floating configuration wedge pairs 98
Table 5.4: Summary of angle-beam measurement configurations for aluminum and low carbon steel (LCS) 6.32mm thick with Perspex wedges.....98
Table 5.5: Expected times-of-flight for the 7075 aluminum measurements for all wedge pairs.....98
Table 5.6: Summary of 2L+1SV angle beam measurement configurations using the incremental load method with multiple V paths. 102
Table 5.7: Summary of 2L+1SV, 2L+1SH and 1L+1SV+1SH angle beam measurement configurations using the end-point method with single V paths.....103
Table 6.1: Parameters for calculating time shift vs. load curves. 108
Table 6.2: Time shift analysis at max load of 194.26MPa for 7075 aluminum and LCS. 110
Table 6.3: Comparison of recovered TOECs for 7075 aluminum and low carbon steel to published values. 110

Table 7.1: Specimens used for floating transducer experiments 112
Table 7.2: Parameters for calculating time shift vs. load curves 114
Table 7.3: 2L+1SV time shift data obtained with the endpoint loading method.....120
Table 7.4: 1L+1SV+1SH time shift data obtained with the endpoint loading method.....122
Table 7.5: 2L+1SH time shift data obtained with the endpoint loading.....123
Table 7.6: 2L+1SV experimental TOECs recovered using the incremental loading method.....124
Table 7.7: 2L+1SV experimental TOECs recovered using the endpoint loading method.....125
Table 7.8: 1L+1SV+1SH experimental TOECs recovered using the endpoint loading method.....126
Table 7.9: 2L+1SH experimental TOECs recovered using the endpoint loading method.....127
Table 8.1: Summary of recovered TOECs for 7075-T6 aluminum.....131
Table 8.2: Summary of experimentally determined TOECs and literature values.....133
Table 8.3: General criteria test of AL7075 TOECs recovered. 134

LIST OF FIGURES

Page

Figure 1.1: Determining third order elastic constants from load-dependent time shifts....3

Figure 3.1: Sample of thickness h with a single V angle-beam path of refracted angle θ....31

Figure 3.2: Variation of acoustoelastic constants with refracted angle in (a) initial and (b) natural systems....41

Figure 3.3: Comparison of current L wave acoustoelastic constants with those of Dubuget et al. (a) Direct Comparison (b) Comparison after switching. K_1 and K_2 in Dubuget's formulae....46

Figure 3.4: Comparison of current SV and SH wave acoustoelastic constants with the S wave constants of Dubuget et al. (a) Direct Comparison (b) Comparison after switching K_1 and K_2 in Dubuget's formulae....46

Figure 4.1: Uncertainties in recovered TOECs caused by uncertainties in all input variables for the attached 2L+1SV configuration with a single V path....65

Figure 4.2: Uncertainty breakdown for the best 2L+1SV attached transducer pair of Table 4.10 (case 9)....70

Figure 4.3: Uncertainty breakdown for the best 2L+1SV floating transducer pair of Table 4.11 (case 9)....70

Figure 4.4: Uncertainty breakdown for the best 1L+1SV+1SH attached transducer pair of Table 4.12 (case 15)....71

Figure 4.5: Uncertainty breakdown for the best 1L+1SV+1SH floating transducer pair of Table 4.13 (case 15)....71

Figure 4.6: Uncertainty U_l / l vs. SV, L1 and L2 refracted angles 76

Figure 4.7: Uncertainty U_m / m vs. SV, L1 and L2 refracted angles 76

Figure 4.8: Uncertainty U_n / n vs. SV, L1 and L2 refracted angles 77

Figure 4.9: U_l / l as a function of L1 and L2 angles at the best SV angle 78

Figure 4.10: U_m / m as a function of L1 and L2 angles at the best SV angle 78

Figure 4.11: U_n / n as a function of L1 and L2 angles at the best SV angle 78

Figure 4.12: U_n / n as a function of L1 and SV angles at the best L2 angle 79

Figure 4.13: U_l / l vs. SV, L1 and SH angles at angles of minimum uncertainty 79

Figure 4.14: U_m / m vs. SV, L1 and SH angles at angles of minimum uncertainty 80

Figure 4.15: U_n / n vs. SV, L1 and SH angles at angles of minimum uncertainty 80

Figure 4.16: U_n / n vs. SH, L1 and L2 at angles giving minimum uncertainty 81

Figure 4.17: U_n / n vs L1 and SH at the best L2 angle 81

Figure 4.18: Thickness variation effect on TOEC recovery uncertainty 82

Figure 4.19: V path variation effect on TOEC recovery uncertainty 83

Figure 5.1: Block diagram of measurement setup 86

Figure 5.2: All coupons with average dimensions 76.32mm width by 6.32mm thick ...86

Figure 5.3: Hydraulic loading fixture 87

Figure 5.4: Propagation paths corresponding to 2V-SV, 3V-L and 4V-L.....92

Figure 5.5: Wedge pairs used for attached tests 93

Figure 5.6: Perspex wedge pairs used for the L and SV floating angle beam measurements.....94

Figure 5.7: Aluminum wedge block used for SH angle beam measurements 94

Figure 5.8: (a) Attached configuration angle-beam measurement setup. (b) Drawing of one possible attached transducer assembly 97

Figure 5.9: Floating configuration angle-beam measurement setup showing the transducers and aluminum sample 99
Figure 5.10: Floating pair assembly with variable angle adjustments (left) and floating pair assembly with wedges clamped together to maintain separation distance (right) 100
Figure 5.11: Typical set of time shift data results for 45L wave signals 101
Figure 5.12: Precision linear slide, microscope, calipers and micrometer used for wedge distance separation and specimen thickness measurements 104
Figure 6.1: Typical SV waveforms at zero and maximum load (double V configuration) used for time delay measurement 107
Figure 6.2: Shear vertical double V (2V-SV) time shift vs. load curves for (a) low carbon steel and (b) 7075 aluminum 108
Figure 6.3: Longitudinal triple V (3V-L) time shift vs. load curves for (a) low carbon steel and (b) 7075 aluminum 109
Figure 6.4: Longitudinal 4V (4V-L) time shift vs. load curves for (a) low carbon steel and (b) 7075 aluminum 109
Figure 7.1: Typical waveforms showing echoes of interest for (a) L, (b) SV and (c) SH wave modes 113
Figure 7.2: Floating 2L+1SV time shift vs. load curves for 7075-T6 aluminum with multiple V Paths 115
Figure 7.3: Floating 2L+1SV time shift vs. load curves for 7075-T6 aluminum with single V Paths 115
Figure 7.4: Floating 2L+1SV time shift vs. load curves for 7075-T651 aluminum with multiple V Paths 116

Figure 7.5: Floating 2L+1SV time shift vs. load curves for 7075-T651 aluminum with single V Paths 116
Figure 7.6: Floating 2L+1SV time shift vs. load curves for 2024 aluminum with multiple V Paths....117
Figure 7.7: Floating 2L+1SV time shift vs. load curves for 2024 aluminum with single V Paths 117
Figure 7.8: Floating 2L+1SV time shift vs. load curves for low carbon steel with multiple V Paths....118
Figure 7.9: Floating 2L+1SV time shift vs. load curves for low carbon steel with single V Paths 118
Figure 7.10: Data from the 45L floating wedge pair on aluminum 7075-T6 sample for five repetitions 119
Figure 8.1: Recovered TOECs, floating 2L+1SV compared to literature values 133
Figure 8.2: Time shift floating 2L+1SV data compared to those calculated from literature values of TOECs at maximum load....134

LIST OF ABBREVIATIONS

TOEC	Third Order Elastic Constants
SOEC	Second Order Elastic Constants
SHM	Structural Health Monitoring
NDE/T	Nondestructive Evaluation/Testing
NLU	Nonlinear Ultrasonics
CAN	Contact Acoustic Nonlinearity
L	Longitudinal Wave
SV	Shear Vertical Wave
SH	Shear Horizontal Wave
TOF	Time-of-Flight
ΔTOF	Time Shift
PZT	Lead Zirconate Titanate
EMAT	Electromagnetic Acoustic Transducer
2L+1SV	Two Longitudinal and one Shear Vertical Wave Modes
2L+1SH	Two Longitudinal and one Shear Horizontal Wave Modes

SUMMARY

This thesis describes procedures and theory for a family of one-sided ultrasonic methods for determining third order elastic constants (TOEC) using sets of angle-beam wedges mounted on one side of a specimen. The methods are based on the well-known acoustoelastic effect, which is the change of wave speed with applied loads and is a consequence of the mechanical nonlinearity of a material. Increases in material nonlinearity have been correlated to the progression of damage, indicating that tracking changes in TOECs may provide a practical means of monitoring damage accumulation at the microstructural level prior to formation of macroscopic defects.

Ultrasonic methods are one of the only ways to measure TOECs, and most prior techniques have utilized wave propagation paths parallel and perpendicular to the loading directions. A few additional ultrasonic techniques reported in the literature have employed oblique paths but with immersion coupling. These reported techniques are generally unsuitable for field implementation. The one-sided contact approach described here is applicable for in situ measurements of TOECs and thus lays the foundation for tracking of TOECs with damage.

Theory is reviewed and further developed for calculating predicted velocity changes, and thus time shifts, as a function of uniaxial tensile loading for longitudinal, shear vertical, and shear horizontal waves in the context of angle-beam transducers mounted on the surface of the specimen. A comparison is made to published results where possible. The inverse problem of determining the three TOECs of an isotropic material from three measurements employing three different angle beam configurations is

comprehensively analyzed. Four configurations providing well-posed solutions are identified and examined. A detailed sensitivity analysis is carried out to identify the best mounting configuration, wave mode combinations, refracted angles and geometry requirements for recovering the three TOECs.

Two transducer mounting configurations are considered: (1) attached (glued-on) transducers potentially suitable for in situ monitoring, and (2) floating (oil-coupled) transducers potentially suitable for single measurements. Limited experimental results are presented for the attached case using two longitudinal measurements and one shear vertical measurement. The floating case experiments utilized three of the four well-posed solutions, and measurements were made on several aluminum alloys and low carbon steel. Key experimental issues are identified and discussed for both transducer mounting configurations.

The specific contributions of this thesis are:

1. Development of the general theory for determining TOECs of isotropic materials with a one-sided approach using contact angle-beam transducers. This development includes identification of four valid measurement configurations that result in a well-posed problem for recovering the three TOECs.
2. Development of the specific theory as applied to attached (i.e., glued-on) angle-beam transducers that have a variable separation distance with load. This coupling method is potentially suitable for in situ monitoring applications.
3. Development of the specific theory as applied to floating (i.e., liquid-coupled) angle-beam transducers where the separation distance does not change with load. This method is potentially suitable for single field or laboratory measurements.

4. Comparison of the eight valid TOEC recovery methods (four wave mode configurations, each having two mounting techniques) via numerical simulations and a detailed sensitivity analysis in which the effect of all expected measurement and parameter errors on determination of the TOECs is quantified.
5. Development of experimental methods that provide insight as to the relative merits of the attached vs. floating coupling methods.

CHAPTER 1

INTRODUCTION

1.1 Problem Description

The objective of this research is to develop theory and experimental methods for measuring third order elastic constants (TOECs) using one-sided angle-beam ultrasonic techniques for a homogeneous, isotropic parallel faced material. The ultrasonic method is based upon the acoustoelastic effect, which is the change of ultrasonic velocity with stress. Acoustoelastic constants are functions of TOECS, which characterize the mechanical nonlinearity of a material. Since an increase in material nonlinearity has been correlated to progression of damage [1], tracking changes in TOECs may provide a practical means of monitoring damage accumulation at the microstructural level prior to formation of macroscopic defects. Developing damage monitoring capabilities requires a reliable method which can accurately and repeatedly track parameters related to damage.

The most widely used method for determination of TOECs of solids is ultrasonic wave speed measurements [2, 3]. Prior ultrasonic measurements of TOECs have utilized wave propagation paths parallel and perpendicular to the loading direction, which simplifies theory but can be a prohibitive requirement for field implementation. There are several possible advantages of an angle-beam technique. First, it can readily be implemented as a one-sided contact technique, not requiring transducers to be mounted on both sides of a specimen or immersion of the specimen and transducers. Second, it is not necessary to embed transducers inside of specimen grips to generate beam paths directly along the loading direction as can be the case for traditional methods. Even though the well-known general theory of acoustoelasticity applies to this situation, the

specific theory for determining TOECs from angle beam measurements of acoustoelastic constants using a one-sided contact approach is not found in the literature.

1.2 Overview of Approach

This research involves measuring multiple acoustoelastic constants for different refracted angles and wave modes for specimens undergoing uniaxial tensile loading, and then determining the TOECs of the material from the measured acoustoelastic constants. Interests in two transducer configurations are considered: (1) attached (glued-on) transducers suitable for in situ monitoring, and (2) floating (oil-coupled) transducers suitable for single measurements. Changes in times-of-flight are measured as a function of applied loads and TOECs are then recovered. A detailed sensitivity analysis is carried out to select the best transducer mounting configuration, wave mode combinations, refracted angles and geometry, and compare previously implemented methods to the angle-beam method. As is the case for traditional methods, the acoustoelastic effect is very small and requires very careful measurements. Results are verified by comparing the measured TOECs to published values for several aluminum alloys and low carbon steel.

Figure 1.1 illustrates the process of recovering the TOECs. First, time shifts due to changes of the specimen geometry during loading are computed. These are functions of the overall geometry, second order elastic constants, applied load and density. Next, the actual time shifts are measured. The difference between the measured time shifts and those due to geometry are the time shifts due to acoustoelasticity, which are a function of the TOECs. A set of these time shifts are inverted to obtain the TOECs *l, m* and *n*.

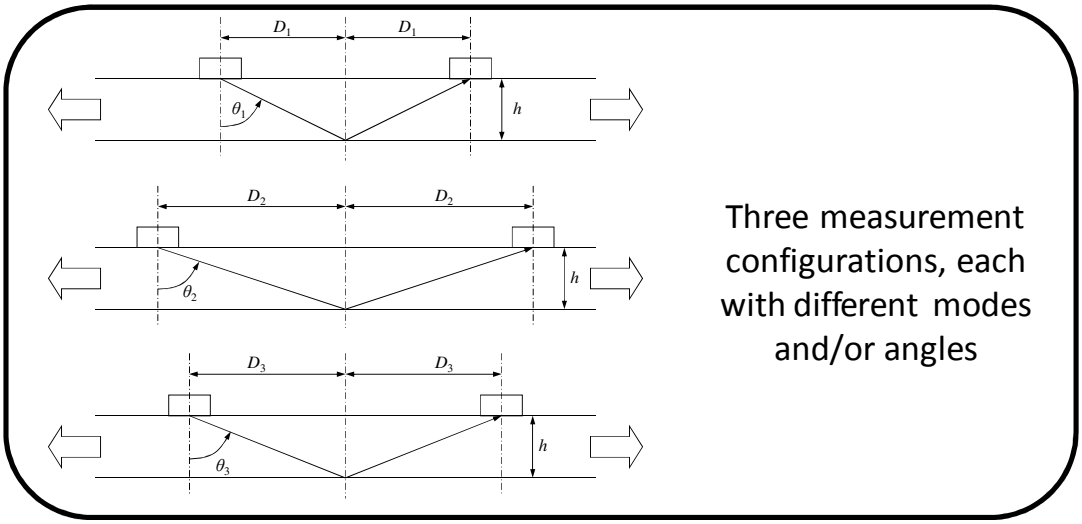

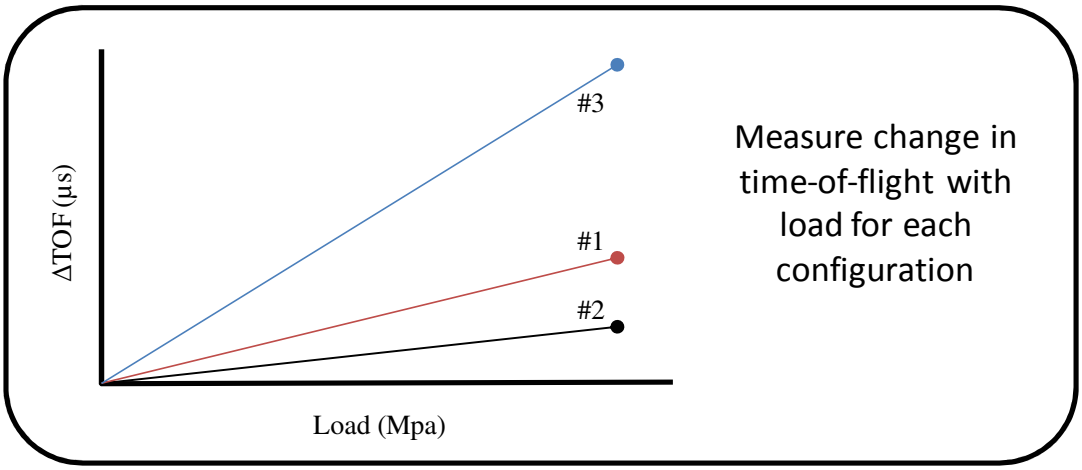

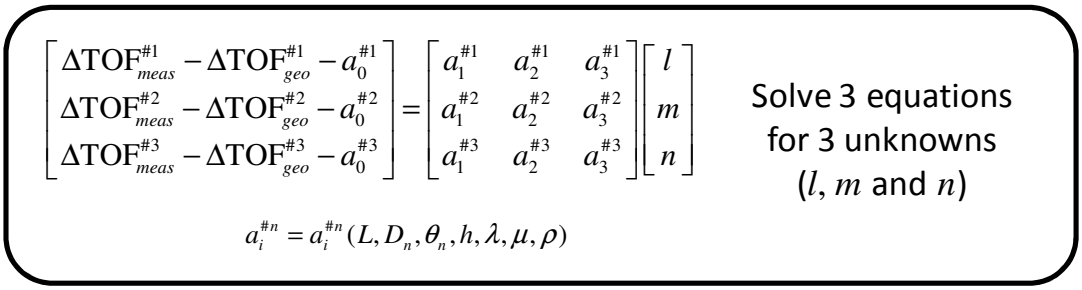

Figure 1.1. Determining third order elastic constants from load-dependent time shifts.

1.3 Principal Contributions

Previous work in nondestructive evaluation (NDE) has led to the replacement of earlier concepts of "zero defects" in materials with the regarding of all materials as being

somewhat flawed from the manufacturing stage [4]. This change in thinking has paved the way for new advances in examining early microstructure changes long before the initiation of macrocracks. This research is motivated by studies which have shown that nonlinearity parameters (e.g., β) exhibit a much larger change over the fatigue life of a specimen compared to linear parameters such as attenuation. Since a material nonlinearity parameter β and the material's TOECs are directly linked, TOECs are good potential candidates for tracking damage. Early researchers such as Sathish [1] have also commented on the limited quantity of techniques which focus on stages of life before crack initiation and formation. This research will provide the enabling technology for one-sided, in situ measurements of TOECs suitable for both SHM and NDE applications.

The specific contributions of this thesis are:

1. Development of the general theory for determining TOECs of isotropic materials with a one-sided approach using contact angle beam transducers. This development includes identification of four valid measurement configurations that result in a well-posed problem for recovering the three TOECs.
2. Development of the specific theory as applied to attached (i.e., glued-on) angle beam transducers that have a variable separation distance with load. This coupling method is potentially suitable for in situ monitoring applications.
3. Development of the specific theory as applied to floating (i.e., liquid-coupled) angle beam transducers where the separation distance does not change with load. This method is potentially suitable for single field or laboratory measurements.
4. Comparison of the eight valid TOEC recovery methods (four wave mode configurations, each having two mounting techniques) via numerical simulations and

a detailed sensitivity analysis in which the effect of all expected measurement and parameter errors on determination of the TOECs is quantified.

5. Development of experimental methods that provide insight as to the relative merits of the attached vs. floating coupling methods.

1.4 Organization of the Thesis

This research effort is concerned with extending existing acoustoelastic theory and experimental methods by focusing on the one-sided recovery of TOECs of engineering alloys. A literature review of nonlinear ultrasonics, third order elastic constants, and acoustoelasticity is provided in Chapter 2. In Chapter 3, theory is presented and extended for the forward problem of determining expected time shifts as a function of load for one-sided angle-beam measurements. Chapter 4 considers the inverse problem of recovering the TOECs from the measured time shift data. Of particular interest is a sensitivity analysis illustrating how errors in various parameters affect the accuracy of the TOEC recovery process. Chapter 5 describes experimental measurements, which are reported in Chapter 6 for the attached transducer configuration and Chapter 7 for the floating transducer configuration. Results are discussed in Chapter 8 and concluding remarks made in Chapter 9.

CHAPTER 2

BACKGROUND

The focus of the research presented in this thesis is the development of an angle-beam acoustoelastic method for determining third-order elastic constants (TOECs). The goal of the background review is to put this research effort in the context of prior work in the areas of nonlinear ultrasonics (NLU), TOECs, and acoustoelasticity. Linear ultrasonics falls under the larger umbrella of NLU. Linear ultrasonics is a well-established field where wave speed and attenuation are parameters typically considered in the field of nondestructive evaluation (NDE). Most linear theories in acoustics have been established by making various assumptions to linearize the more general nonlinear problems. Additional background information on ultrasonics can be found in [3, 5, 6].

2.1 Overview of Nonlinear Ultrasonics

Nonlinear ultrasonics refers to nonlinear phenomena associated with waves and vibrations at ultrasonic frequencies above 20 kHz. Nonlinear phenomena of frequent interest include finite amplitude effects, harmonic generation, and acoustoelasticity. NLU mainly involves the study these phenomena singly and in combination [7].

The finite amplitude approach leads to measurements of specific harmonics from a large amplitude monotone input or the search for shifts in frequency when sweeping the input frequency. The nonlinear elastic wave spectroscopy (NEWS) method is one example based on nonlinearity in the constitutive relation resulting in shifts in resonant frequencies and nonlinear attenuation [8].

The harmonic generation approach has also been widely studied. In this approach material nonlinearity is investigated by measuring higher-order harmonics resulting from large amplitude sinusoidal excitations, and efforts have been made to correlate these harmonics to damage [9, 10]. Suzuki and Hikata looked at harmonics resulting from the glide motion of dislocations in materials [11]. Their results agreed with the earlier experiments of Hikata and Chick [12] and can be regarded as among the pioneering work in this area of nonlinear ultrasonics. Typically, the amplitude of the second harmonic compared to the first is about 40-100 times smaller in metals. The magnitude of these harmonics, particularly the second-order harmonic, gives a measure of the acoustic nonlinearity parameter (β), which is an absolute nondimensional parameter that characterizes the acoustic nonlinearity of the medium.

The acoustoelasticity approach looks at wave propagation in stressed media, and a theoretical review of the effect is based upon the nonlinear theory of elasticity. Biot in 1940 was the first to report that the propagation of elastic waves in solids in the presence of stress is different from the stress-free case [13].

Material nonlinearity is the result of nonlinear interactions at the atomic scale. If an acoustic signal is used to interrogate such a material, the resulting nonlinear acoustic phenomena can include nonlinear losses, generation of higher harmonics, and shifts in resonant frequencies. Generally, material nonlinearity consists of two sources, the inherent or natural nonlinearity and the damage-induced nonlinearity. The natural nonlinearity evolves from two main origins, geometric nonlinearity and intrinsic physical nonlinearity. Damage-induced nonlinearity includes contact acoustic nonlinearity (CAN), which is a spatially concentrated source and occurs in solids containing cracks

that may open and close when subjected to ultrasound [14]. Both natural and damage induced nonlinearities contribute to the general nonlinear stress-strain behavior of a material [15].

There can be distributed sources of nonlinearity resulting from fatigue damage, since nonlinearity results from regions of microplasticity because of elastic plastic deformation in the material. These may be a result of residual stress since the microstructures with significant residual stress will have different elastic properties than the stress-free microstructure. Ageing also causes microstructural changes over the life of parts, which can change the acoustic velocity of waves used to interrogate materials. As the microstructure changes continuously under mechanical loading, the early signs of damage include the formation of dislocation dipoles, vein structures, and persistent slip bands, which are precursors to crack formation [16]. Overall, the study of damage evolution is complicated, involving computational mechanics and multiscale modeling to understand the core phenomena. Good resource texts that cover nonlinear wave theory, material nonlinearity, and constitutive models are [15, 17].

Sathish et al. [1] considered early detection of fatigue damage in titanium alloys. They reported some of the challenges in detecting cracks smaller than 50 μm and commented on the low quantity of techniques that focus on detecting early changes in microstructures before crack initiation and formation. A comparison of linear and nonlinear ultrasonic techniques found much larger increases in the nonlinear parameters compared to linear ones over the fatigue life of specimens. Van Den Abeele et al. [8] and Nagy [18] also made the distinction between linear and nonlinear methods and have reported similar results. Van Den Abeele et al. clearly distinguished nonlinear behaviors

in both the elastic and plastic regions before failure, with both regimes showing similar trends. Yang et al. [19] considered age hardening effects from heat treatment of nickel maraging steel, and showed changes in TOECs after treatment.

The results above provide some evidence of the importance of NLU techniques. Kim et al. [10] in 2006 recommended the next step in the use of NLU techniques to be a systematic study that quantifies the accuracy and validity of detection in early stages prior to crack initiation. They mention the need for developing experimental procedures that are field implementable and repeatable.

2.2 Third Order Elastic Constants

TOECs, which are a measure of material nonlinearity, have a relation to the anharmonic properties of materials and provide information on interatomic bonding forces. TOECs have been linked to the ultimate strength of a material [20] and are used in determining residual and applied stress, e.g., [21]. TOECs are also related to thermal expansion, crystal structure, ultrasonic absorption, wave speed and deformation, temperature, and pressure dependence of elastic properties and are used in describing the interaction of acoustic and thermal phonons [22].

TOECs were introduced to account for effects that could not be explained with a linear stress-strain model. Crecraft [23] presented insight into these unexplained effects by explaining the stress-strain relationship on an atomic scale, considering inter-atomic force variations with spacing. If the assumption is made that the material is hyperelastic, then a strain energy function can be expressed as a power series in strain. The constitutive law, where U is the strain energy function, is shown in Equation (2.1) for small strains with the assumption that the material is hyperelastic (i.e., elastic materials whose stress-

strain relationship is derived from a strain energy function). Following the development in [15, 24],

$$U = C^{(0)} + C_{ij}^{(1)}\,\varepsilon_{ij} + \frac{1}{2!}C_{ijkl}^{(2)}\,\varepsilon_{ij}\,\varepsilon_{kl} + \frac{1}{3!}C_{ijklmn}^{(3)}\,\varepsilon_{ij}\,\varepsilon_{kl}\,\varepsilon_{mn} + \cdots, \quad (i, j = 1,2,3)\,, \tag{2.1}$$

In this equation, ε_{ij} is the Lagrangian strain tensor, which is approximated by $\varepsilon_{ij} \approx \frac{1}{2}\left(\frac{\partial u_j}{\partial a_i} + \frac{\partial u_i}{\partial a_j}\right)$ for small deformations [25]. If the strain energy is zero before deformation and the biasing stress is zero for zero strain, then the first and second term of Eq. (2.1) are zero. C_{ijkl} and C_{ijklmn} are the second-order elastic constants (SOEC) and TOECs, respectively, with coordinates a_i and displacements u_i. The Second Piola-Kirchoff stress tensor [26], σ_{ij}, is defined as $\sigma_{ij} = \frac{\partial U}{\partial \varepsilon_{ij}}$. Therefore,

$$\frac{\partial U}{\partial \varepsilon_{ij}} = C_{ij}^{(1)} + C_{ijkl}^{(2)}\varepsilon_{kl} + \frac{1}{2}C_{ijklmn}^{(3)}\varepsilon_{kl}\varepsilon_{mn} + \cdots \tag{2.2}$$

$$\frac{\partial \sigma_{ij}}{\partial \varepsilon_{kl}} = C_{ijkl}^{(2)} + C_{ijklmn}^{(3)}\varepsilon_{mn} + \cdots \tag{2.3}$$

Equation (2.3) represents the nonlinear stress-strain relation with an effective elastic modulus. TOECs C_{ijklmn} are written here in the Brugger full indicial form [27], and represent a total of 729 TOECs. Due to symmetry the number reduces to 56 independent TOECs. For higher symmetries, the number of independent third-order coefficients necessary to define the properties of a particular material is reduced, and is three for an isotropic solid, the highest crystal symmetry achievable [15]. These constants can be represented in several forms, and their relationships are shown in Table 2.1 for an isotropic solid.

Table 2.1. Relationships among commonly used third order elastic constants for isotropic solids.

Brugger	Murnaghan Hughes & Kelly	Landau and Lifshitz	Toupin & Bernstein
C_{111}	$2l+4m$	$2A+6B+2C$	$\nu_1+6\nu_2+8\nu_3$
C_{112}	$2l$	$2B+2C$	$\nu_1+2\nu_2$
C_{123}	$2l-2m+n$	$2C$	ν_1
C_{144}	$m-(n/2)$	B	ν_2
C_{155}	m	$B+(A/2)$	$\nu_2+2\nu_3$
C_{456}	$n/4$	$A/4$	ν_3

The Voigt notation is used for convenience in Table 2.1, where 11~1, 22~2, 33~3, 23~4, 13~5, and 12~6. Three of the Brugger TOECs are independent for an isotropic material, namely, C_{123}, C_{144} and C_{456}. The other three are linear combinations of the first three, with $C_{112}=C_{123}+2C_{144}$, $C_{155}=C_{144}+2C_{456}$, $C_{111}=C_{123}+6C_{144}+8C_{456}$. An isotropic material has two independent SOECs, $C_{12}=\lambda$, $C_{44}=\mu$, and $C_{11}=\lambda+2\mu$, where λ and μ are the Lamé constants. In crystalline solids the absolute magnitude of the TOECs is generally one order higher than SOECs [28]. The TOECs are all negative and should satisfy the condition $C_{111} < C_{112} < C_{123}$ [29]. A Cauchy relationship for TOECs is mentioned by Hwa et al. [30], which states that $C_{456}=C_{144}=C_{123}$. These relationships can be used to assess the validity of TOECs recovered from measurements.

2.3 Acoustoelasticity

The theory of acoustoelasticity was first developed by Hughes and Kelly [31] in 1953 based on the Murnaghan theory of finite deformations [32]. Murnaghan's theory described the strain energy function as a third-order polynomial in strains, which then led to a second-order constitutive relationship. The term acoustoelasticity (elastoacousticity

or sonoacousticity or the stress acoustic constant) comes from analogies with photoelasticity. An acoustoelastic constant K can be found from a particular experiment as $K = \Delta c/(\sigma c)$, where c is the wave speed and σ is the applied stress. The constant K is dependent on the specific wave mode, polarization, direction of propagation, and stress orientation. Acoustoelasticity is based on the continuum theory of small disturbances (ultrasonic waves) superimposed on an elastically deformed body formulated by Cauchy during the classical era in 1829. The basic assumption is that the material remains in the elastic region throughout the deformation. Acoustoelasticity is a nonlinear effect, and its constant K is a function of both SOECs and TOECs.

Toupin and Berstein [24] in 1961 considered hyperelastic materials of arbitrary symmetry and defined three states for ultrasonic waves in stressed media: the stressless original state (free or natural state), a stressed and deformed (initial) state, and a state when the ultrasonic wave motion acts on the deformation or final state. They developed a set of TOECs, ν_1, ν_2, and ν_3 (also called the 3rd order Lamé constants), and completed the basic theory for determining TOECs for an isotropic medium popularly known as the "five constant theory," i.e., λ, μ, ν_1, ν_2, and ν_3. A thermodynamically correct theory describing the propagation of ultrasonic waves in pre-stressed solids was developed by Thurston and Brugger in 1964 [33]. They derived expressions for the velocity and the pressure/stress derivatives in terms of SOECs and TOECs for both applied hydrostatic stress and uniaxial stress distributions.

Accurate measurements of the acoustoelastic effect are difficult because of the small magnitude of the effect, since the relative change in wave speed is of the order of 0.001% per MPa of applied stress for metals. In typical acoustoelasticity measurements,

the time shift (proportional to velocity change) as a function of applied load for a plane wave to propagate over a certain path is measured. Because of the small velocity changes, attaining reproducible time-of-flight measurements is essential in accurately measuring the acoustoelastic effect. Detection of the acoustoelastic effect is closely related to several parallel efforts in accurately measuring small velocity changes. McSkimim et al. [34] used the superposition method for measuring velocities in acoustoelastcity measurements. Two different frequencies are combined and yielded velocity accuracy within one part in 5000. Other researchers at the time (e.g., Crecraft [35]) used the "sing around" technique and accounted for the fractional changes in velocity. This method relies on the transmitted pulse retriggering the transmitter until a repetition frequency is obtained. A recent attempt at making more accurate velocity measurements considers changes in refracted angles in a refractometry technique and offers some advantages over traditional time-of-flight measurements [36]. In [37], Janssen mentions that ultrasonic couplants are a weak link in these experiments. His work suggests a coupling layer thickness greater than 80 μm for reproducible time-of-flight determination in both shear (S) and longitudinal (L) wave propagation. Wave velocities are also influenced by temperature and material texture and can adversely affect the accuracy of the acoustoelasticity measurements. An analysis of the effect of temperature on acoustoelasticity measurements was given by Mi et al. [38].

2.4 Applications of Acoustoelasticity

The two most important applications of acoustoelasticity have been the determination of TOECs and the measurement of stress (both applied and residual). Direct measurement of various acoustoelastic constants has also been considered for

damage detection in several configurations, [39, 40], although little work has been done in this area.

2.4.1 Traditional Acoustoelasticity Methods for TOEC Recovery

Most traditional ultrasonic techniques for recovering TOECs from wave speed changes utilize propagation perpendicular and parallel to the applied loading direction. Crecraft in 1962 determined the Murnaghan TOECs for nickel steel from the computation of the small changes in velocity resulting from the applied stress. He found a linear relation between this applied stress and the velocity changes for all bulk wave types [35]. Bogardus in 1965 determined TOECs for fused silica, magnesium oxide, and germanium using Thurston's theory for pressure derivatives from velocity measurements [41]. Smith et al. in 1966 were among the first to carry out measurements to obtain the TOECs of several polycrystalline metals. Ultrasonic velocity measurements were made with wave propagation normal to the stress, and evaluation of constants was also done using Thurston's theory [42]. The use of longitudinal and shear waves to measure the TOECs of rail steel was carried out by Egle and Bray in 1976. The longitudinal wave in the direction of applied load shows the largest relative change of wave speed with strain. [43]. In 2005 Stobbe [44] used perpendicular longitudinal and shear (both polarization) paths of propagation to recover TOECs for aluminum 7075. He considered changes in TOECs over the fatigue life of a coupon.

Hughes and Kelly measured TOECs for polystyrene, pyrex, and Armco iron using the velocity equations they derived [31]. Their derivation for isotropic materials led to five equations for determining SOECs and TOECs, three for uniaxial tension and two for hydrostatic pressure. By using the theory of Murnaghan, Hughes and Kelly carried out

measurements at directions perpendicular and parallel to the loading direction. Three of these equations for wave velocities in the principal directions for uniaxial tension are shown here. Equation (2.4) is for a longitudinal (L) wave propagating parallel to the applied uniaxial stress:

$$\rho_o c_{1x}^2 = \lambda + 2\mu - \frac{\sigma}{3K_o}\left[2l + \lambda + \frac{\lambda+\mu}{\mu}\left(4m + 4\lambda + 10\mu\right)\right]. \tag{2.4}$$

Equation (2.5) is for an L wave propagating normal to the applied uniaxial stress:

$$\rho_o c_{1y}^2 = \lambda + 2\mu - \frac{\sigma}{3K_o}\left[2l - \frac{2\lambda}{\mu}\left(m + \lambda + 2\mu\right)\right]. \tag{2.5}$$

Equation (2.6) is for a shear vertical (SV) wave propagating parallel to the stress direction.

$$\rho_o c_{2x}^2 = \mu - \frac{\sigma}{3K_o}\left(m + \frac{\lambda n}{4\mu} + 4\lambda + 4\mu\right). \tag{2.6}$$

Here ρ_o is the density of the material in the unstrained state, σ denotes the tensile load applied, and λ and μ are the Lamé constants. $K_o = \lambda + \frac{2}{3}\mu$ is the bulk modulus for an isotropic material in the unstrained state, and *l, m,* and *n* are the Murnaghan TOECs.

Kato et al. considered compliance constants (the inverse of stiffness constants) through fourth order and showed their dependence on not only stress, but also macroscopic characteristics such as effective elastic-plastic constants of metals. Their work made use of quasi longitudinal and shear waves and extended into the plastic regime [45]. Pao et al. reexamined earlier assumptions contained in the theory of small motions superimposed on a large deformation and the theory of hyperelasticity [46].

They showed that the existing theory of acoustoelasticity was applicable to problems of TOEC determination but not to those of residual stresses.

Some specific experimental issues of these traditional approaches complicate the measurement process. First, transducers are usually mounted on both sides of a specimen, which makes alignment difficult and precludes in situ implementation. Second, specimens are typically very thin, resulting in very small time shifts. Third, it is necessary to embed transducers inside the specimen grips to generate beam paths along the loading direction when applying uniaxial loads in a testing machine.

2.4.2 Stress Measurement

The knowledge of both applied and residual stress is of interest to several communities. These include structural engineers, material fabrication and control, welding, and heat treatment communities. Some of the challenges faced by the stress reconstruction community are similar to those encountered in the TOEC recovery process due to their direct relationships.

Benson and Raelson [47] and Tokuoka and Iwashimizu [48] looked at birefringence (S waves of different polarizations propagate with velocities under load) of acoustic waves in experiments with deformed elastic media. They derived basic acoustoelasticity relations of the variation of velocity with stress. These relations showed that the acoustical birefringence is proportional to the difference of principal stresses. Bergman and Shahbender carried out experimental investigations on velocity changes of bulk waves in stressed aluminum samples [49]. Their work showed the dependence of wave speed on relevant elastic constants with relation to applied stress and density changes due to a change in volume from deformation. Bolt axial stress determination by

Johnson et al. [50] using time-of-flight measurements for L and S waves was carried out and had the advantage of not requiring length measurements. The method showed good results in a comparison with torque measurements for the space shuttle landing wheel fasteners [51]. Mi et al. used the time shift of shear vertical ultrasonic signals to deduce applied stress with knowledge of SOEC and TOECs using attached ultrasonic transducers in a crack monitoring application [38].

The similarities between photoelastic and acoustoelastic birefringence were studied by Crecraft, and initial attempts were made to solve problems of separating residual stresses and material texture [21, 23]. The importance of birefringence led to several applications to determine stress in solids. In the 1970s, acoustoelasticity investigations focused on methods to isolate texture effects from the desired effects of stress-induced anisotropy. Iwashimizu and Kubomura studied the effect of slight anisotropy on elastic wave propagation and found that the polarization direction of shear waves rotates for uniform applied stress [52]. Dorfi developed an ultrasonic stress reconstruction method based on acoustoelasticity theory for orthotropic media [53]. His method showed good temperature sensitivity and agreement with predictions from finite element analysis work. Crecraft [23] and Hsu [54] confirmed that the velocities are linear functions of applied stress with very small changes in velocity reported.

2.5 Non-Standard Ultrasonic Configurations for Acoustoelasticity Measurements

Some acoustoelasticity experiments done without using bulk wave propagation normal or parallel to the direction of applied stress are reported here. These methods include using bulk waves propagating at oblique angles and guided wave modes.

2.5.1 Bulk Wave Methods

The theory for the use of bulk waves in acoustoelasticity measurements in normal incidence cases was established over 40 years ago and the use of oblique incidence bulk waves about 20 years ago. Dubuget et al. used oblique incidence bulk waves and developed an immersion device for measuring acoustoelastic responses for various directions of propagation. They then used these responses to calculate TOECs for 7075 aluminum [55]. Their work confirmed that in the propagation plane perpendicular to the applied stress, the acoustoelastic effect is isotropic. In the propagation planes parallel to the applied stress direction, the acoustoelastic constants are angle dependent. Specifically, for L wave propagation, the acoustoelastic constant was positive at normal incidence and then became negative in sign as the refracted angle increased, i.e., as the propagation direction rotated toward the applied stress direction. Their method required knowing the thickness of the sample with great accuracy and no details were provided on the derivation of the acoustoelastic constants.

Bouhadjera in 2003 [56] developed a simple apparatus and presented formulae to recover TOECs using a pulse echo immersion technique. No derivations are shown. He comments on the difficulties in traditional measurements and shows that his device requires only one parameter, namely, the time-of-flight (TOF), to be determined accurately for multiple measurements to recover TOECs. His work is very appealing but is restricted to a laboratory environment since transducers were rotated around a prism-shaped specimen under uniaxial loads in an immersion setup to achieve multiple refracted angles. A contact transducer was also used to measure L waves in the specimen. His

results included plots of S and L wave velocity changes vs. loads, and no values of TOECs were reported.

Angle-beam acoustelasticity work has also involved separating the effects of residual stress and texture on wave speed. This problem has been addressed by Dorfi and others by developing methods such as his generalized acoustic ratio (GAR) technique to reduce the effect of texture on residual stress measurements by making additional measurements at various angles to eliminate unknown material parameters [57]. King and Fortunko reviewed procedures applied to stress evaluation and found that acoustic measurements with bulk waves propagating normal to the surface do not provide sufficient information to separate the influences of stress and material property variations such as texture [58]. They derived expressions for shear horizontal velocities in terms of the incident angle, acoustoelastic constants, and principal stresses and were able to separate texture and stress effects.

Other oblique angle methods include the work of Sinaie [59], who used quasi-shear wave immersion measurements at six different angles to solve for texture parameters that were then separated from stress-induced effects. Because his primary interest was residual stress measurement, Sinaie assumed a slight anisotropy in the wave propagation problem with a cubic structured sample under test and solved the problem of obtaining wave velocities in terms of texture parameters. Zhao's work with an oblique incidence technique proved that the time delay measurement is related to the phase velocity for propagation in any arbitrary plane of an arbitrary anisotropic medium [60]. He also conducted a sensitivity analysis on the effect of averaging methods for the determination of elastic moduli. His simulation showed that accurate thickness

measurements were not necessary to achieve satisfactory results. Overall, oblique incidence techniques have been used in several applications. One possible drawback noted by King et al. is that in plates, reflected SV and L waves are coupled and show phase shifts as a function of angle of incidence.

2.5.2 Guided Wave Methods

Guided wave methods reviewed here include Rayleigh or surface waves and Lamb waves. Intuitively, surface wave methods could be viewed as a limit in angle-beam work as the refracted angle approaches 90; with the other limit being normal incidence. However, because of the complex nature of these waves, specific theory has to be developed. In surface wave methods, the ultrasonic transmitter and receiver are on the same side of the specimen, and this setup naturally leads to one-sided test configurations. Rayleigh or surface waves have been used to measure mechanical properties in various materials in general and have the advantage of not requiring thickness measurements [61].

Several one-sided tests have been reported where the majority measure acoustoelastic constants using Rayleigh waves. An example is [40], where the approach is accompanied by the assumption that the material is homogeneous in depth. Other examples of one-sided surface wave tests are point contact measurements. Acoustoelasticity resulting from Rayleigh waves is shown by Berruti et al. and favorably compares to the results of an acoustic microscopy technique for measuring the acoustoelastic effect on a sample of AA 6082 T6 aluminium alloy [62]. Lee and Kuo in 2004 applied a point contact technique and took advantage of not only Rayleigh waves, but also the surface skimming longitudinal wave, and determined acoustoelastic constants

accordingly [63]. Their focus was the measurement of the effect and the change in the acoustoelastic constants with loading, and no mention was made of material property determination. Tanala et al. also used Rayleigh waves along with subsurface longitudinal waves because of the sensitivity of L waves to the acoustoelastic effect [64]. Their use of the acoustoelastic effect in Rayleigh waves for tracking fatigue damage in Wasaloy is a one-sided approach, and the results are promising. The acoustoelastic coefficients derived decreased with increased fatigue damage, and there was also a sign change.

The acoustoelastic effect for Lamb waves was explored by Husson, whose theoretical work predicts sensitivity only to the symmetric part of the stress field. He studied both surface and plate waves in a nonuniformly stressed medium by using perturbation theory and Lagrangian descriptions of particle motion [65]. Qu and Liu in 1998 [66] considered changes in dispersion curves for waves in a stressed aluminum plate relative to the unloaded state.

One drawback in the use of Rayleigh waves in acoustoelasticity applications is the limitation to smooth surfaces while Lamb waves are limited to plate-like structures. Guided wave acoustoelasticity work reported in the literature has focused more on the measurement of acoustoelastic constants rather than TOECs. It appears that theory needs to be developed to recover TOECs using guided wave methods.

2.6 Other Techniques in Acoustoelasticity and TOEC Recovery

In addition to the ultrasonic methods mentioned previously, there are a few other methods to determine TOECs and account for the acoustoelastic effect. Some non-ultrasonic methods include optical techniques, i.e., stress-induced optical birefringence, which requires transparent materials [67]. Deformation theory using finite strain

elasticity theory has also been used to obtain TOECs for hexagonal boron nitride by Mathew et al. [68]. Expressions were derived using sublattice displacements up to the first order in strains and considered interactions up through second neighbor atoms. The potential energy expression obtained is the expansion of the squares of vector distances and leads to a term with harmonic and anharmonic parameters. Since TOECs are related to thermal expansion, relations between constants are obtained from this anharmonic behavior such as in [69]. Researchers have also looked at deviations from Hooke's law and determined TOECs from the nonlinearity in the stress-strain relationship [70].

Other ultrasonic-based methods include measuring the acoustoelastic effect with line focus beam (LFB) acoustic microscopy where defocusing separates signals in time. A description of the technique is provided by Briggs [71]. Sometimes elastic moduli recovery for anisotropic materials required destructive methods. Acquiring certain wave speed measurements involved machining the material for samples in specific directions and applying traditional normal incidence techniques [72]. Berruti et al. favorably compared the acoustoelastic effects in an aluminum alloy using LFB microscopy and a point contact method [62]. Theory for recovering TOECs using LFB microscopy has not been reported.

Another ultrasonic method used in the recovery of TOECs is the harmonic generation approach. For a given monotone sinusoidal input waveform to the material, output is of the form that shows the second harmonic generation in the 2nd term [15]:

$$y(x,t) = A_1 \cos(kx - \omega t) - \frac{c_2}{8c_1} k^2 A_1^2 x \cos 2(kx - \omega t) + \cdots, \tag{2.8}$$

$$\beta = \left(\frac{A_2}{A_1^2}\right)\frac{8c^2}{\omega^2 a}, \qquad A_2 = -\frac{c_2}{8c_1} A_1^2 x, \tag{2.9}$$

where A_1 is the amplitude of the fundamental, A_2 the amplitude of the second harmonic, and a is the propagation distance in the medium. The relation between the nonlinearity parameter β and TOECs is shown in Equation (2.10) for the 1D case (longitudinal bulk waves) for an isotropic material [7].

$$\beta = -\frac{3(\lambda + 2\mu) + C_{111111}}{\lambda + 2\mu} \tag{2.10}$$

A more detailed discussion of finite amplitude ultrasonics is found in [12, 15, 73].

The widely used method of tone burst excitation followed by the detection of higher-order harmonics has the drawback of relying upon amplitude measurements and it is difficult to accurately and repeatedly capture the effects [40]. Generally, most TOEC recovery methods do not provide a complete set of TOECs compared to ultrasonic acoustoelasticity methods [74]. Hence, combinations of harmonic measurements and stress or pressure derivatives have been used to determine all TOECs for both isotropic and cubic symmetries [75]. Harmonic methods were also combined with ultrasonic frequency mixing methods to recover TOECs [76]. Two waves with different frequencies have a nonlinear interaction, which leads to the generation of sum and difference frequencies. The amplitudes of these new frequency components are dependent on TOECs of the media.

2.7 Section Summary

This background review has considered nonlinear ultrasonics in general, acoustoelasticity in particular, and existing techniques for TOEC recovery. Acoustoelasticity relies on changes in velocity that can be determined accurately, and measurements are feasible for in situ implementation. Overall, nonlinear ultrasonic

methods hold great potential in examining early microstructural changes in damage evolution and general material characterization. Nonlinear effects carry a much broader spectrum of information on material properties compared to linear effects and thus offer the potential to extend the scope of existing NDE methods.

TOECs are hard to measure and traditional TOEC measurement methods have been challenging because of the fixture designs required to achieve transducer alignment and different wave modes for both hydrostatic and uniaxial loads. Existing methods are generally not suitable for either in situ implementation or accurate repeated measurements to track damage.

Overall, no one-sided acoustoelasticity application using angle-beam bulk waves in a contact configuration for TOEC recovery has been found in the literature. Further information on the development of acoustoelastic theory can be found in [7, 15]. Angle-beam methods are applicable for one-sided access and are considered in this research for accurate and repeatable recovery methods for isotropic parallel faced materials. The background work also points to the need for a complete sensitivity analysis for TOEC recovery via acoustoelasticity to provide a better understanding of the accuracy of the recovered constants.

CHAPTER 3

THEORY DEVELOPMENT AND FORWARD PROBLEM

This chapter considers the forward problem of calculating both the velocity change and time shift as a function of applied load for two angle-beam configurations, namely one with attached (i.e. glued on) transducers and the other with floating (i.e. liquid coupled) transducers. The main assumptions are that the material is homogeneous and isotropic, the phase and group velocities are equal (no dispersion). It is also assumed that the material is hyperelastic (i.e., the stress-strain relationship is derived from a strain energy function), and specimens have parallel surfaces.

Acoustoelasticity theory in general is reviewed, and the angle beam problem is defined and developed. Note that the general theory of acoustoelasticity is well developed and applies to all angles and all modes (longitudinal and shear) of bulk wave propagation. In general, the speed of propagation of a particular wave mode propagating at a particular angle depends upon both the applied stress and the third order elastic constants. Measuring the change in wave speed with stress thus provides a means of determining the third order elastic constants. The purpose of this chapter is to provide complete derivations of the change in wave speed with stress for specific angle beam cases not found in the literature. In practice, wave speeds are not measured directly but are derived from changes in times-of-flight. Therefore specific equations for changes in time-of-flight are also derived that highlight differences in the attached and floating transducer configurations.

3.1 Ultrasonic Waves in Stressed Solids

This specific problem is that of a small amplitude elastic wave superimposed on the static deformation of an elastic solid. It specifically considers propagation of elastic waves at an angle to an applied uniaxial stress as a function of applied stress. In 1961 Toupin and Bernstein [24] considered hyperelastic materials of arbitrary symmetry and defined three states for ultrasonic waves in stressed media: (1) the stress free original state (i.e. free or natural state), (2) the statically stressed and deformed (initial) state (i), and (3) a final state (f) when the dynamic elastic wave motion acts on the deformed material. Deformation from the initial to final state is much smaller than the static deformation from the natural to the initial state, although the initial deformation is elastic. It is assumed that the material is hyperelastic. i.e. its constitutive relation can be developed from a strain energy function.

Theory is reviewed for a small amplitude ultrasonic wave superimposed on an initially isotropic stressed solid. Equations of motion are then developed which describe propagation of bulk waves in such a solid. Following derivations of Pao et al. [46, 77], and later by Dorfi et al. [57], coordinates of a material point in the natural, initial and final states are represented by the position vectors **a**, **X** and **x**, respectively. Components of quantities referring to the natural state are given by Greek subscripts (e.g., α, β); those referring to the initial state are given by uppercase Roman subscripts (e.g., I, J); and those referring to the final state by lowercase Roman subscripts (e.g., i, j). Thus, a_α, X_J and x_j are components of the position vectors in the natural, initial and final systems, respectively.

Displacements of a material point from the natural to initial states, and natural to final states, are given by $\mathbf{u}^{\mathbf{i}}$ and $\mathbf{u}^{\mathbf{f}}$:

$$\mathbf{u}^{\mathbf{i}}(\mathbf{a}) = \mathbf{X} - \mathbf{a}, \quad \mathbf{u}^{\mathbf{f}}(\mathbf{a},t) = \mathbf{x} - \mathbf{a}. \tag{3.1}$$

The dynamic displacement associated with the superimposed wave motion is the difference between the final state and the initial state:

$$\mathbf{u}(\mathbf{a},t) = \mathbf{x}(\mathbf{a},t) - \mathbf{X}(\mathbf{a}) = \mathbf{u}^{\mathbf{f}}(\mathbf{a},t) - \mathbf{u}^{\mathbf{i}}(\mathbf{a}). \tag{3.2}$$

The above equation is expressed in terms of the natural coordinates **a**, and the goal is to obtain the equation of motion for the dynamic displacement **u**(**a**,t).

The physical stress at a particular material point is given by the Cauchy stress tensor **t**, whose components are t^{i}_{JK} for the initial state and t^{f}_{jk} for the final state. These components are expressed in the initial and final coordinate systems, respectively. It is convenient to work in the natural coordinate system, and to do so the Cauchy stress tensors are related to second Piola-Kirchoff stress tensors, which are defined in the natural system,

$$t^{\mathrm{i}}_{JK} = \frac{1}{J^{\mathrm{i}}}\frac{\partial X_K}{\partial a_\beta}\frac{\partial X_J}{\partial a_\alpha}T^{\mathrm{i}}_{\alpha\beta}, \text{ and } t^{f}_{ij} = \frac{1}{J^{\mathrm{f}}}\frac{\partial x_i}{\partial a_\alpha}\frac{\partial x_j}{\partial a_\beta}T^{\mathrm{f}}_{\alpha\beta} = \frac{1}{J^{\mathrm{F}}}\frac{\partial x_i}{\partial X_K}\frac{\partial x_j}{\partial X_L}T^{\mathrm{f}}_{KL}. \tag{3.3}$$

Here J^{i} is the determinant of the matrix $\partial X_J/\partial a_\alpha$ (J,α = 1,2,3), and similarly J^{f} and J^{F} are the determinants of the matrices $\partial x_j/\partial a_\alpha$ and $\partial x_j/\partial X_K$, respectively. Note that summation over repeated indices is assumed here and in all equations.

The deformations can be expressed in terms of the displacements by using Eq. (3.1) and (3.2) to obtain,

$$\frac{\partial X_K}{\partial a_\beta} = \delta_{K\gamma}\left[\delta_{\gamma\beta} + \frac{\partial u^{\mathrm{i}}_\gamma}{\partial a_\beta}\right], \quad \frac{\partial x_i}{\partial X_K} = \delta_{iM}\left[\delta_{MK} + \frac{\partial u_M}{\partial X_K}\right], \text{ and } \frac{\partial x_i}{\partial a_\alpha} = \delta_{i\gamma}\left[\delta_{\alpha\gamma} + \frac{\partial u^{\mathrm{f}}_\gamma}{\partial a_\alpha}\right]. \tag{3.4}$$

The incremental stress caused by the elastic wave is $\mathbf{T} = \mathbf{T}^{\mathrm{f}} - \mathbf{T}^{\mathrm{i}}$ with components

$$T_{JK} = T^{\mathrm{f}}_{JK} - T^{\mathrm{i}}_{JK} \quad \text{and} \quad T_{\alpha\beta} = T^{\mathrm{f}}_{\alpha\beta} - T^{\mathrm{i}}_{\alpha\beta}. \tag{3.5}$$

The initial static deformation must satisfy the equation of equilibrium, which in the natural system of coordinates is,

$$\frac{\partial}{\partial a_\beta}\left[T^{\mathrm{i}}_{\beta a} + T^{\mathrm{i}}_{\beta\gamma}\frac{\partial u^{\mathrm{i}}_\alpha}{\partial a_\gamma}\right] = 0. \tag{3.6}$$

The final dynamic state (static deformation plus superimposed wave motion) must satisfy the equation of motion, which in the natural system of coordinates is,

$$\frac{\partial}{\partial a_\beta}\left[T^{\mathrm{f}}_{\beta a} + T^{\mathrm{f}}_{\beta\gamma}\frac{\partial u^{\mathrm{f}}_\alpha}{\partial a_\gamma}\right] = \rho^0\frac{\partial^2 u^{\mathrm{f}}_\alpha}{\partial t^2}. \tag{3.7}$$

The equation of motion for the incremental displacement in the natural coordinates, $\mathbf{u}(\mathbf{a},t)$, is obtained by subtracting Eq. (3.8) from Eq. (3.9),

$$\frac{\partial}{\partial a_\beta}\left[T_{\beta\alpha} + T_{\beta\gamma}\frac{\partial u_\alpha}{\partial a_\gamma} + T^{\mathrm{i}}_{\beta\gamma}\frac{\partial u_\alpha}{\partial a_\gamma} + T_{\beta\gamma}\frac{\partial u^{\mathrm{i}}_\alpha}{\partial a_\gamma}\right] = \rho^0\frac{\partial^2 u_\alpha}{\partial t^2}. \tag{3.8}$$

This equation is further simplified by neglecting the second term inside the brackets, which is a product of two very small quantities,

$$\frac{\partial}{\partial a_\beta}\left[T_{\beta\alpha} + T^{\mathrm{i}}_{\beta\gamma}\frac{\partial u_\alpha}{\partial a_\gamma} + T_{\beta\gamma}\frac{\partial u^{\mathrm{i}}_\alpha}{\partial a_\gamma}\right] = \rho^0\frac{\partial^2 u_\alpha}{\partial t^2}. \tag{3.9}$$

This is the incremental equation of motion. Since no assumptions have been made regarding the strain, this equation applies for both elastic and plastic strains.

The Lagrangian strain tensors (in the natural coordinates) for the initial and final states are defined as:

$$E^{\mathrm{i}}_{\alpha\beta} = \frac{1}{2}\left(\frac{\partial u^{\mathrm{i}}_\alpha}{\partial a_\beta} + \frac{\partial u^{\mathrm{i}}_\beta}{\partial a_\alpha} + \frac{\partial u^{\mathrm{i}}_\lambda}{\partial a_\alpha}\frac{\partial u^{\mathrm{i}}_\lambda}{\partial a_\beta}\right), \quad E^{\mathrm{f}}_{\alpha\beta} = \frac{1}{2}\left(\frac{\partial u^{\mathrm{f}}_\alpha}{\partial a_\beta} + \frac{\partial u^{\mathrm{f}}_\beta}{\partial a_\alpha} + \frac{\partial u^{\mathrm{f}}_\lambda}{\partial a_\alpha}\frac{\partial u^{\mathrm{f}}_\lambda}{\partial a_\beta}\right). \tag{3.10}$$

If it is assumed that the superimposed wave motion is small, then the difference of the two strain tensors becomes,

$$E_{\alpha\beta} = E^{\mathrm{f}}_{\alpha\beta} - E^{\mathrm{i}}_{\alpha\beta} = \frac{1}{2}\left(\frac{\partial u_a}{\partial a_\beta} + \frac{\partial u_b}{\partial a_\alpha} + \frac{\partial u^{\mathrm{i}}_\lambda}{\partial a_\alpha}\frac{\partial u_\lambda}{\partial a_\beta} + \frac{\partial u_\lambda}{\partial a_\alpha}\frac{\partial u^{\mathrm{i}}_\lambda}{\partial a_\beta} \right). \tag{3.11}$$

For a hyperelastic material, a constitutive relation can be developed from a strain energy function [26]. If this strain energy function is expanded about the state of zero strain and the first two terms are kept, the following constitutive equation for the initial and final states is obtained,

$$T^{\mathrm{i}}_{\alpha\beta} = c_{\alpha\beta\gamma\delta}E^{\mathrm{i}}_{\gamma\delta} + \frac{1}{2}c_{\alpha\beta\gamma\delta\varepsilon\eta}E^{\mathrm{i}}_{\gamma\delta}E^{\mathrm{i}}_{\varepsilon\eta} \quad \text{and} \quad T^{\mathrm{f}}_{\alpha\beta} = c_{\alpha\beta\gamma\delta}E^{\mathrm{f}}_{\gamma\delta} + \frac{1}{2}c_{\alpha\beta\gamma\delta\varepsilon\eta}E^{\mathrm{f}}_{\gamma\delta}E^{\mathrm{f}}_{\varepsilon\eta}\,. \tag{3.12}$$

The $c_{\alpha\beta\gamma\delta}$ are the second order elastic constants, and the $c_{\alpha\beta\gamma\delta\varepsilon\eta}$ are the third order elastic constants, which are neglected for the linear theory of elasticity. A constitutive equation for the incremental stress tensor is found by subtracting $\mathbf{T}^{\mathrm{i}}$ from $\mathbf{T}^{\mathrm{f}}$,

$$\begin{aligned} T_{\alpha\beta} &= T^{\mathrm{f}}_{\alpha\beta} - T^{\mathrm{i}}_{\alpha\beta} \\ &= c_{\alpha\beta\gamma\delta}E^{\mathrm{f}}_{\gamma\delta} + \frac{1}{2}c_{\alpha\beta\gamma\delta\varepsilon\eta}E^{\mathrm{f}}_{\gamma\delta}E^{\mathrm{f}}_{\varepsilon\eta} - c_{\alpha\beta\gamma\delta}E^{\mathrm{i}}_{\gamma\delta} - \frac{1}{2}c_{\alpha\beta\gamma\delta\varepsilon\eta}E^{\mathrm{i}}_{\gamma\delta}E^{\mathrm{i}}_{\varepsilon\eta} \\ &= c_{\alpha\beta\gamma\delta}E_{\gamma\delta} + \frac{1}{2}c_{\alpha\beta\gamma\delta\varepsilon\eta}\left[E^{\mathrm{i}}_{\gamma\delta}E^{\mathrm{i}}_{\varepsilon\eta} + E^{\mathrm{i}}_{\gamma\delta}E_{\varepsilon\eta} + E_{\gamma\delta}E^{\mathrm{i}}_{\varepsilon\eta} + E_{\gamma\delta}E_{\varepsilon\eta} - E^{\mathrm{i}}_{\gamma\delta}E^{\mathrm{i}}_{\varepsilon\eta} \right] \\ &= c_{\alpha\beta\gamma\delta}E_{\gamma\delta} + c_{\alpha\beta\gamma\delta\varepsilon\eta}\left[E^{\mathrm{i}}_{\gamma\delta}E_{\varepsilon\eta} + \frac{1}{2}E_{\gamma\delta}E_{\varepsilon\eta} \right]. \end{aligned} \tag{3.13}$$

To be consistent with the approximation of Eq. (3.12), the second term inside the brackets is neglected (product of two small quantities), and the infinitesimal strain tensor $e_{\alpha\beta}$ is used for the first term inside the brackets, yielding

$$T_{\alpha\beta} = c_{\alpha\beta\gamma\delta}E_{\gamma\delta} + c_{\alpha\beta\gamma\delta\varepsilon\eta}e^{\mathrm{i}}_{\gamma\delta}e_{\varepsilon\eta} \tag{3.14}$$

with

$$e_{\alpha\beta} = \frac{1}{2}\left[\frac{\partial u_\alpha}{\partial a_\beta} + \frac{\partial u_\beta}{\partial a_\alpha}\right] \quad \text{and} \quad e^{\mathrm{i}}_{\alpha\beta} = \frac{1}{2}\left[\frac{\partial u^{\mathrm{i}}_\alpha}{\partial a_\beta} + \frac{\partial u^{\mathrm{i}}_\beta}{\partial a_\alpha}\right]. \tag{3.15}$$

The constitutive equation in terms of displacement gradients is obtained by substituting Eqs. (3.11) and (3.15) into Eq. (3.14) and is

$$T_{\alpha\beta} = c_{\alpha\beta\gamma\delta}\left(\delta_{\rho\gamma} + \frac{\partial u^{\mathrm{i}}_\rho}{\partial a_\gamma}\right)\frac{\partial u_\rho}{\partial a_\delta} + c_{\alpha\beta\gamma\delta\varepsilon\eta}\frac{\partial u^{\mathrm{i}}_\gamma}{\partial a_\delta}\frac{\partial u_\varepsilon}{\partial a_\eta}. \tag{3.16}$$

The equation of motion for **u**(**a**,t), is obtained by substituting Eq. (3.16) into Eq. (3.9),

$$\frac{\partial}{\partial a_\beta}\left(T^i_{\beta\gamma}\frac{\partial u_\alpha}{\partial a_\gamma} + \Gamma_{\alpha\beta\gamma\delta}\frac{\partial u_\gamma}{\partial a_\delta}\right) = \rho^o\frac{\partial^2 u_\alpha}{\partial t^2}, \tag{3.17}$$

where

$$\Gamma_{\alpha\beta\gamma\delta} = c_{\alpha\beta\gamma\delta} + c_{\alpha\beta\rho\delta}\frac{\partial u^i_\gamma}{\partial a_\rho} + c_{\rho\beta\gamma\delta}\frac{\partial u^i_\alpha}{\partial a_\rho} + c_{\alpha\beta\gamma\delta\varepsilon\eta}\,e^i_{\varepsilon\eta}. \tag{3.18}$$

For homogeneous initial deformation, the equation of motion becomes,

$$A_{\alpha\beta\gamma\delta}\frac{\partial^2 u_\gamma}{\partial a_\beta \partial a_\delta} = \rho_o \ddot{u}_\alpha \tag{3.19}$$

where

$$A_{\alpha\beta\gamma\delta} = T^i_{\beta\delta}\delta_{\alpha\gamma} + \Gamma_{\alpha\beta\gamma\delta} = c_{\beta\delta\lambda\rho}e^{\mathrm{i}}_{\lambda\rho}\delta_{\alpha\gamma} + c_{\alpha\beta\gamma\delta} + c_{\alpha\beta\rho\delta}\frac{\partial u^i_\gamma}{\partial a_\rho} + c_{\rho\beta\gamma\delta}\frac{\partial u^i_\alpha}{\partial a_\rho} + c_{\alpha\beta\gamma\delta\varepsilon\eta}\,e^i_{\varepsilon\eta}. \tag{3.20}$$

For an isotropic material, there are two independent second order elastic constants and three independent third order elastic constants. The second order elastic constants λ and μ (Lamé constants) are related to the $c_{\alpha\beta\gamma\delta}$ by

$$C_{\alpha\beta\gamma\delta} = \lambda\delta_{\alpha\beta}\delta_{\gamma\delta} + \mu\left(\delta_{\alpha\gamma}\delta_{\beta\delta} + \delta_{\alpha\delta}\delta_{\beta\gamma}\right). \tag{3.21}$$

The third order elastic constants l, m and n (Murnagan constants) are related to the $c_{\alpha\beta\gamma\delta\varepsilon\eta}$ by [15],

$$C_{\alpha\beta\gamma\delta\varepsilon\eta} = 2\left(l - m + \frac{n}{2}\right)\delta_{\alpha\beta}\delta_{\gamma\delta}\delta_{\varepsilon\eta} + 2\left(m - \frac{n}{2}\right)\left(\delta_{\alpha\beta}I_{\gamma\delta\varepsilon\eta} + \delta_{\gamma\delta}I_{\varepsilon\eta\alpha\beta} + \delta_{\varepsilon\eta}I_{\alpha\beta\gamma\delta}\right) + \frac{n}{2}\left(\delta_{\alpha\gamma}I_{\beta\delta\varepsilon\eta} + \delta_{\alpha\delta}I_{\beta\gamma\varepsilon\eta} + \delta_{\beta\gamma}I_{\alpha\delta\varepsilon\eta} + \delta_{\beta\delta}I_{\alpha\gamma\varepsilon\eta}\right). \tag{3.22}$$

where

$$I_{\alpha\beta\gamma\delta} = \frac{\left(\delta_{\alpha\gamma}\delta_{\beta\delta} + \delta_{\alpha\delta}\delta_{\beta\gamma}\right)}{2}\ . \tag{3.23}$$

The relationships between commonly used TOECs for isotropic solids are summarized in Table 2.1.

3.2 Formulation of the Angle-Beam Acoustoelasticity Problem

Bulk waves propagating at a refracted angle θ are shown for the angle-beam configuration illustrated in Figure 3.1. Axes x_1, x_2, and x_3 are parallel to the principal stress directions, with a uniaxial load applied in the x_1 direction. Wave propagation is in the $x_1 - x_2$ plane, with polarization in the $x_1 - x_2$ plane for the longitudinal (L) and shear vertical (SV) waves, and polarization in the x_3 direction for shear horizontal (SH) waves.

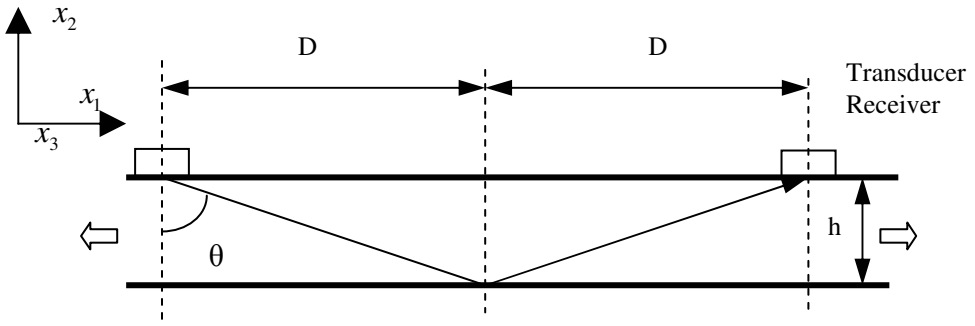

Figure 3.1. Sample of thickness *h* with a single "V" angle-beam path of refracted angle θ.

Multiple measurements must be performed to recover the three TOECs for an isotropic material. Considered here are L, SV and SH waves propagating along the angle

beam path shown in Figure 3.1. A new coordinate system is defined with the x_1 axis aligned along the direction of propagation. The derivation steps follows the theory given by Pao et al. [77] for the propagation of plane elastic waves in a homogeneous medium with initial strains as reviewed in section 3.1. Referring to Equation (3.19), which is the equation of motion in the natural (unstrained) coordinates, a_i are the coordinates, u_α are the components of displacement, and ρ^0 is the density in the natural state.

Consider a plane wave propagating in the a_1 direction with frequency ω, wavenumber k, and polarization **U**,

$$u_\lambda = U_\lambda \exp[i(ka_1 - \omega t]. \tag{3.24}$$

If this expression is substituted into Eq. (3.19), the following equation results,

$$\left[A_{\alpha 1 \gamma 1} - \rho^0 c^2\right] U_\gamma = 0, \tag{3.25}$$

where the wavespeed c is equal to ω/k. In matrix form this equation becomes,

$$\begin{bmatrix} A_{1111} - \rho^0 c^2 & A_{1121} & A_{1131} \\ A_{2111} & A_{2121} - \rho^0 c^2 & A_{1131} \\ A_{3111} & A_{3121} & A_{3131} - \rho^0 c^2 \end{bmatrix} \begin{bmatrix} U_1 \\ U_2 \\ U_3 \end{bmatrix} = \begin{bmatrix} 0 \\ 0 \\ 0 \end{bmatrix} \tag{3.26}$$

This equation has non-zero solutions only if the determinant of the matrix is zero. The eigenvalues are related to the wavespeeds (i.e., ρc^2), and the eigenvectors (U_α) are the polarizations. This result is identical to that derived in [38].

For the problem considered here, the direction of applied load is not the same as the wave propagation direction. The stress tensor in the original coordinate system of Figure 3.1 resulting from a uniaxial stress of σ is given by

$$\tilde{\sigma} = \begin{bmatrix} \sigma & 0 & 0 \\ 0 & 0 & 0 \\ 0 & 0 & 0 \end{bmatrix}, \tag{3.27}$$

The rotation matrix R is,

$$R = \begin{bmatrix} \sin\theta & \cos\theta & 0 \\ -\cos\theta & \sin\theta & 0 \\ 0 & 0 & 1 \end{bmatrix}. \tag{3.28}$$

Therefore the stress tensor in the rotated system (along the direction of propagation) is $\sigma_{ij} = r_{ik}\, r_{jl}\, \sigma_{kl}$, which reduces to,

$$\tilde{\sigma} = \begin{bmatrix} \sigma\sin^2\theta & -\sigma\sin\theta\cos\theta & 0 \\ -\sigma\sin\theta\cos\theta & \sigma\cos^2\theta & 0 \\ 0 & 0 & 0 \end{bmatrix} \tag{3.29}$$

Since the stresses in the rotated coordinate system are known, the strains in this system can by computed by inverting the following system of equations,

$$\begin{bmatrix} \sigma_1 \\ \sigma_2 \\ \sigma_3 \\ \sigma_4 \\ \sigma_5 \\ \sigma_6 \end{bmatrix} = \begin{bmatrix} \sigma\sin^2\theta \\ \sigma\cos^2\theta \\ 0 \\ 0 \\ 0 \\ -\sigma\sin\theta\cos\theta \end{bmatrix} = \begin{bmatrix} c_{11} & c_{12} & c_{13} & 0 & 0 & 0 \\ c_{12} & c_{22} & c_{11} & 0 & 0 & 0 \\ c_{13} & c_{23} & c_{33} & 0 & 0 & 0 \\ 0 & 0 & 0 & 2c_{44} & 0 & 0 \\ 0 & 0 & 0 & 0 & 2c_{55} & 0 \\ 0 & 0 & 0 & 0 & 0 & 2c_{66} \end{bmatrix} \begin{bmatrix} e_1 \\ e_2 \\ e_3 \\ e_4 \\ e_5 \\ e_6 \end{bmatrix}. \tag{3.30}$$

Voigt's contracted notation is used where $e_1 = e_{11}$, $e_2 = e_{22}$, $e_3 = e_{33}$, $e_4 = e_{23} = e_{32}$, $e_5 = e_{13} = e_{31}$, and $e_6 = e_{12} = e_{21}$. Note that the elastic constants are $c_{11} = c_{22} = c_{33} = \lambda + 2\mu$, $c_{12} = c_{13} = c_{23} = c_{21} = c_{31} = c_{32} = \lambda$, and $c_{44} = c_{55} = c_{66} = \mu$ as per Table 2.1.

The strain components in the rotated system are calculated in terms of the Lamé constants as follows;

$$
\begin{aligned}
e_1 &= \sigma \frac{2(\lambda+\mu)\sin^2\theta - \lambda\cos^2\theta}{2\mu(3\lambda+2\mu)} \\
e_2 &= \sigma \frac{-\lambda\sin^2\theta - 2(\lambda+\mu)\cos^2\theta}{2\mu(3\lambda+2\mu)} \\
e_3 &= \sigma \frac{-\lambda}{2\mu(3\lambda+2\mu)} \\
e_6 &= \sigma \frac{-\sin\theta\cos\theta}{2\mu} \\
e_4 &= e_5 = 0
\end{aligned}
\tag{3.31}
$$

These are the initial strains needed to compute $\mathbf{e}^{\mathrm{i}}$ and $\mathbf{u}^{\mathrm{i}}$ in Eq. (3.20).

3.2.1 Longitudinal Wave Acoustoelastic Constants

Derivation of longitudinal (L) wave acoustoelastic constants is first undertaken where the particle motion (polarization) is along the direction of propagation. In general, two quasi-shear wave modes and one quasi-L wave more are obtained from the three eigenvalues. For the L wave, the eigenvector that is primarily in the x_1 direction is considered, and the strain component along this direction is e_1. Referring to Eq. (3.26), the off-diagonal terms are very small, and thus the eigenvalue corresponding to the A_{1111} term provides a good estimate of the L wave velocity. Interest is in the wave speed, hence the small difference between the quasi and pure mode and the eigenvectors can be ignored since the equation is not being solved exactly. Therefore, from Equation (3.20),

$$
A_{1111} = c_{11\lambda\rho}e^{\mathrm{i}}_{\lambda\rho} + c_{1111} + c_{11\rho1}\frac{\partial u_1^i}{\partial a_\rho} + c_{\rho111}\frac{\partial u_1^i}{\partial a_\rho} + c_{1111\varepsilon\eta}\, e^i_{\varepsilon\eta}. \tag{3.32}
$$

After conversion to Voigt notation for both second and third order elastic constants, ignoring rotation terms, and some algebra,

$$
A_{1111} = c_{11} + (3c_{11} + c_{111})e^{\mathrm{i}}_{11} + (c_{12} + c_{112})e^{\mathrm{i}}_{22} + (c_{13} + c_{113})e^{\mathrm{i}}_{33}. \tag{3.33}
$$

This equation can be expressed as a function of the applied stresses by substituting the strains of Eq. (3.31). The relationships of Table 2.1 are used to express the elastic constants in terms of λ, μ, l, m and n. The final expression for A_{1111} becomes,

$$A_{1111} = \lambda + 2\mu + \sigma_{11}\left[\frac{2\lambda^2 + 9\lambda\mu + 6\mu^2 + 2l\mu + 4m\lambda + 4m\mu}{\mu(3\lambda + 2\mu)}\right] + \sigma_{22}\left[\frac{-\lambda^2 - 2\lambda\mu + 2l\mu - 2m\lambda}{\mu(3\lambda + 2\mu)}\right]. \tag{3.34}$$

The longitudinal velocity in the natural coordinates is then calculated as $c_L = \sqrt{A_{1111}/\rho^0}$,

$$c_L = \left\{\frac{\lambda + 2\mu}{\rho^0} + \sigma_{11}\left[\frac{2\lambda^2 + 9\lambda\mu + 6\mu^2 + 2l\mu + 4m\lambda + 4m\mu}{\rho^0\mu(3\lambda + 2\mu)}\right] + \sigma_{22}\left[\frac{-\lambda^2 - 2\lambda\mu + 2l\mu - 2m\lambda}{\rho^0\mu(3\lambda + 2\mu)}\right]\right\}^{1/2}. \tag{3.35}$$

After some algebra, it can be expressed as,

$$c_L = \sqrt{\frac{\lambda + 2\mu}{\rho^0}}\left\{1 + \frac{\sigma_{11}\left(2\lambda^2 + 9\lambda\mu + 6\mu^2 + 2l\mu + 4m\lambda + 4m\mu\right)}{\mu(\lambda + 2\mu)(3\lambda + 2\mu)} + \frac{\sigma_{22}\left(-\lambda^2 - 2\lambda\mu + 2l\mu - 2m\lambda\right)}{\mu(\lambda + 2\mu)(3\lambda + 2\mu)}\right\}^{1/2}. \tag{3.35}$$

Recognizing that the stress-induced terms are much smaller than the first term, the velocity can be approximated as,

$$c \cong \sqrt{\frac{\lambda + 2\mu}{\rho_o}}\left[1 + \frac{\sigma_{11}\left(2\lambda^2 + 9\lambda\mu + 6\mu^2 + 2l\mu + 4m\lambda + 4m\mu\right)}{2\mu(\lambda + 2\mu)(3\lambda + 2\mu)} + \frac{\sigma_{22}\left(-\lambda^2 - 2\lambda\mu + 2l\mu - 2m\lambda\right)}{2\mu(\lambda + 2\mu)(3\lambda + 2\mu)}\right] = c_L^0\left(1 + \frac{\Delta c_L}{c_L^0}\right). \tag{3.35}$$

The longitudinal velocity in the natural (unstrained) system is $c_L^0 = \sqrt{(\lambda + 2\mu)/\rho^0}$.

For the case of interest here, the stresses are $\sigma_{11}=\sigma\sin^2\theta$, $\sigma_{22}=\sigma\cos^2\theta$, where σ is the uniaxial stress. The change of velocity can then be expressed as,

$$\begin{aligned}\frac{\Delta c_{\mathrm{L}}}{c_{\mathrm{L}}^0}&=\sigma\left[\begin{array}{c}\dfrac{\sin^2\theta\left(2\lambda^2+9\lambda\mu+6\mu^2+2l\mu+4m\lambda+4m\mu\right)}{2\mu\left(\lambda+2\mu\right)\left(3\lambda+2\mu\right)}\\ +\dfrac{\cos^2\theta\left(-\lambda^2-2\lambda\mu+2l\mu-2m\lambda\right)}{2\mu\left(\lambda+2\mu\right)\left(3\lambda+2\mu\right)}\end{array}\right]\\&=\sigma\left[\tilde{K}_1^{\mathrm{L}}\sin^2\theta+\tilde{K}_2^{\mathrm{L}}\cos^2\theta\right]\\&=\sigma\tilde{K}^{\mathrm{L}}(\theta)\end{aligned}\quad . \tag{3.36}$$

Here $\tilde{K}_1^{\mathrm{L}}$ and $\tilde{K}_2^{\mathrm{L}}$ are the acoustoelastic constants for longitudinal velocity changes in the natural system,

$$\tilde{K}_1^{L}=\frac{2\lambda^2+9\lambda\mu+6\mu^2+2l\mu+4(\lambda+\mu)m}{2\mu(\lambda+2\mu)(3\lambda+2\mu)}, \tag{3.37}$$

$$\tilde{K}_2^{L}=\frac{-\lambda(\lambda+2\mu)+2\mu l-2\lambda m}{2\mu(\lambda+2\mu)(3\lambda+2\mu)}. \tag{3.38}$$

To obtain acoustoelastic constants in the initial system, a correction term must be applied to obtain the velocity in the strained coordinate system to compensate for the change in path length resulting from the initial strain,

$$c_{\mathrm{L}}^{\mathrm{i}}\cong c_{\mathrm{L}}\left(1+e_{11}\right)\cong c_{\mathrm{L}}^0\left(1+\frac{\Delta c_{\mathrm{L}}}{c_{\mathrm{L}}^0}\right)\left(1+e_{11}\right)\cong c_{\mathrm{L}}^0\left(1+\frac{\Delta c_{\mathrm{L}}}{c_{\mathrm{L}}^0}+e_{11}\right). \tag{3.39}$$

Substituting e_{11} from Equation (3.31) yields,

$$c_{\mathrm{L}}^{\mathrm{i}}\cong\sqrt{\frac{\lambda+2\mu}{\rho}}\left\{\begin{array}{c}1+\sigma\sin^2\theta\left[\dfrac{4\lambda^2+15\lambda\mu+10\mu^2+2\mu l+4(\lambda+\mu)m}{2\mu(\lambda+2\mu)(3\lambda+2\mu)}\right]\\ +\sigma\cos^2\theta\left[\dfrac{-2\lambda(\lambda+2\mu)+2\mu l-2\lambda m}{2\mu(\lambda+2\mu)(3\lambda+2\mu)}\right]\end{array}\right\}. \tag{3.40}$$

Therefore, the longitudinal wave acoustoelastic constants in the initial (strained) system are,

$$K_1^{\mathrm{L}} = \frac{4\lambda^2 + 15\lambda\mu + 10\mu^2 + 2\mu l + 4(\lambda+\mu)m}{2\mu(\lambda+2\mu)(3\lambda+2\mu)} \tag{3.41}$$

and

$$K_2^{\mathrm{L}} = \frac{-2\lambda(\lambda+2\mu) + 2\mu l - 2\lambda m}{2\mu(\lambda+2\mu)(3\lambda+2\mu)}. \tag{3.42}$$

It is interesting to note that these constants have no dependence on *n*.

3.2.2 Shear Vertical Wave Acoustoelastic Constants

The shear vertical (SV) acoustoelastic constants can be derived in a similar manner as was done for L waves. For the SV wave, the particle motion is perpendicular to the direction of propagation and is in the x_1–x_2 plane. The starting point is Eq. (3.26), but the A_{2121} term is the one of interest. This derivation has been done by Mi et al. [38], and results are summarized here for completeness.

Velocity changes in both the natural and initial systems are of the same form as for the longitudinal velocity changes,

$$\begin{aligned} \frac{\Delta c_{\mathrm{SV}}}{c_{\mathrm{SV}}^0} &= \sigma\left[\tilde{K}_1^{\mathrm{SV}}\sin^2\theta + \tilde{K}_2^{\mathrm{SV}}\cos^2\theta\right] = \sigma\tilde{K}^{\mathrm{SV}}(\theta), \\ \frac{\Delta c_{\mathrm{SV}}^{\mathrm{i}}}{c_{\mathrm{SV}}^0} &= \sigma\left[K_1^{\mathrm{SV}}\sin^2\theta + K_2^{\mathrm{SV}}\cos^2\theta\right] = \sigma K^{\mathrm{SV}}(\theta). \end{aligned} \tag{3.43}$$

The two acoustoelastic constants representing SV velocity changes in the natural system are identical,

$$\tilde{K}_1^{\mathrm{SV}} = \tilde{K}_2^{\mathrm{SV}} = \frac{2\mu(\lambda+\mu) + \mu m + \lambda n/4}{2\mu^2(3\lambda+2\mu)}. \tag{3.44}$$

In the initial system they are no longer the same,

$$K_1^{SV} = \frac{4\mu(\lambda+\mu)+\mu m+\lambda n/4}{2\mu^2(3\lambda+2\mu)}, \tag{3.45}$$

$$K_2^{SV} = \frac{\mu(\lambda+2\mu)+\mu m+\lambda n/4}{2\mu^2(3\lambda+2\mu)}. \tag{3.46}$$

These constants have no dependence on *l*, and furthermore their dependence on *m* and *n* is not a function of angle. These constants were all reported in [38].

3.2.3 Shear Horizontal Wave Acoustoelastic Constants

In order to complete the bulk wave angle-beam acoustoelasticity theory, the shear horizontal (SH) wave follows a similar derivation. The particle motion for the SH wave is in the x_3 direction. Referring to Eq. (3.26), the term A_{3131} provides a good estimate of the SH wave velocity. From Eq. (3.20) and after some algebra,

$$A_{3131} = c_{55} + (c_{11} + c_{155})e_{11}^i + (c_{12} + c_{255})e_{22}^i + (c_{13} + 2c_{55} + c_{355})e_{33}^i \ . \tag{3.47}$$

After substituting for the strains and elastic constants, we have,

$$A_{3131} = \mu + \sigma_{11}\left[\frac{2\mu(\lambda+\mu)+\mu m+\lambda n/4}{\mu(3\lambda+2\mu)}\right] + \sigma_{22}\left[\frac{-\lambda\mu+\mu m-(\lambda+\mu)n/2}{\mu(3\lambda+2\mu)}\right]. \tag{3.48}$$

The SH wave speed is $c_{SH} = \sqrt{A_{3131}/\rho^0}$, which reduces to $\sqrt{\mu/\rho^0}$ when there is no applied load.

Following the same procedure as was done for the L wave, the acoustoelastic constants for SH wave velocity changes in the natural system are,

$$\tilde{K}_1^{SH} = \frac{2\mu(\lambda+\mu)+\mu m+\lambda n/4}{2\mu^2(3\lambda+2\mu)}, \tag{3.49}$$

$$\tilde{K}_2^{SH} = \frac{-\lambda\mu+\mu m-(\lambda+\mu)n/2}{2\mu^2(3\lambda+2\mu)}. \tag{3.50}$$

These can be mapped to the initial system as was done for the L wave in Eq. (3.39) by correcting for the strain along the direction of propagation, yielding acoustoelastic constants for changes in SH wave velocities in the initial system.

$$K_1^{\mathrm{SH}} = \frac{4\mu(\lambda+\mu)+\mu m+\lambda n/4}{2\mu^2(3\lambda+2\mu)}, \tag{3.51}$$

$$K_2^{\mathrm{SH}} = \frac{-2\lambda\mu+\mu m-(\lambda+\mu)n/2}{2\mu^2(3\lambda+2\mu)}. \tag{3.52}$$

Thus, changes in SH wave speeds follow the same form as for the L and SV waves:

$$\begin{aligned}\frac{\Delta c_{\mathrm{SH}}}{c_{\mathrm{SH}}^0} &= \sigma\left[\tilde{K}_1^{\mathrm{SH}}\sin^2\theta+\tilde{K}_2^{\mathrm{SH}}\cos^2\theta\right]=\sigma\tilde{K}^{\mathrm{SH}}(\theta),\\ \frac{\Delta c_{\mathrm{SH}}^{\mathrm{i}}}{c_{\mathrm{SH}}^0} &= \sigma\left[K_1^{\mathrm{SH}}\sin^2\theta+K_2^{\mathrm{SH}}\cos^2\theta\right]=\sigma K^{\mathrm{SH}}(\theta).\end{aligned} \tag{3.53}$$

3.2.4 Summary of Angle Beam Acoustoelastic Constants

All bulk wave acoustoelastic constants have been derived for wave speed changes in both the natural and initial coordinate systems. For all three wave modes (L, SV and SH) wave speed changes are of the same form,

$$\frac{\Delta c}{c^0} = \sigma\left[K_1\sin^2\theta+K_2\cos^2\theta\right]=\sigma K(\theta). \tag{3.54}$$

Acoustoelastic constants in the natural system are denoted by $\tilde{K}_{1,2}$ and those in the initial system by $K_{1,2}$. All constants are summarized in Table 3.1.

Table 3.1. Summary of acoustoelastic constants in the natural and initial systems.

Longitudinal (L) Wave Acoustoelastic Constants	
$\tilde{K}_1^L = \frac{2\lambda^2 + 9\lambda\mu + 6\mu^2 + 2\mu l + 4(\lambda+\mu)m}{2\mu(\lambda+2\mu)(3\lambda+2\mu)}$	$\tilde{K}_2^L = \frac{-\lambda(\lambda+2\mu) + 2\mu l - 2\lambda m}{2\mu(3\lambda+2\mu)(\lambda+2\mu)}$
$K_1^{\mathrm{L}} = \frac{4\lambda^2 + 15\lambda\mu + 10\mu^2 + 2\mu l + 4(\lambda+\mu)m}{2\mu(\lambda+2\mu)(3\lambda+2\mu)}$	$K_2^{\mathrm{L}} = \frac{-2\lambda(\lambda+2\mu) + 2\mu l - 2\lambda m}{2\mu(3\lambda+2\mu)(\lambda+2\mu)}$
Shear Vertical (SV) Wave Acoustoelastic Constants	
$\tilde{K}_1^{\mathrm{SV}} = \frac{2\mu(\lambda+\mu) + \mu m + \lambda n/4}{2\mu^2(3\lambda+2\mu)}$	$\tilde{K}_2^{\mathrm{SV}} = \frac{2\mu(\lambda+\mu) + \mu m + \lambda n/4}{2\mu^2(3\lambda+2\mu)}$
$K_1^{\mathrm{SV}} = \frac{4\mu(\lambda+\mu) + \mu m + \lambda n/4}{2\mu^2(3\lambda+2\mu)}$	$K_2^{\mathrm{SV}} = \frac{\mu(\lambda+2\mu) + \mu m + \lambda n/4}{2\mu^2(3\lambda+2\mu)}$
Shear Horizontal (SH) Wave Acoustoelastic Constants	
$\tilde{K}_1^{\mathrm{SH}} = \frac{2\mu(\lambda+\mu) + \mu m + \lambda n/4}{2\mu^2(3\lambda+2\mu)}$	$\tilde{K}_2^{\mathrm{SH}} = \frac{-\lambda\mu + \mu m - (\lambda+\mu)n/2}{2\mu^2(3\lambda+2\mu)}$
$K_1^{\mathrm{SH}} = \frac{4\mu(\lambda+\mu) + \mu m + \lambda n/4}{2\mu^2(3\lambda+2\mu)}$	$K_2^{\mathrm{SH}} = \frac{-2\lambda\mu + \mu m - (\lambda+\mu)n/2}{2\mu^2(3\lambda+2\mu)}$

The overall acoustoelastic constants $K(\theta)$ are graphically shown in Figure 3.2 where they are plotted as a function of refracted angle θ. Second and third order elastic constants for 7075 aluminum are used as reported by Stobbe [44]. As expected, the SV and SH wave acoustoelastic constants are the same at an angle of 90° (propagation along the loading direction), but are different for the normal incidence case of 0° (propagation perpendicular to the loading direction).

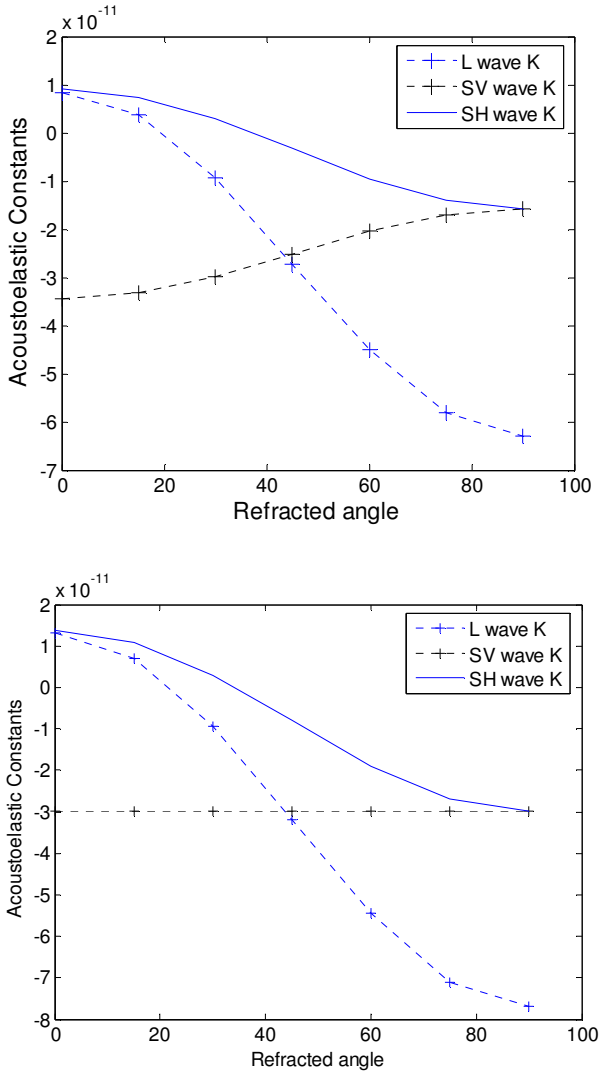

Figure 3.2. Variation of acoustoelastic constants with refracted angle in (a) initial and (b) natural systems.

3.3 Reconciliation with Prior Acoustoelastic Constants

Hughes and Kelly's fundamental work showed acoustoelastic velocity relations for shear and longitudinal waves propagating both parallel and perpendicular to the loading direction [31]. The literature survey in Chapter 2 indicated that most subsequent work utilized these equations. The paper by Dubuget et al. [55] is an exception as this work shows some acoustoelastic constants for oblique incidence propagation. The acoustoelastic constants derived in this thesis are compared to both researchers' work.

3.3.1 Parallel and Perpedicular Propagation using Stress Derivatives

In the oblique incidence formulation, propagation parallel and perpendicular to the applied loads corresponds to refracted angles of 90° and 0°, respectively, as illustrated in Figure 3.1. Equivalent equations are identified from Hughes and Kelly's work [31], and acoustoelastic constants are compared. This comparison is done by using the stress derivative approach, which considers the rate of change of the velocity with respect to the applied stress σ. The velocity equation is differentiated with respect to stress and is then rearranged to identify the acoustoelastic constants.

Equation (3.55), which is from Hughes and Kelly [31], represents a longitudinal (L) wave propagating parallel to the applied stress ($\theta = 90°$),

$$\rho^0 c_{1x}^2 = \lambda + 2\mu + \frac{\sigma}{3\lambda + 2\mu}\left[2l + \lambda + \frac{\lambda+\mu}{\mu}\left(4m + 4\lambda + 10\mu\right)\right]. \tag{3.55}$$

The first derivative with respect to stress yields

$$2\rho^0 c_{1x}\frac{dc_{1x}}{d\sigma} = \frac{2l + \lambda + \frac{\lambda+\mu}{\mu}\left(4m + 4\lambda + 10\mu\right)}{3\lambda + 2\mu}. \tag{3.56}$$

Setting $c_{1x} = c_{\mathrm{L}}^0 = \sqrt{(\lambda + 2\mu)/\rho^0}$ on the left hand side and dividing both sides by $\left(c_{\mathrm{L}}^0\right)^2$ results in,

$$\rho^0 \frac{1}{c_{\mathrm{L}}^0}\frac{dc_{1x}}{d\sigma} = \frac{2l + \lambda + \frac{\lambda+\mu}{\mu}\left(4m + 4\lambda + 10\mu\right)}{2\left(3\lambda + 2\mu\right)\left(\lambda + 2\mu\right)}\rho^0. \tag{3.57}$$

After rearranging terms, the acoustoelastic constant $K = \dfrac{\Delta c}{c\Delta\sigma}$ can be identified as,

$$K_1^{\mathrm{L}} = \frac{1}{c_{\mathrm{L}}^0}\frac{dc_{1x}}{d\sigma} = \frac{4\lambda^2 + 15\lambda\mu + 10\mu^2 + 2l\mu + 4(\lambda+\mu)m}{2\mu(\lambda+2\mu)(3\lambda+2\mu)} \ . \tag{3.58}$$

This expression matches that of the acoustoelastic constant derived earlier for L wave propagation at 90°; i.e. K_1^{L} of Table 3.1.

Equation (3.59), which is from Hughes and Kelly [31], represents an L wave propagating normal to applied stress; i.e, $\theta = 0°$,

$$\rho^0 c_{1y}^2 = \lambda + 2\mu + \frac{\sigma}{3\lambda+2\mu}\left[2l - \frac{2\lambda}{\mu}(m+\lambda+2\mu)\right]. \tag{3.59}$$

Via a similar manipulation,

$$K_2^{\mathrm{L}} = \frac{1}{c_{\mathrm{L}}^0}\frac{dc_{1y}}{d\sigma} = \frac{-2\lambda(\lambda+2\mu) + 2\mu l - 2\lambda m}{2\mu(\lambda+2\mu)(3\lambda+2\mu)}, \tag{3.60}$$

which is in agreement with the same constant in Table 3.1.

Equation (3.61), which is from Hughes and Kelly [31], represents a shear wave propagating parallel to the applied stress; i.e, $\theta = 90°$.

$$\rho^0 c_{2x}^2 = \mu + \frac{\sigma}{3\lambda+2\mu}\left(m + \frac{\lambda n}{4\mu} + 4\lambda + 4\mu\right). \tag{3.61}$$

Note that this configuration is the $\theta = 90°$ limiting case for both SV and SH waves in the angle beam formulation. After a similar manipulation,

$$K_1^{\mathrm{SV}} = K_1^{\mathrm{SH}} = \frac{1}{c_{\mathrm{SV,SH}}^0}\frac{dc_{2x}}{d\sigma} = \frac{4\mu(\lambda+\mu) + \mu m + \lambda n/4}{2\mu^2(3\lambda+2\mu)}. \tag{3.62}$$

This expression matches those of Table 3.1 for SV and SH waves propagating at 90°.

Equation (3.63), which is from Hughes and Kelly [31], represents a shear vertical (SV) wave propagating normal to the direction of applied stress;

$$\rho^0 c_{2y}^2 = \mu + \frac{\sigma}{3\lambda + 2\mu}\left(m + \frac{\lambda n}{4\mu} + \lambda + 2\mu \right). \tag{3.63}$$

The particle polarization is parallel to direction of applied load. In a similar manipulation,

$$K_2^{\mathrm{SV}} = \frac{1}{c_{\mathrm{SV}}^0}\frac{dc_{2y}}{d\sigma} = \frac{\mu(\lambda + 2\mu) + m\mu + \lambda n/4}{2\mu^2(3\lambda + 2\mu)}. \tag{3.64}$$

This expression matches that of Table 3.1.

Equation (3.65), which is from Hughes and Kelly [31], represents a shear horizontal (SH) wave propagating normal to the applied stress direction,

$$\rho^0 c_{2z}^2 = \mu + \frac{\sigma}{3\lambda + 2\mu}\left(m - \frac{\lambda + \mu}{2\mu} n - 2\lambda \right). \tag{3.65}$$

The particle polarization is normal to the direction of applied load and thus corresponds to the SH wave. Similarly,

$$K_2^{SH} = \frac{1}{c_{2x}}\frac{dc_{2x}}{d\sigma} = \frac{-2\lambda\mu - \frac{\lambda n}{2} + \mu m - \frac{\mu n}{2}}{2\mu^2(3\lambda + 2\mu)}, \tag{3.66}$$

matches the results of Table 3.1.

Hence all the equations derived here for $\theta = 0°$ and $\theta = 90°$ are in agreement with those of Hughes and Kelly.

3.3.2 Oblique Propagation Constants in the Literature

Dubuget et al. [55] has published acoustoelastic constants for oblique propagation, and this work can be regarded as the closest found to that presented here. As described in Chapter 2, an immersion system was used with the transducer rotated around the sample. Details of the derivations were not included, but this author feels

compelled to report the published acoustoelastic constants and compare them to those derived here.

For planes parallel to the applied uniaxial load, acoustoelastic constants for both L and S wave propagation are reported as,

$$A_{cl} = \frac{\sigma\left[l - \mu + (5\mu + 2\lambda + 2m)\left(\cos^2\theta + (3\cos^2\theta - 1)\frac{\lambda}{2\mu} \right) \right]}{(\lambda + 2\mu)(3\lambda + 2\mu)}, \tag{3.67}$$

$$A_{ct} = \frac{\sigma\left[m + \lambda(3\cos^2\theta + 1) + \mu(2\cos^2\theta + 1) + \frac{\lambda n}{4\mu} \right]}{2\mu(3\lambda + 2\mu)}. \tag{3.68}$$

Note that the *A*'s in Eqs. (3.67) and (3.68) are not exactly the same as the *K*'s of this thesis. Recall that the acoustoelastic constants developed herein for L, SV and SH waves were all of the form of Eq. (3.54), $\Delta c/c^0 = \sigma\left[K_1 \sin^2\theta + K_2 \cos^2\theta \right] = \sigma K(\theta)$. Rearranging Eqs. (3.67) and (3.68) to match this form results in,

$$A_{cl} = \sigma\left[\begin{array}{l} \dfrac{\sin^2\theta\left(-2\lambda(\lambda+2\mu) - \mu(\lambda+2\mu) + 2\mu l - 2\lambda m\right)}{2\mu(\lambda+2\mu)(3\lambda+2\mu)} \\ + \dfrac{\cos^2\theta\left(4\lambda^2 + 14\lambda\mu + 8\mu^2 + 2\mu l + 4(\lambda+\mu)m\right)}{2\mu(\lambda+2\mu)(3\lambda+2\mu)} \end{array} \right], \tag{3.69}$$

$$A_{ct} = \sigma\left[\frac{\sin^2\theta\left(\mu(\lambda+\mu) + \mu m + \lambda n/4\right)}{2\mu^2(3\lambda+2\mu)} + \frac{\cos^2\theta\left(\mu(4\lambda+3\mu) + \mu m + \lambda n/4\right)}{2\mu^2(3\lambda+2\mu)} \right]. \tag{3.70}$$

These expressions have some similarities to those of Table 3.1, but definitely do not match. It is interesting to note that they are close to the L and SV constants if K_1 and K_2 are switched, and in fact the terms that include the third order elastic constants are identical. Graphical comparisons of the acoustoelastic constants over the range of

refracted angles for both L and S wave propagation are shown in Figures 3.3 and 3.4. Values of all elastic constants are from Stobbe [44].

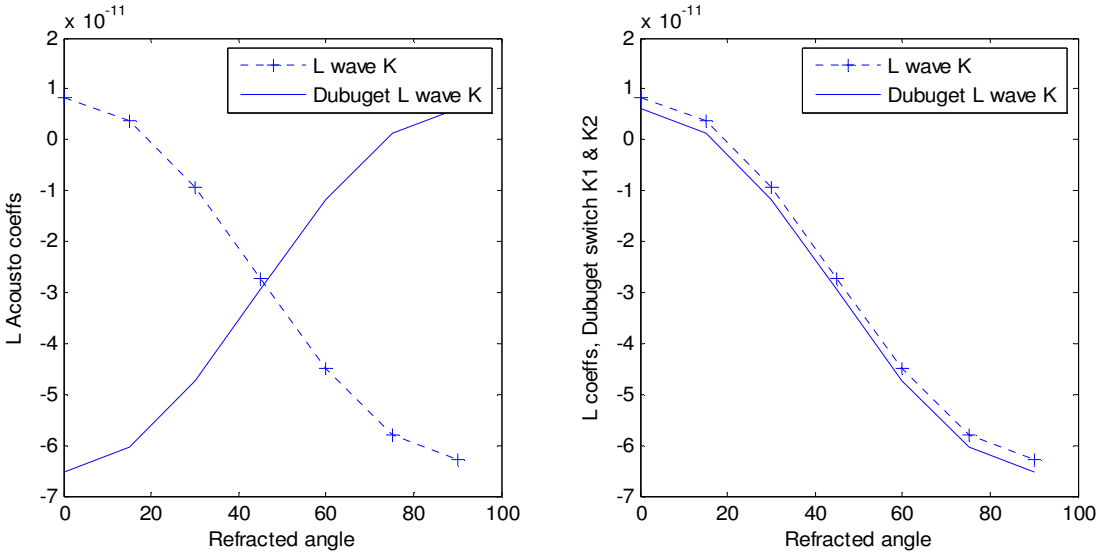

Figure 3.3. Comparison of current L wave acoustoelastic constants with those of Dubuget et al. [55]. (a) Direct comparison. (b) Comparison after switching K_1 and K_2 in Dubuget's formulae.

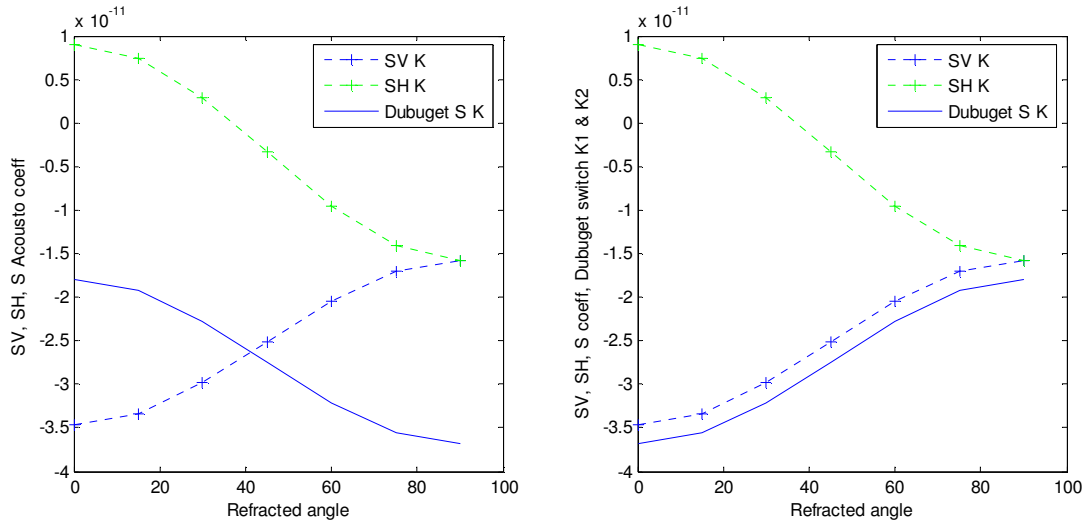

Figure 3.4. Comparison of current SV and SH wave acoustoelastic constants with the S wave constants of Dubuget et al. [55]. (a) Direct comparison. (b) Comparison after switching K_1 and K_2 in Dubuget's formulae.

The plots of the L wave and SV wave sets of constants show some agreement when K_1 and K_2 are switched, meaning that the angle θ is complemented. Algebraically the constants of Dubuget do not reduce to those of the parallel and perpendicular theory developed by Hughes and Kelly, which means that there is a question concerning the accuracy of their recovered TOECs.

3.4 Forward Problem: Computation of Measured Time Shifts

The forward problem consists of calculating time shifts for a given load using known TOECs and other properties of the material. The forward problem must be solved before the inverse problem of determining the TOECs from the time shifts can be addressed. In this section the time shifts for both the attached and floating transducers are examined. In the attached case the transducer separation distance increases with load, whereas for the floating case the distance remains constant.

3.4.1 Time Shift for Attached Transducer Configuration

Referring to Figure 3.1, the original path length P_0 in the natural (unstrained) state is,

$$P_0 = 2N_V \sqrt{\left(D_0/N_V\right)^2 + h_0^{\,2}}\,, \tag{3.71}$$

where N_V is the number of V paths (skips), D_0 is the original (half) transducer separation, and h_0 is the original thickness. Note that $N_V = 1$ in Figure 3.1. The original time of flight in the undeformed state is $TOF_0 = P_0/c_0$, where c_0 is the wave speed of interest (L, SV or SH). After deformation, the new separation distance becomes $D = D_0 + \Delta D = D_0\left(1+e\right)$, and the sample thickness becomes $h = h_0 + \Delta h = h_0\left(1-\nu e\right)$ as the

transducers move apart and the sample thickness decreases. Here ν is Poisson's ratio, the uniaxial strain is $e=\sigma/E$, and E is Young's modulus. The new path length is

$$P=2N_V\sqrt{\left(D/N_V\right)^2+h^2}\ . \tag{3.72}$$

The new time of flight is $TOF=P/c$, where the new velocity is $c=c_o+K(\theta)\sigma$. The total time shift ΔTOF due to both acoustoelasticity and geometry changes is,

$$\Delta TOF=TOF-TOF_0=\frac{2N_V\sqrt{\left[D_0(1+e)/N_V\right]^2+\left[h_0(1-\nu e)\right]^2}}{c_0+K(\theta)\sigma c_0}-\frac{P_0}{c_0}. \tag{3.73}$$

This equation is valid for all three wave modes (L, SV and SH) and for acoustoelastic constants in the initial state.

The same analysis can be performed in the natural (unstrained) state. Since the transducers are attached to the specimen, the path length in natural coordinates does not change. Thus, the only contribution to the time shift is the change in wave velocity. The time shift is computed as,

$$\Delta TOF=\frac{P_0}{c_0+\tilde{K}(\theta)\sigma c_0}-\frac{P_0}{c_0}. \tag{3.74}$$

Note that the acoustoelastic constant used here is that for wave speed changes in the natural system. Although this equation looks very different from Eq. (3.73), the computed time shifts are virtually identical.

3.4.2 Time Shift for Floating Transducer Configuration

Figure 3.1 also applies to the angle-beam floating configuration, but the transducer separation is now constant because the two transducers are held together as an

assembly and are liquid coupled to the specimen. Thus, as the load increases, the separation distance remains the same and the sample thickness decreases.

As for the attached case, time shifts can be calculated in either the natural system or the initial system. In the initial system, the time shift is,

$$\Delta TOF = \frac{2N_V\sqrt{\left[D_0/N_V\right]^2+\left[h_0(1-\nu e)\right]^2}}{c_0+K(\theta)\sigma c_0}-\frac{P_0}{c_0}. \tag{3.75}$$

A comparison to Eq. (3.73) indicates that the time shift for the floating configuration will always be less than that for the attached configuration if all other parameters are the same since the path in the deformed state is smaller.

In the natural system, the transducer separation distance decreases as the load is applied, but the thickness remains constant. The refracted angle also changes slightly. Thus, the acoustoelastic constant has to be evaluated for the refracted angle corresponding to the position of the transducers in the natural system after the load is applied. The time shift is calculated as,

$$\Delta TOF = \frac{2N_V\sqrt{\left[D_0(1-e)/N_V\right]^2+h_0{}^2}}{c_0+\tilde{K}(\theta')\sigma c_0}-\frac{P_0}{c_0}. \tag{3.76}$$

where

$$\theta' = \tan^{-1}\left[D_0(1-e)/(N_V h_0)\right]. \tag{3.77}$$

Since this difference in angle is a very small factor, the comparison to Eq. (3.74) indicates that the time shift for the floating configuration will always be less than that for the attached configuration if all other parameters are the same. Although Eq. (3.76) looks very different from Eq. (3.75), the computed time shifts are virtually identical.

3.5 Section Summary

Theory has been developed for both attached and floating configurations for angle-beam acoustoelasticity measurements with all three bulk wave modes (L, SV and SH). It is shown that all acoustoelastic constants reduce to those reported in the literature for the parallel and perpendicular cases. An attempt was made to reconcile the angle beam results with those reported in the literature, but there are significant differences. It is believed that those reported here are correct because they reduce to known expressions for the parallel and perpendicular cases. The general forward problem entails using known TOECs and derived acoustoelastic constants to predict the time shift of the ultrasonic waves with load, and formulae are shown for all the attached and floating cases for all wave modes.

CHAPTER 4

INVERSE PROBLEM DEVELOPMENT

The general inverse problem considered here is to determine the TOECs of a parallel faced isotropic sample using measured time shift data from a one-sided angle-beam technique. A necessary condition is that at least three measurements are required to determine the three TOECs. In this chapter the inverse problem is numerically investigated to determine additional conditions that are necessary for recovering TOECs from time shift data, examine the sensitivity of the inversion to various input parameters, and analyze which configuration is expected to achieve the most accurate results.

4.1 Required Measurements

Possible sets of required measurements may be determined by examining the form of the acoustoelastic constants in Table 3.2 for the L, SV and SH bulk wave modes. There are several conditions that can readily be deduced:

1. The set has to include at least one L wave measurement since only the L wave acoustoelastic constants contain the *l* TOEC.
2. Since the L wave acoustoelastic constants do not contain *n,* at least one shear wave measurement is required (SV or SH).
3. SV measurements at different angles do not provide additional information since the dependence on *m* and *n* is the same in both acoustoelastic constants. (i.e. Equations (3.45) and (3.46) for K_1^{SV} and K_2^{SV}).

For three measurements, there are ten possible mode combinations as shown in Table 4.1. Each combination is referred to by the concatenation of the modes.

Table 4.1. Possible wave mode combinations for TOEC recovery and their abbreviations.

Configuration			Abbreviation	Comment
L	SV	SH		
3	0	0	3L	Not possible, no *n* information
2	1	0	2L+1SV	**Possible, L waves at different angles**
2	0	1	2L+1SH	**Possible, L waves at different angles**
1	2	0	1L+2SV	Not possible, can't separate *m* and *n*
1	1	1	1L+1SV+1SH	**Possible**
1	0	2	1L+2SH	**Possible, SH waves at different angles**
0	3	0	3SV	Not possible, no *l* information
0	2	1	2SV+1SH	Not possible, no *l* information
0	1	2	1SV+2SH	Not possible, no *l* information
0	0	3	3SH	Not possible, no *l* information

Based on the conditions summarized in the above table, six of the ten combinations are eliminated, leaving 2L+1SV, 2L+1SH, 1L+1SV+1SH, and 1L+2SH as possible measurement combinations that may be used. The experimental focus of the work has been mainly the 2L+1SV configuration, with some measurements made using the 1L+1SV+1SH and 2L+1SH configurations. If additional L, SV or SH measurements are available, then the solution can be posed as an optimization problem whereby the mean squared error (MSE) in the time shifts is minimized.

4.2 TOEC Recovery Inverse Problem

The specific goal of the inverse problem is to determine the three TOECs from time-of-flight and load measurements; i.e, measurement of the time shift ΔTOF for each angle beam configuration at a specified applied load of σ. Regardless of the configuration chosen, the approach to solving the inverse problem is to find the values of l, m and n that yield $\Delta TOFs$ that best match the experimental data.

4.2.1 Linearization of the Change in Time of Flight

The time of flight TOF is related to the distance traveled, or path length P, and the wave speed c by $TOF = P/c$. The first approach to solving the inverse problem is to linearize the change in time of flight ΔTOF with respect to changes in path length (geometry) and changes in velocity (acoustoelasticity).

$$\begin{aligned} \Delta TOF &= \Delta TOF_G + \Delta TOF_A \\ &\cong \frac{\partial TOF}{\partial P}\Delta P + \frac{\partial TOF}{\partial c}\Delta c \\ &\cong \frac{1}{c}\Delta P - \frac{P}{c^2}\Delta c \end{aligned} \tag{4.1}$$

In this equation ΔP and Δc are the changes in path length and wave speed, respectively, caused by the load. Recalling that $\Delta c = cK\sigma$ gives

$$\Delta TOF \cong \frac{1}{c}\Delta P - \frac{PK\sigma}{c}, \tag{4.2}$$

where K is the appropriate acoustoelastic constant.

The change in path length ΔP can be further decomposed into contributions from the transducer separation D and thickness h.

$$\Delta P = \frac{\partial P}{\partial D}\Delta D + \frac{\partial P}{\partial h}\Delta h. \tag{4.3}$$

The derivatives can readily be computed from the expression for path length P. Referring to Figure 3.1, P can be expressed as,

$$P = 2N_V\sqrt{\left(\frac{D}{N_V}\right)^2 + h^2}, \tag{4.4}$$

where N_V is the number of V paths, or skips (only one V path is shown in the figure). Taking derivatives with respect to D and h gives,

$$\frac{\partial P}{\partial D} = \frac{2D}{N_V \sqrt{\left(\frac{D}{N_V}\right)^2 + h^2}} = \frac{4D}{P} \tag{4.5}$$

and

$$\frac{\partial P}{\partial h} = \frac{2N_V h}{\sqrt{\left(\frac{D}{N_V}\right)^2 + h^2}} = \frac{4N_V^2 h}{P}. \tag{4.6}$$

The final linearized expression for ΔTOF is,

$$\Delta TOF \cong \frac{4D}{cP}\Delta D + \frac{4N_V^2 h}{cP}\Delta h - \frac{PK\sigma}{c}. \tag{4.7}$$

Note that the first two terms are due to geometry changes and the third term is due to acoustoelasticity.

4.2.2 Attached Transducers

As the load increases, the thickness reduces and the transducers move further apart. Hence, in the initial (pre-stressed) coordinate system, the change in distance is $\Delta D = \varepsilon D$ and the change in thickness is $\Delta h = -\nu\varepsilon h$ where ε is the strain in the direction of loading. The strain is related to the stress by Young's modulus, E; $\varepsilon = \sigma/E$. In Equation (4.7), the time shift due to geometry now becomes,

$$\begin{aligned} \Delta TOF_G &= \frac{4D^2\varepsilon - 4N_V^2 h^2 \nu\varepsilon}{cP} \\ &= 4\left(\frac{D^2 - N_V^2 h^2 \nu}{cP}\right)\frac{\sigma}{E} \end{aligned}. \tag{4.8}$$

The velocity change due to acoustoelasticity is simply $cK(\theta)\sigma$, where $K(\theta)$ is the appropriate acoustoelastic constant for a refracted angle of θ and σ is the applied stress. The total time shift is,

$$\Delta TOF = \left[\frac{4(D^2 - h^2 N_V^2 \nu)}{c\,P}\right]\frac{\sigma}{E} - \left[\frac{K(\theta)\,P}{c}\right]\sigma . \tag{4.9}$$

Note that both terms are linear with respect to the applied load.

The geometry term is caused by deformation in the thickness and length directions, and is a function of only second order elastic constants (ν and E), the nominal wavespeed, and the applied stress. The part of the time shift due to acoustoelasticity is proportional to the acoustoelastic constant. Referring to Table 3.2, it can be seen that all of the acoustoelastic constants are linear in the TOECs l, m and n. Thus, the time shift due to acoustoelasticity can generally be expressed as,

$$\Delta TOF_A = -\frac{P}{c}\sigma\,K(\theta) = a_0 + a_1 l + a_2 m + a_3 n . \tag{4.10}$$

Expressions for the constants a_i can be obtained for propagation of L, SV and SH waves using the formulae for the various acoustoelastic constants in the initial system given in Table 3.2. These expressions are summarized in Table 4.2.

The three expressions for the particular measurement configuration being considered (e.g., 2L+1SV) can be then combined and rearranged to yield a set of three linear equations:

$$\begin{bmatrix} a_1^{SV} & a_2^{SV} & a_3^{SV} \\ a_1^{L1} & a_2^{L1} & a_3^{L1} \\ a_1^{L2} & a_2^{L2} & a_3^{L2} \end{bmatrix}\begin{bmatrix} l \\ m \\ n \end{bmatrix} = \begin{bmatrix} \Delta TOF_{meas}^{SV} - \Delta TOF_G^{SV} - a_0^{SV} \\ \Delta TOF_{meas}^{L1} - \Delta TOF_G^{L1} - a_0^{L1} \\ \Delta TOF_{meas}^{L2} - \Delta TOF_G^{L2} - a_0^{L2} \end{bmatrix}. \tag{4.11}$$

Note that the L1 and L2 coefficients are computed using the same formulae but with different refracted angles. Similar systems of equations can be written for the other three valid configurations (i.e., 2L+1SH, 1L+1SV+1SH and 1L+2SH). This linear system of equations can then be solved for the three TOECs l, m and n.

Table 4.2. Coefficients for expressing the time shift due to acoustoelasticity as a linear combination of TOECs ($\Delta TOF_A = a_0 + a_1 l + a_2 m + a_3 n$).

L-Wave Propagation	
a_0^L	$\frac{-P\sigma}{c_L}\left[\frac{(4\lambda^2+15\lambda\mu+10\mu^2)\sin^2\theta-2\lambda(\lambda+2\mu)\cos^2\theta}{2\mu(3\lambda+2\mu)(\lambda+2\mu)}\right]$
a_1^L	$\frac{-P\sigma}{c_L}\left[\frac{1}{(3\lambda+2\mu)(\lambda+2\mu)}\right]$
a_2^L	$\frac{-P\sigma}{c_L}\left[\frac{4(\lambda+\mu)\sin^2\theta-2\lambda\cos^2\theta}{2\mu(3\lambda+2\mu)(\lambda+2\mu)}\right]$
a_3^L	0
SV-Wave Propagation	
a_0^{SV}	$\frac{-P\sigma}{c_{SV}}\left[\frac{4(\lambda+\mu)\sin^2\theta+(\lambda+2\mu)\cos^2\theta}{2\mu(3\lambda+2\mu)}\right]$
a_1^{SV}	0
a_2^{SV}	$\frac{-P\sigma}{c_{SV}}\left[\frac{1}{2\mu(3\lambda+2\mu)}\right]$
a_3^{SV}	$\frac{-P\sigma}{c_{SV}}\left[\frac{\lambda}{8\mu^2(3\lambda+2\mu)}\right]$
SH-Wave Propagation	
a_0^{SH}	$\frac{-P\sigma}{c_{SH}}\left[\frac{4(\lambda+\mu)\sin^2\theta-2\lambda\cos^2\theta}{2\mu(3\lambda+2\mu)}\right]$
a_1^{SH}	0
a_2^{SH}	$\frac{-P\sigma}{c_{SH}}\left[\frac{1}{2\mu(3\lambda+2\mu)}\right]$
a_3^{SH}	$\frac{-P\sigma}{c_{SH}}\left[\frac{\lambda\sin^2\theta-2(\lambda+\mu)\cos^2\theta}{8\mu^2(3\lambda+2\mu)}\right]$

4.2.3 Floating Transducers

The analysis just performed for the attached transducers can be applied to the floating transducers with a few minor modifications. Since the transducers are floating with respect to the specimen surface, the separation distance D does not change with load. Thus, the expression for ΔTOF in Eq. (4.9) becomes,

$$\Delta TOF = -\left[\frac{4h^2 N_V^2 \nu}{cP}\right]\frac{\sigma}{E} - \left[\frac{K(\theta)P}{c}\right]\sigma \tag{4.12}$$

The first term is the time shift due to geometry, and it is always negative because the path length under load is always shorter than the no-load path. The second term, the time shift due to acoustoelasticity, is the same as for the attached case. Systems of equations similar to those of Eq. (4.11) can be constructed for the four measurement configurations to recover the TOECs.

4.2.4 Normal Incidence Case

The normal incidence case; i.e., refracted angle of 0, was previously considered by Stobbe [44] for the recovery of TOECs for aluminum 7075. Measurements were made with one longitudinal, one shear vertical and one shear horizontal wave in both through transmission and pulse echo configurations. The theory behind these experiments is reviewed here since the normal incidence case is a subset of either the floating or the attached angle-beam case for the 1L+1SV+1SH configuration. Note that the SV configuration corresponds to particle motion in the direction of loading, and the SH to particle motion normal to the direction of loading.

For pulse-echo normal incidence, the path length P is equal to the thickness h, and Eq. (4.4) applies with $\theta = 0$, N_V = 0.5, and D = 0. The various time shifts due to

acoustoelasticity for the three wave modes can be expressed as per Eq. (4.10) using the appropriate formulae from Table 4.2. For the L wave,

$$\begin{aligned}\Delta TOF_A^L = &\frac{-P\sigma}{c_L}\left[\frac{-2\lambda(\lambda+2\mu)}{2\mu(3\lambda+2\mu)(\lambda+2\mu)}\right] \\ &-\frac{P\sigma}{c_L}\left[\frac{1}{(3\lambda+2\mu)(\lambda+2\mu)}\right]l-\frac{P\sigma}{c_L}\left[\frac{-2\lambda}{2\mu(3\lambda+2\mu)(\lambda+2\mu)}\right]m \\ &=-\frac{P\sigma}{c_L}\left[\frac{-2\lambda(\lambda+2\mu)}{2\mu(3\lambda+2\mu)(\lambda+2\mu)}\right]-\frac{P\sigma}{c_L}\left[\frac{2\mu l-2\lambda m}{2\mu(3\lambda+2\mu)(\lambda+2\mu)}\right].\end{aligned} \tag{4.13}$$

Rearranging and grouping terms yields,

$$-2\mu l+2\lambda m=\frac{c_L}{P\sigma}\left[2\mu(3\lambda+2\mu)(\lambda+2\mu)\right]\Delta TOF_A^L-2\lambda(\lambda+2\mu). \tag{4.14}$$

A similar expression can be obtained for the SV configuration,

$$\mu m+\lambda n/4=\frac{c_{SV}}{P\sigma}\left[2\mu^2(3\lambda+2\mu)\right]\Delta TOF_A^{SV}+\mu(\lambda+2\mu), \tag{4.15}$$

and the SH configuration,

$$-\mu m-(\lambda+\mu)n/2=\frac{c_{SH}}{P\sigma}\left[2\mu^2(3\lambda+2\mu)\right]\Delta TOF_A^{SH}-2\lambda\mu. \tag{4.16}$$

These equations can be expressed in matrix form,

$$\begin{bmatrix}-2\mu & 2\lambda & 0\\ 0 & \mu & \frac{\lambda}{4}\\ 0 & \mu & -(\lambda+\mu)/2\end{bmatrix}\begin{bmatrix}l\\ m\\ n\end{bmatrix}=\begin{bmatrix}R_L\\ R_{SV}\\ R_{SH}\end{bmatrix}, \tag{4.17}$$

where the constants R_L, R_{SV} and R_{SH} are defined as follows:

$$\begin{aligned}R_L&=\frac{c_L}{P\sigma}\left[2\mu(3\lambda+2\mu)(\lambda+2\mu)\right]\Delta TOF_A^L-2\lambda(\lambda+2\mu),\\ R_{SV}&=\frac{c_{SV}}{P\sigma}\left[2\mu^2(3\lambda+2\mu)\right]\Delta TOF_A^{SV}+\mu(\lambda+2\mu),\\ R_{SH}&=\frac{c_{SH}}{P\sigma}\left[2\mu^2(3\lambda+2\mu)\right]\Delta TOF_A^{SH}-2\lambda\mu.\end{aligned} \tag{4.18}$$

The time shifts due to acoustoelasticity are the measured time shifts, ΔTOF_{meas}, minus the computed time shifts due to geometry, ΔTOF_G,

$$\Delta TOF_A = \Delta TOF_{meas} - \Delta TOF_G = \Delta TOF_{meas} - \left[\frac{h\nu}{c}\right]\frac{\sigma}{E}, \tag{4.19}$$

where c is the appropriate wavespeed (L, SV or SH).

4.3 Example Forward and Inverse Calculations

This section shows sample calculations for configurations typical of experiments performed. The purpose of this numerical study is to illustrate recovery of elastic constants for all eight valid configurations (four mode combinations, attached and floating transducers). Table 4.3 summarizes the nominal parameters considered for various attached and floating transducers using a single V-path (skip) configuration. The material is 7075 aluminum and the TOECs are from Stobbe [44].

Table 4.3. Input parameters for TOEC recovery examples

Parameter		**Nominal Value**	**Variable Name**	**Parameter**		**Nominal Value**	**Variable Name**
1.	TOEC #1	-252.2×10^9 Pa	l	**9.**	45SH Trans Sep	6.26mm	D_{SH1}
2.	TOEC #2	-324.9×10^9 Pa	m	**10.**	70SH Trans Sep	17.209mm	D_{SH2}
3.	TOEC #3	-351.2×10^9 Pa	n	**11.**	Lambda	54.9 GPa	λ
4.	Sample Thickness	6.26 mm	h	**12.**	Mu	26.5 GPa	μ
5.	Sample Width	76.29 mm	w	**13.**	Density	2800 kg/m^3	ρ
6.	45L Trans Sep	6.26 mm	D_{L1}	**14.**	Force	94,298 N	F
7.	60L Trans Sep	10.85 mm	D_{L2}	**15.**	# V-Paths	1	N_V
8.	45SV Trans Sep	6.26 mm	D_{SV}				

The various ΔTOFs are first calculated for the two L, one SV and two SH configurations shown in Table 4.3 for both the attached and floating transducer cases. Furthermore, the ΔTOFs can be either calculated exactly using Eqs. (3.73) and (3.75), or

approximately using the linearized formulae of Eqs. (4.9) and (4.12). These results are summarized in Table 4.4. Young's modulus, E, and Poisson's ratio, ν, are calculated from the Lamé constants λ and μ using $E = \mu(3\lambda + 2\mu)/(\lambda + \mu)$ and $\nu = \lambda/[2(\lambda + \mu)]$.

Table 4.4. Calculated time shifts for numerical examples

Configuration	Calculated Δ*TOF*s (ns)			
	Attached		Floating	
	Exact	Approximate	Exact	Approximate
L1, $\theta_{nom} = 45°$	18.07	17.97	14.09	13.99
L2, $\theta_{nom} = 60°$	43.76	43.37	35.32	34.94
SV, $\theta_{nom} = 45°$	34.07	33.89	26.03	25.87
SH1, $\theta_{nom} = 45°$	9.11	9.09	1.08	1.07
SH2, $\theta_{nom} = 70°$	58.23	58.07	28.94	28.79

As expected, the time shifts for the floating transducers are always less than those for the attached transducer since the path length becomes shorter with load. The 60º longitudinal case has both the maximum time shifts and the maximum errors in time shifts caused by using the linear approximation, but the errors are still quite small (less than 0.5 ns).

The TOECs *l, m* and *n* can now be computed from the five sets of Δ*TOF*s given in Table 4.4 using various angle beam combinations. Tables 4.5, 4.6, 4.7 and 4.8 summarize the results for the 2L+1SV, 2L+1SH, 1L+2SH and 1L+1SV+1SH configurations, respectively. For the 1L+1SV+1SH configuration, the L-wave angle of 60º is used.

Table 4.5. Recovered TOECs for the 2L+1SV configuration with L1=45º, L2=60 º and SV=45 º.

Constant	Calculated TOECs for 2L+1SV Configuration (GPa)			
	Attached		Floating	
	(Exact Δ*TOF*s)	(Approx. Δ*TOF*s)	(Exact Δ*TOF*s)	(Approx. Δ*TOF*s)
l	-249.2	-252.2	-248.7	-252.2
m	-328.6	-324.9	-328.6	-324.9
n	-347.8	-351.2	-347.3	-351.2

Table 4.6. Recovered TOECs for the 2L+1SH configuration with L1=45º, L2=60 º and SH=70 º.

Constant	Calculated TOECs for 2L + 1SH Configuration (GPa)			
	Attached		Floating	
	(Approx. Δ*TOF*s)	(Exact Δ*TOF*s)	(Approx. Δ*TOF*s)	(Exact Δ*TOF*s)
l	-249.2	-252.2	-248.7	-252.2
m	-328.6	-324.9	-328.6	-324.9
n	-357.9	-351.2	-358.1	-351.2

Table 4.7. Recovered TOECs for the 1L+1SV+1SH configuration with L=60º, SV=45 º and SH=70 º.

Constant	Calculated TOECs for 1L + 1SV + 1SH Configuration (GPa)			
	Attached		Floating	
	(Approx. Δ*TOF*s)	(Exact Δ*TOF*s)	(Approx. Δ*TOF*s)	(Exact Δ*TOF*s)
l	-265.7	-252.2	-264.6	-252.2
m	-324.5	-324.9	-324.7	-324.9
n	-355.6	-351.2	-354.8	-351.2

Table 4.8. Recovered TOECs for the 1L+2SH configuration with L=60º, SH1=45 º and SH2=70 º.

Constant	Calculated TOECs for 1L + 2SH Configuration (GPa)			
	Attached		Floating	
	(Approx. Δ*TOF*s)	(Exact Δ*TOF*s)	(Approx. Δ*TOF*s)	(Exact Δ*TOF*s)
l	-261.6	-252.2	-261.4	-252.2
m	-325.5	-324.9	-325.5	-324.9
n	-351.9	-351.2	-352.0	-351.2

The correct TOECs are exactly recovered for both the attached and floating transducers when the approximate Δ*TOF*s are used, but they are not when the exact Δ*TOF*s are used. The reason is that the inversion procedure is based upon the linearized approximate equations for the Δ*TOF*s, and thus the exact TOECs are recovered only when the time shifts match those calculated by the approximations. The error in the recovered TOECs when using the exact Δ*TOF*s is due to the linearization and is generally quite small, particularly for *m* and *n*. The largest errors are for *l*, and they are less than 5%. Linearization errors are thus neglected from this point forward.

4.4 Sensitivity Analysis

In developing the method for TOEC recovery it is desirable to quantify the uncertainty in the measurement process. The primary goal is to answer the question, "How accurately are TOECs being estimated?" A comprehensive sensitivity analysis has to be performed for each measurement configuration developed. A measurement configuration refers to the combination of modes, transducer spacings and V-paths considered for a particular specimen thickness and transducer mounting. The analysis accounts for small errors in the transducer spacing, specimen thickness, elastic constants, applied force and density as well as errors in the measured time shifts, and quantifies their effects on the recovered TOECs. These numerical experiments can determine which measurement configuration shows the least sensitivity to the various errors; e.g. 2L+1SV vs. 1L+2SH, and can lead to better recovery methods.

The TOEC measurement accuracy and uncertainty is also compared to those of existing ultrasonic methods for determining TOECs where the direction of propagation is either parallel or directly perpendicular to the loading direction. Generally the TOECs can be expressed in the following way,

$$TOEC = f\left(\Delta TOFs, \lambda, \mu, D, h, w, \rho, F\right). \tag{4.20}$$

Equation (4.20) relates a TOEC to specific variables. The overall uncertainty in the TOEC depends on the uncertainty of each variable. The overall uncertainty is determined by the square root of the sum of the squares of the individual uncertainties as shown below for the l TOEC, where U_l is the overall uncertainty in l.

$$
\begin{aligned}
l &= f_l\left(\Delta TOFs, \lambda, \mu, D, h, w, \rho, F\right) \\
\Delta l &= \frac{\partial f_l}{\partial TOF_1}\Delta TOF_1 \cdots + \frac{\partial f_l}{\partial \lambda}\Delta\lambda + \frac{\partial f_l}{\partial \mu}\Delta\mu + \cdots \\
U_l &= \sqrt{\left(\frac{\partial f_l}{\partial TOF}\Delta TOF\right)^2 + \cdots \left(\frac{\partial f_l}{\partial \lambda}\Delta\lambda\right)^2 + \cdots}
\end{aligned}
\tag{4.21}
$$

Uncertainties of the individual variables were determined by a combination of means including looking at ranges of values in the literature values (e.g., for elastic constants and density) and estimating the scatter from repeated measurements (e.g., times-of-flight and specimen dimensions).

Since there are no closed form expressions for calculating *l*, *m* and *n*, a numerical approach is taken for evaluating the individual uncertainty terms. For example, the uncertainty due to λ is estimated as,

$$
\frac{\partial f_l}{\partial \lambda}\Delta\lambda \cong f_l\big|_{\lambda_0+\Delta\lambda} - f_l\big|_{\lambda_0}, \tag{4.22}
$$

where $\Delta\lambda$ is the estimated uncertainty in λ.

4.5 Best Configuration for TOEC Recovery

The best configuration for recovery of TOECs is that which results in the lowest uncertainty while still being experimentally feasible. In this section the uncertainties of the individual input parameters are first estimated. Next, an example calculation is presented in which the uncertainties in *l*, *m* and *n* are calculated. Then a comparison of uncertainties is given for all possible attached and floating configurations using a limited set of common refracted angle wedges. Finally, an exhaustive search is made of a wide range of feasible refracted angles.

4.5.1 Estimated Uncertainties of Input Variables

Nominal uncertainties of all input variables for the TOEC recovery sensitivity analysis are shown in Table 4.9, and apply to both the floating and attached cases. Note that these values are generally conservative and it may be possible to achieve lower uncertainties for some of these variables. The nominal values of all input variables, with the exception of the ΔTOFs, are given in Table 4.3.

Table 4.9. Estimated uncertainties for all input parameters.

Variable	Uncertainty
ΔTOF (all)	1 ns
h	0.08 mm
w	0.08 mm
D (all)	0.5 mm
λ	2 GPa
μ	0.3 GPa
ρ	30 Kg/m^3
F	500 N

4.5.2 Example Uncertainty Calculations

An example uncertainty calculation is presented here for the 2L+1SV attached transducer configuration with nominal refracted angles and other parameters as given in Table 4.3. The time shifts are calculated as per the approximate linearized equations. There are a total of 12 input variables – the three ΔTOFs, the specimen width and thickness, three transducer separation distances, two elastic constants, the density, and the applied load. Note that the applied stress is calculated from the applied load and the specimen cross sectional area. Figure 4.1 shows the uncertainties in l, m and n due to the uncertainties in all 12 variables. The 13th bar is the total uncertainty calculated as per Eq. (4.21).

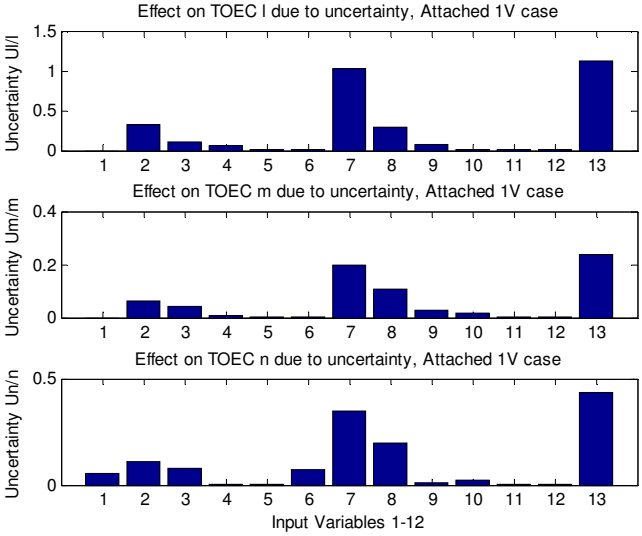

No.	*Variable*
1	ΔTOF_{SV}
2	ΔTOF_{L1}
3	ΔTOF_{L2}
4	h
5	w
6	D_{SV}
7	D_{L1}
8	D_{L2}
9	λ
10	μ
11	ρ
12	F
13	*Total*

Figure 4.1. Uncertainties in recovered TOECs caused by uncertainties in all input variables for the attached 2L+1SV configuration with a single V path.

It can be seen that the uncertainty for l is the biggest and that for m is the smallest. The largest contributor to uncertainty is the transducer separation distance for the 45º L-wave transducer pair, followed by the measured time shift for this same pair.

4.5.3 Common Refracted Angle Search

An approach is considered using refracted angle wedges that are commonly available. The choice of wedge angles was made based on the availability and common industry usage, and consists of 45S, 70S, 35L, 45L, 60L and 70L. These angles lead to 12 combinations for the 2L+1SV configuration, and 14 combinations for the 1L+1SV+1SH configuration. Table 4.10 shows the resulting overall uncertainties for the 2L+1SV attached configuration, and Table 4.11 for the floating transducers. Results are expressed as, for example, U_l/l , which is the total uncertainty in l divided by the nominal value of l. The lowest average uncertainty for both configurations is obtained when SV=70º, L1=35º and L2=70º (case 9), and the second best is when SV=45º, L1=35º and L2=70º (case 3), indicating that the L angles must be far apart.

Table 4.10. Uncertainties for the 2L+1SV configuration with attached transducers.

	Angles			**Relative Uncertainties**			
Case	**L1**	**L2**	**SV**	U_l / l	U_m / m	U_n / n	**Average**
1	35º	45º	45º	1.0185	0.4399	0.7897	0.7494
2	35	60	45	0.6790	0.1496	0.2779	0.3688
3	35	70	45	0.6352	0.1060	0.2043	0.3152
4	45	60	45	1.1288	0.2389	0.4337	0.6005
5	45	70	45	0.8633	0.1411	0.2636	0.4227
6	70	60	45	1.9343	0.3051	0.5507	0.9300
7	35	45	70	1.0185	0.4399	0.7861	0.7482
8	35	60	70	0.6790	0.1496	0.2678	0.3655
9	**35**	**70**	**70**	**0.6352**	**0.1060**	**0.1903**	**0.3105**
10	45	60	70	1.1288	0.2389	0.4273	0.5983
11	45	70	70	0.8633	0.1411	0.2531	0.4192
12	60	70	70	1.9343	0.3051	0.5457	0.9280
Average				1.0432	0.2300	0.4159	

Table 4.11. Uncertainties for the 2L+1SV configuration with floating transducers.

	Angles			Relative Uncertainties			
Case	**L1**	**L2**	**SV**	U_l / l	U_m / m	U_n / n	**Average**
1	35º	45º	45º	0.8594	0.3728	0.6670	0.6331
2	35	60	45	0.5776	0.1275	0.2306	0.3119
3	35	70	45	0.5411	0.0908	0.1660	0.2660
4	45	60	45	0.9536	0.2023	0.3632	0.5064
5	45	70	45	0.7310	0.1199	0.2172	0.3560
6	70	60	45	1.6308	0.2576	0.4616	0.7833
7	35	45	70	0.8594	0.3728	0.6650	0.6324
8	35	60	70	0.5776	0.1275	0.2249	0.3100
9	**35**	**70**	**70**	**0.5411**	**0.0908**	**0.1571**	**0.2633**
10	45	60	70	0.9536	0.2023	0.3596	0.5052
11	45	70	70	0.7310	0.1199	0.2113	0.3541
12	60	70	70	1.6308	0.2576	0.4589	0.7824
Average				0.8823	0.1952	0.3486	

The 1L+1SV+1SH solution is examined in a similar manner for comparison purposes with results summarized in Tables 4.12 and 4.13. The range of uncertainty is similar to the 2L+1SV results; i.e. 0.62 for the attached transducers and 0.52 for the floating. The best-case floating pair for the 2L+1SV configuration gives a slightly lower uncertainty of 0.2633 vs. 0.3105. For the 1L+1SV+1SH configuration the floating case also gives a lower uncertainty of 0.1279 vs. 0.1727.

Table 4.12. Uncertainties for the 1L+1SV+1SH configuration with attached transducers.

	Angles			Relative Uncertainties			
Case	**L**	**SV**	**SH**	U_l / l	U_m / m	U_n / n	**Average**
1	35	45	45	0.5183	0.0566	0.0911	0.2220
2	35	45	70	0.5221	0.1039	0.2456	0.2905
3	35	70	45	0.5279	0.0532	0.0828	0.2180
4	35	70	70	0.5210	0.0907	0.1833	0.2650
5	45	45	45	0.4953	0.0566	0.0911	0.2143
6	45	45	70	0.5410	0.1039	0.2456	0.2968
7	45	70	45	0.4916	0.0532	0.0828	0.2092
8	45	70	70	0.5256	0.0907	0.1833	0.2665
9	60	45	45	0.4320	0.0566	0.0911	0.1932
10	60	45	70	0.6208	0.1039	0.2456	0.3234
11	60	70	45	0.4168	0.0532	0.0828	0.1843
12	60	70	70	0.5652	0.0907	0.1833	0.2797
13	70	45	45	0.4075	0.0566	0.0911	0.1851
14	70	45	70	0.6992	0.1039	0.2456	0.3496
15	**70**	**70**	**45**	**0.3822**	**0.0532**	**0.0828**	**0.1727**
16	70	70	70	0.6176	0.0907	0.1833	0.2972
Average				0.5171	0.0761	0.1507	

Table 4.13. Uncertainties for the 1L+1SV+1SH configuration with floating transducers.

	Angles			Relative Uncertainties			
Case	**L**	**SV**	**SH**	U_l / l	U_m / m	U_n / n	**Average**
1	35	45	45	0.4436	0.0404	0.0628	0.1823
2	35	45	70	0.4455	0.0681	0.1635	0.2257
3	35	70	45	0.4433	0.0376	0.0564	0.1791
4	35	70	70	0.4448	0.0603	0.1203	0.2085
5	45	45	45	0.4173	0.0404	0.0628	0.1735
6	45	45	70	0.4409	0.0681	0.1635	0.2242
7	45	70	45	0.4155	0.0376	0.0564	0.1698
8	45	70	70	0.4329	0.0603	0.1203	0.2045
9	60	45	45	0.3432	0.0404	0.0628	0.1488
10	60	45	70	0.4509	0.0681	0.1635	0.2275
11	60	70	45	0.3355	0.0376	0.0564	0.1432
12	60	70	70	0.4164	0.0603	0.1203	0.1990
13	70	45	45	0.3033	0.0404	0.0628	0.1355
14	70	45	70	0.4808	0.0681	0.1635	0.2375
15	**70**	**70**	**45**	**0.2897**	**0.0376**	**0.0564**	**0.1279**
16	70	70	70	0.4271	0.0603	0.1203	0.2026
Average				0.4082	0.0516	0.1008	

The l uncertainty is the largest for all solutions examined, and the 1L+1SV+1SH configuration offers significantly lower uncertainty values than the 2L+1SV configuration. The scatter is also lower for this solution. Specifically, Table 4.13 shows that for the floating 1L+1SV+1SH configuration almost any angle combination will yield similar results. In both solutions the attached cases have a larger scatter in the average uncertainty. Figures 4.2 and 4.3 show the output uncertainty breakdown for the 2L+1SV attached and floating configurations, respectively. Figures 4.4 and 4.5 show the same for the 1L+1SV+1SH configuration.

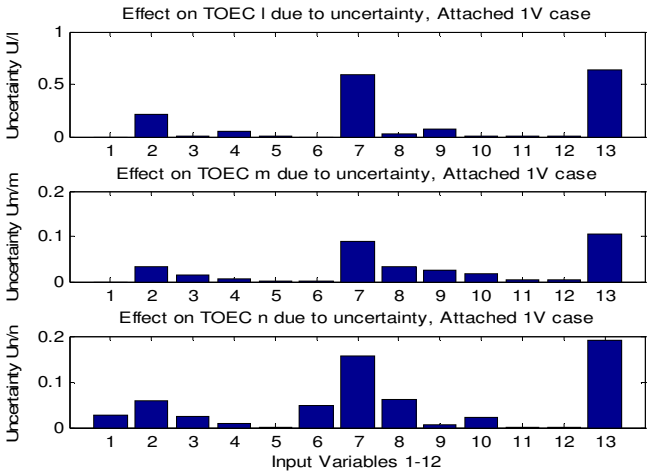

No.	*Variable*
1	ΔTOF_{SV}
2	ΔTOF_{L1}
3	ΔTOF_{L2}
4	h
5	w
6	D_{SV}
7	D_{L1}
8	D_{L2}
9	λ
10	μ
11	ρ
12	F
13	*Total*

Figure 4.2. Uncertainty breakdown for the best 2L+1SV attached transducer pair of Table 4.10 (case 9).

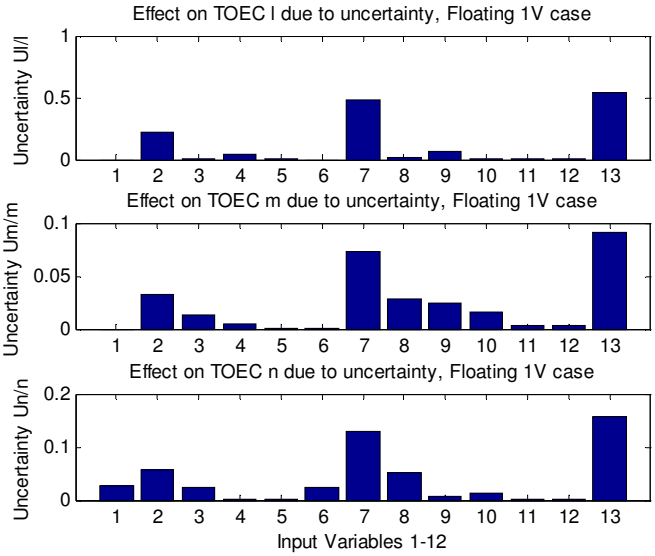

Figure 4.3. Uncertainty breakdown for the best 2L+1SV floating transducer pair of Table 4.11 (case 9).

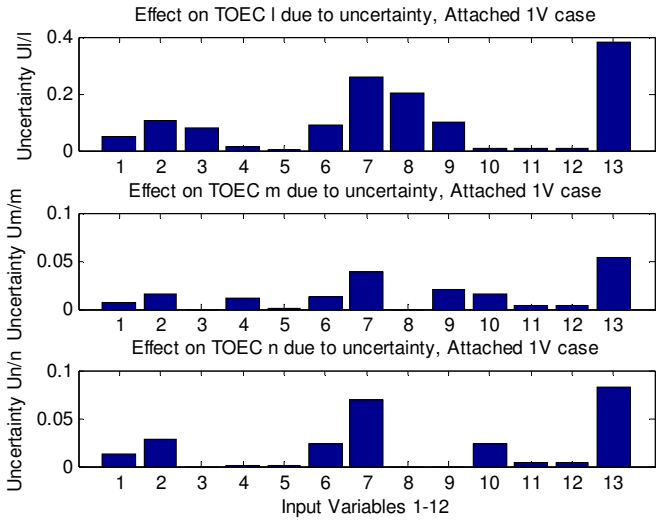

No.	*Variable*
1	ΔTOF_{SV}
2	ΔTOF_{SH}
3	ΔTOF_{Ll}
4	h
5	w
6	D_{SV}
7	D_{SH}
8	D_{Ll}
9	λ
10	μ
11	ρ
12	F
13	*Total*

Figure 4.4. Uncertainty breakdown for the best 1L+1SV+1SH attached transducer pair of Table 4.12 (case 15).

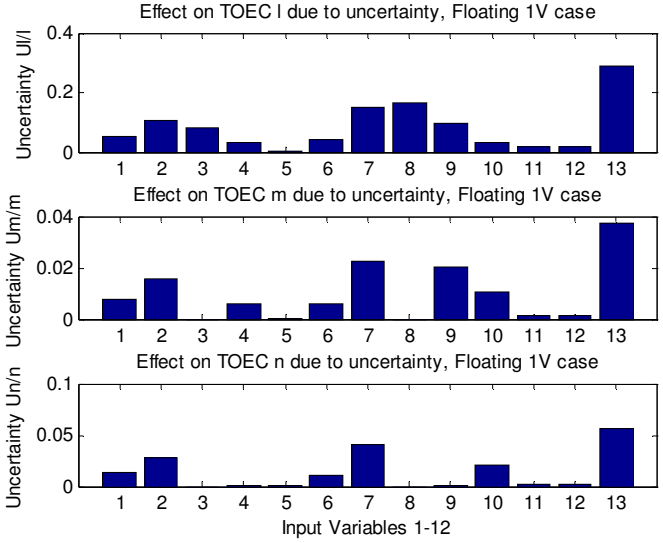

Figure 4.5. Uncertainty breakdown for the best 1L+1SV+1SH floating transducer pair of Table 4.13 (case 15).

Column 13 in Figures 4.2 through 4.5 represents the total uncertainty in each TOEC. Some preliminary observations for the 2L+1SV solution are listed below for both attached and floating transducers.

1. The SV ΔTOF (input variable #1) does not affect *l* or *m* as shown in the theory.

2. The *l* TOEC has the highest uncertainty

3. Generally the ΔTOF and separation distances are the major contributors to the overall uncertainty. Specifically the L1 (smaller refracted angle) ΔTOF and separation distance are major contributors to the *l* TOEC uncertainty

4. In both configurations *m* has the least uncertainty while *l* has the most even if separation distance errors are ignored.

Overall the common refracted angle approach highlights the need to consider a larger range of refracted angles to see if these preliminary observations hold throughout the entire solution space.

4.5.4 Exhaustive Refracted Angle Search

An exhaustive search process is carried out over a reasonable angle range for each configuration (2L+1SV, 2L+1SH, 1L+1SV+1SH and 1L+2SH; attached and floating transducers). The search consists of evaluating the overall uncertainties in recovering *l*, *m* and *n* for every angle combination while satisfying the restrictions; e.g. L1 ≠ L2 for 2L+1SV. The best solution is considered to be the one offering the lowest level of total uncertainty for the same input conditions. The results of the common refracted angle approach are a subset of this exhaustive approach. For all wave modes (L, SV and SH),

the angle range considered was 32 to 70 degrees. This range was selected because any angle in this range should be experimentally feasible both in terms of the geometry to generate the waves and the resulting signal amplitude. The variation of angles over the range leads to changes in both the separation distance and hence time shifts. The same nominal error values in Table 4.9 are used in this approach to establish uncertainty variations over the angle range.

The exhaustive search metholodogy is first presented for the 2L+1SV attached configuration, and is essentially the same for all the other seven configurations. The search and optimization procedure is as follows:

1. Create angle arrays in one degree steps for each transducer pair; e.g., 32,33,…69,70.

2. Implement a triple loop to iterate through all possible angle combinations while obeying the rules. (e.g., $L1 \neq L2$).

3. The results, which are in the form of 3D "cubes," one each for *l*, *m* and *n*, are analyzed to see which angle combinations yield the lowest uncertainties.

Table 4.14 summarizes the refracted angles for both the attached and floating 2L+1SV configurations that achieve the minimum uncertainties in *l*, *m* and *n*. The rows labeled "Selected" are those manually selected angles that provide the best compromise in uncertainty for all three TOECs. Tables 4.15, 4.16 and 4.17 present the same information for the other three configurations.

Table 4.14. Exhaustive search results for the 2L+1SV attached and floating configurations corresponding to the minimum uncertainties in *l*, *m* and *n*.

Coupling	L1	L2	SV	U_l / *l*	U_m / *m*	U_n / *n*	Comment
Attached	32°	70°	*50°	0.5823	0.0980	0.1892	Minimum U_l
Attached	32°	70°	*70°	0.5823	0.0980	0.1761	Minimum U_m
Attached	32°	70°	*32°	0.5823	0.0980	0.1927	Minimum U_n
Attached	**32°**	**70°**	**70°**	**0.5823**	**0.0980**	**0.1761**	**Selected**
Floating	32°	70°	*50°	0.4974	0.0842	0.1530	Minimum U_l
Floating	32°	70°	*70°	0.4974	0.0842	0.1461	Minimum U_m
Floating	32°	70°	*32°	0.4974	0.0842	0.1585	Minimum U_n
Floating	**32°**	**70°**	**32°**	**0.4974**	**0.0842**	**0.1461**	**Selected**

***** Almost no angular dependence

Table 4.15. Exhaustive search results for the 2L+1SH attached and floating configurations corresponding to the minimum uncertainties in *l*, *m* and *n*.

Coupling	L1	L2	SH	U_l / *l*	U_m / *m*	U_n / *n*	Comment
Attached	32°	70°	*50°	0.5823	0.0980	0.3524	Minimum U_l
Attached	32°	70°	*70°	0.5823	0.0980	0.3300	Minimum U_m
Attached	32°	70°	32°	0.5823	0.0980	0.1300	Minimum U_n
Attached	**32°**	**70°**	**32°**	**0.5823**	**0.0980**	**0.1300**	**Selected**
Floating	32°	70°	*50°	0.4974	0.0842	0.2709	Minimum U_l
Floating	32°	70°	*70°	0.4974	0.0842	0.2739	Minimum U_m
Floating	32°	70°	32°	0.4974	0.0842	0.1015	Minimum U_n
Floating	**32°**	**70°**	**32°**	**0.4974**	**0.0842**	**0.1015**	**Selected**

***** Almost no angular dependence

Table 4.16. Exhaustive search results for the 1L+1SV+1SH attached and floating configurations corresponding to the minimum uncertainties in *l*, *m* and *n*.

Coupling	L1	SV	SH	U_l / *l*	U_m / *m*	U_n / *n*	Comment
Attached	32°	70°	70°	0.5173	0.0907	0.1833	Minimum U_l
Attached	32°	*50°	*50°	0.5170	0.0576	0.1010	Minimum U_m
Attached	32°	*32°	*32°	0.5171	0.0546	0.0704	Minimum U_n
Attached	**32°**	**32°**	**32°**	**0.5171**	**0.0546**	**0.0704**	**Selected**
Floating	32°	32°	32°	0.4438	0.0417	0.0518	Minimum U_l
Floating	*50°	*50°	32°	0.3923	0.0386	0.0492	Minimum U_m
Floating	*70°	*70°	32°	0.2733	0.0346	0.0459	Minimum U_n
Floating	**32°**	**70°**	**70°**	**0.2733**	**0.0346**	**0.0459**	**Selected**

***** Almost no angular dependence

Table 4.17. Exhaustive search results for the 1L+2SH attached and floating configurations corresponding to the minimum uncertainties in *l*, *m* and *n*.

Coupling	L1	SH1	SH2	U_l / *l*	U_m / *m*	U_n / *n*	Comment
Attached	70°	32°	70°	0.3301	0.0450	0.0775	Minimum U_l
Attached	*32°	32°	70°	0.5168	0.0450	0.0775	Minimum U_m
Attached	*32°	32°	70°	0.3301	0.0450	0.0775	Minimum U_n
Attached	**70°**	**70°**	**32°**	**0.3301**	**0.0450**	**0.0775**	**Selected**
Floating	70°	32°	70°	0.2616	0.0326	0.0540	Minimum U_l
Floating	*32°	32°	70°	0.4437	0.0326	0.0540	Minimum U_m
Floating	*32°	32°	70°	0.2616	0.0326	0.0540	Minimum U_n
Floating	**70°**	**32°**	**70°**	**0.2616**	**0.0326**	**0.0540**	**Selected**

***** Almost no angular dependence

The next three figures show graphical results for the 2L+1SV configuration. Figure 4.6 shows the variation in uncertainty for *l* vs. the SV, L1 and L2 angles, where the angles not varied are set to the values giving the minimum uncertainty in *l*.

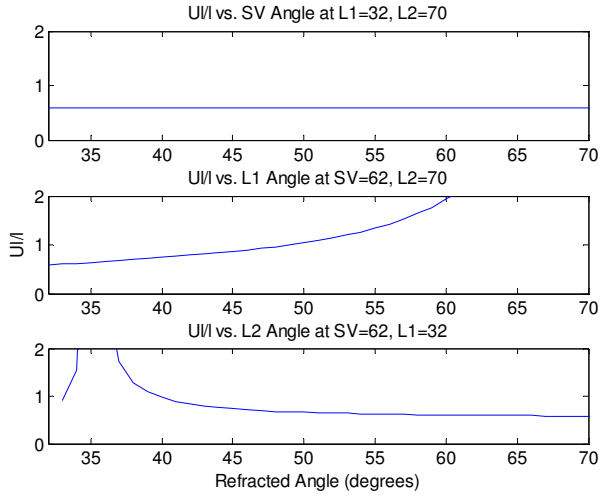

Figure 4.6. U_l / l vs. SV, L1 and L2 angles.

Figure 4.7 shows the variation in uncertainty for m vs. the SV, L1 and L2 angles, where the angles not varied are set to the values giving the minimum uncertainty in m.

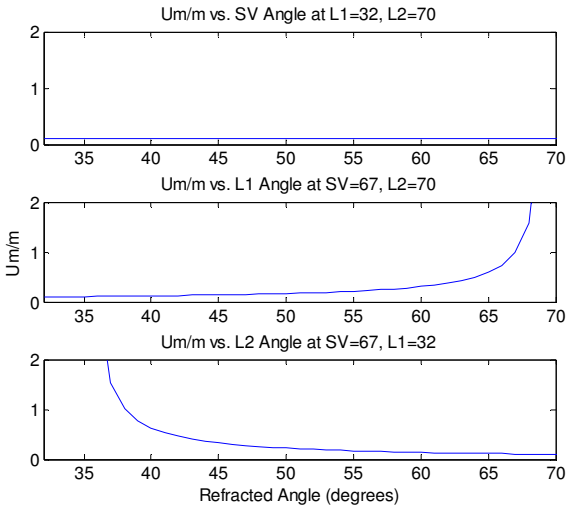

Figure 4.7. U_m / m vs. SV, L1 and L2 angles.

Figure 4.8 shows the variation in uncertainty for n vs. the SV, L1 and L2 angles, where the angles not varied are set to the values giving the minimum uncertainty in n.

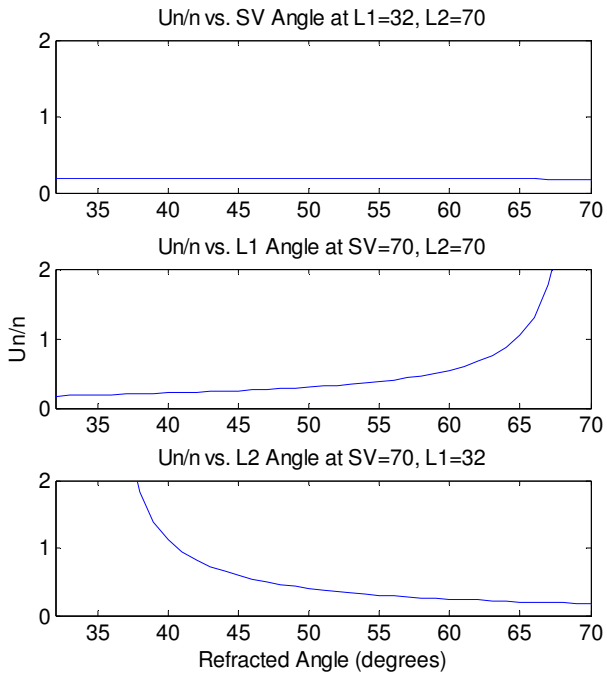

Figure 4.8. U_n / n vs. SV, L1 and L2 angles.

Note that all plots are smooth functions and show the general trend that both L angles must be as far apart as possible. At the points where L1=L2 the singularities appear as peaks in the plots; e.g. Figure 4.6, 2nd plot at L1=70 degrees.

The information shown in Figures 4.6, 4.7 and 4.8 can be thought of as single lines within the "cubes" of data. Various cross-sectional, or 2D, plots provide more information as can be seen in Figures 4.9 – 4.12 for the 2L+1SV configuration.

Figure 4.9 shows U_l / l as a function of L1 and L2 angles at the best SV angle (i.e., SV = 62°). Note the high amplitude ridge near the diagonal showing the large uncertainty that results when L1 and L2 are close together. Figures 4.10 and 4.11 are the analogous plots for U_m / m and U_n / n and have similar characteristics.

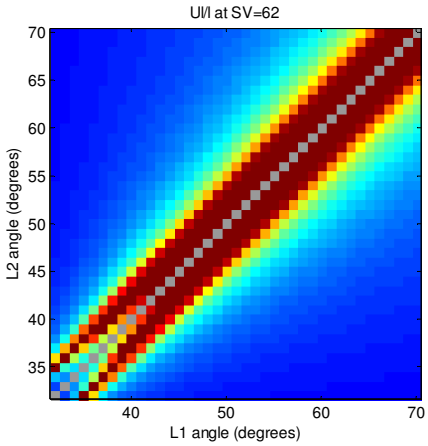

Figure 4.9. U_l / l as a function of L1 and L2 angles at the best SV angle.

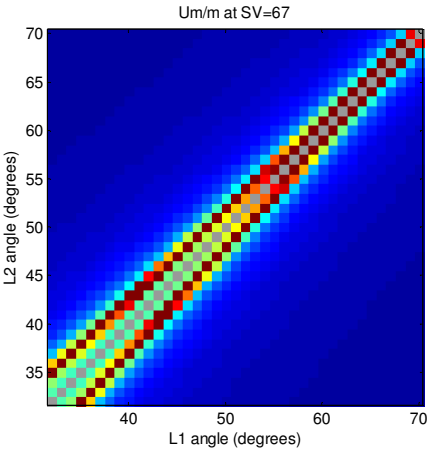

Figure 4.10. U_m / m as a function of L1 and L2 angles at the best SV angle.

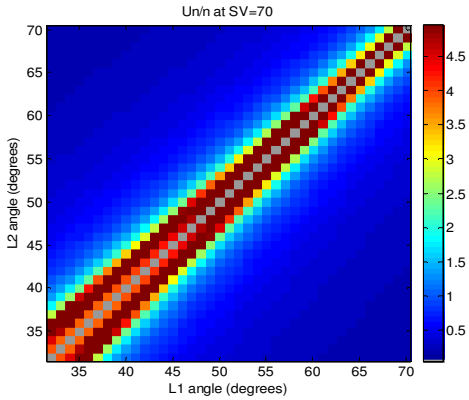

Figure 4.11. U_n / n as a function of L1 and L2 angles at the best SV angle.

Figure 4.12 shows U_n/n as a function of L1 and SV angles at the best L2 angle. Now the singularity is evident as the L1 angle approaches the L2 angle.

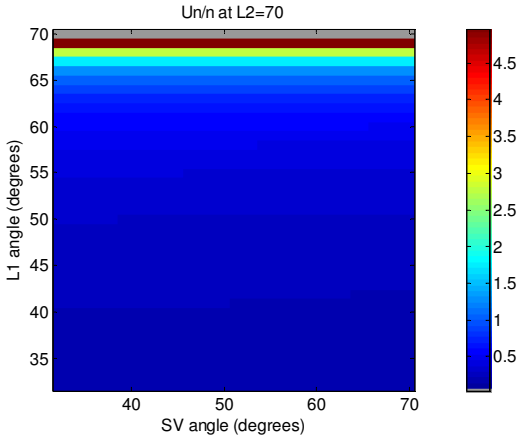

Figure 4.12. U_n / n as a function of L1 and SV angles at the best L2 angle.

The corresponding line plots were generated for the 1L+1SV+1SH floating configuration and are shown in Figures 4.13, 4.14 and 4.15. Note that these plots are much different than the one for the 2L+1SV configuration since there are no singularities, indicating that any combination of angles will yield similar sensitivities. The 2D image plots are not shown because they are relatively flat with no significant features.

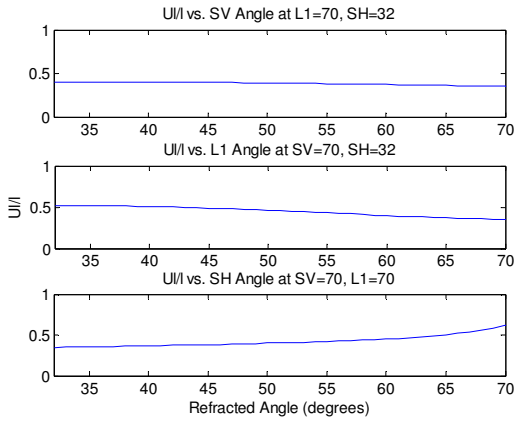

Figure 4.13. U_l / l vs. SV, L1 and SH angles at angles of minimum uncertainty.

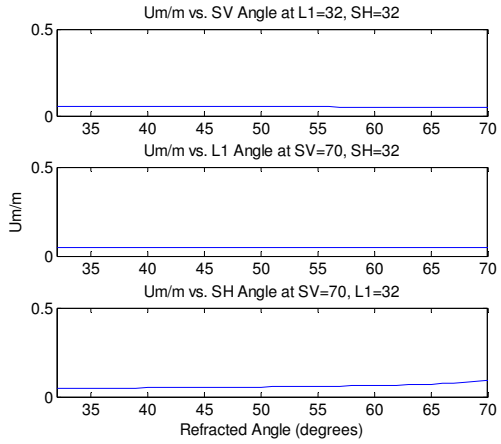

Figure 4.14. U_m/m vs. SV, L1 and SH angles at angles of minimum uncertainty.

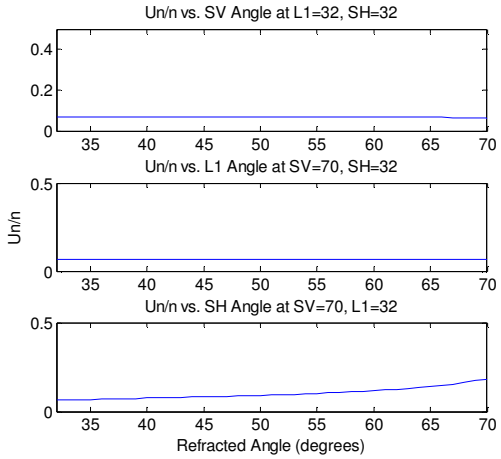

Figure 4.15. U_n/n vs. SV, L1 and SH angles at angles of minimum uncertainty.

The figures are similar for the other floating and attached configurations and are not shown. In general, if there are two common angles (e.g., L1 and L2 or SH1 and SH2), the uncertainty increases as the angles get close to each other, and there is a singularity when they are equal. There is one exception to this behavior and that is in the 2L+1SH solution and shown in Figures 4.16 and 4.17. The uncertainty in n has an unexpected singularity at an SH angle of approximately 60 degrees.

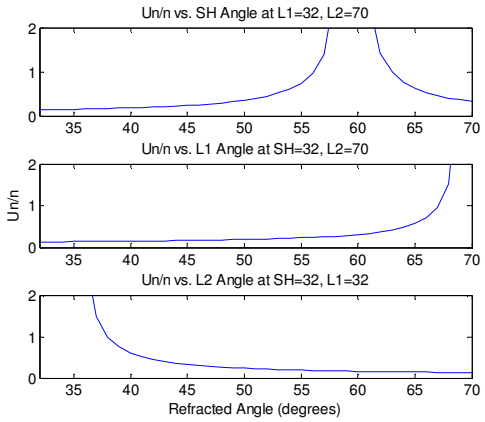

Figure 4.16. U_n / n vs. SH, L1 and L2 at angles giving minimum uncertainty.

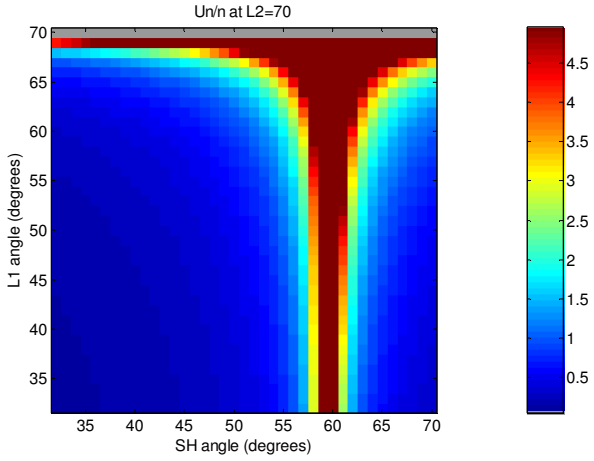

Figure 4.17. U_n / n vs. L1 and SH at the best L2 angle.

4.5.5 Effect of Thickness

The sample thickness is varied in the sample calculation of section 4.4 using the best angles in the common angle approach to see the effect on the recovery of TOECs. Figure 4.18 shows the effect of 1-10 multiples of the base thickness of 6.26 mm. Note that the load in terms of force is constant, causing a reduction in stress as the thickness increases.

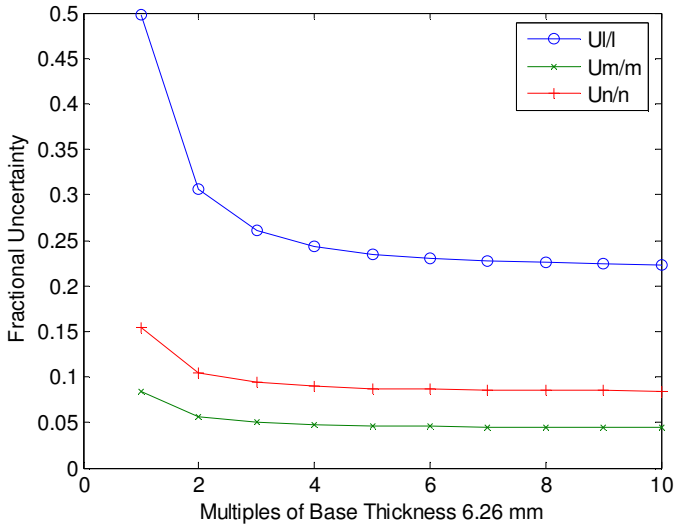

Figure 4.18. Effect of thickness on TOEC recovery uncertainty.

These results show that beyond three thickness multiples, the uncertainty remains relatively constant at approximately half the base values for the *l* TOEC, and approximately two-thirds of the base value for *m* and *n*.

4.5.6 Effect of V-Paths

The number of V-paths is varied in the sample calculation earlier using the best angles in the common angle approach to see the effect on the recovery of TOECs. Intuitively changes in the number of V-paths and thickness should produce similar effects as they both lead to overall changes in path length and hence time shift. This is illustrated in Figure 4.19 as an increase in the number of V paths is directly proportional to increases in transducer separation.

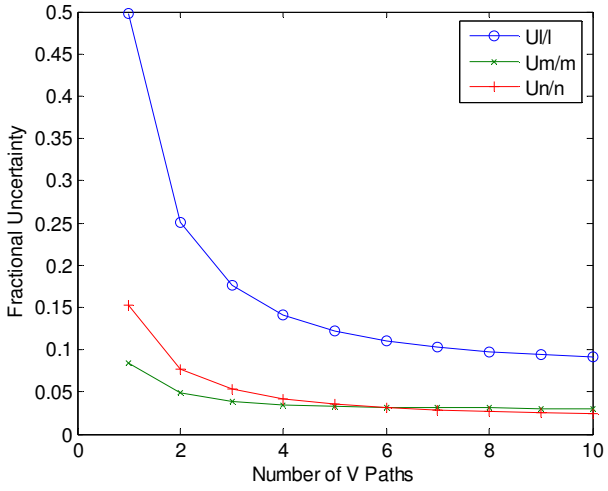

Figure 4.19. Effect of number of V paths on TOEC recovery uncertainty.

The trend is similar to the thickness trends in Figure 4.18 except the reduction is uncertainty is quite a bit more. The reason for the difference is that the stress is not reduced as the number of V paths increases. If the load is increased as the thickness is increased, the plots match quite closely.

An overall increase in path length should lead to a better estimate of the TOECs of the sample since the time shifts are larger. This advantage has to be balanced with the fact that a larger interrogation path may cause other problems such as those resulting from non-uniformity of the specimen and stress distribution.

4.6 Section Summary

Four well-posed solutions are identified and examined in response to the problem posed. A linearised assumption is utilized where the total time shift is due to geometry and acoustoelasticity only. TOEC errors in the use of exact time shifts are small (approx 3GPa) hence assumptions are valid. The numerical results confirm the validity and self-consistency of the procedure for determining TOECs from measured load-dependent time

shifts. In both attached and floating cases, the results show that the resulting constants are very sensitive to experimental errors in measuring mainly time shifts and separation distances. It is also important to keep in mind that some input uncertainty values were conservative and much better values could possibly be realized in the experimental procedures. The best configuration for recovery of TOECs when limited to three measurements for an isotropic material is the floating 1L+1SV+1SH configuration where almost any angles can be used.

CHAPTER 5

EXPERIMENTS

Experiments performed for the recovery of TOECs are reported in this chapter. The experimental setups and procedures used herein are described for acquiring angle-beam acoustoelasticity data for both attached and floating transducer mounting configurations.

5.1 Overview

The acoustoelastic measurement process considered here consists of measuring time shifts of received ultrasonic echoes as a function of applied uniaxial load for a specific angle-beam configuration. The measurement system consists of the following:

1. Spike-mode pulser receiver (Panametrics model 5072PR)
2. Digital oscilloscope (Tektronix TDS5034)
3. Ultrasonic transducers and angle beam wedges
4. Hydraulic loading fixture
5. Computer with MatLab software

A block diagram of the measurement system is shown in Figure 5.1. Tx and Rx represent the transmitting and receiving angle beam transducer/wedge assemblies for sending and receiving ultrasonic waves through the sample. Transducer wedge assemblies are acoustically coupled to an axially loaded specimen for both the attached and floating experiment configurations.

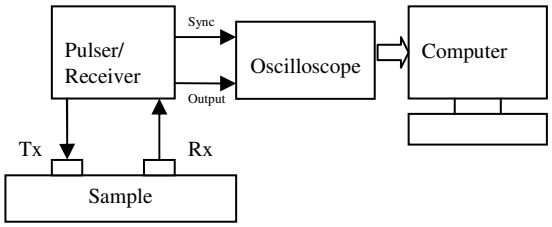

Figure 5.1. Block diagram of measurement setup.

5.2 Samples

Materials studied include 7075-T6 aluminum, 7075-T651 aluminum, 2024 aluminum, and low carbon steel. These materials are essentially isotropic and the selection offers a reasonable range of TOECs for which values have been reported previously. Some of these samples, which are rectangular two hole coupons, are shown in Figure 5.2. They were machined from the center of stock material, all to the same nominal thickness, with the rolling direction along the long axis of the specimens.

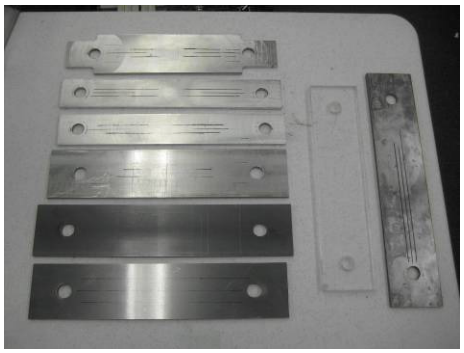

Figure 5.2. All coupons with average dimensions 76.32mm width by 6.32mm thick.

A simple dowel pin grip was used to couple the load to the sample. Measurements were made in the center of specimen sufficiently away from the grips so that a pure uniaxial load is produced in this center region. The maximum load applied in

the measurements to the specimens is approximately 95 kN, which corresponds to a maximum uniaxial stress of approximately 195 MPa in the center cross sectional area of the sample for the nominal specimen geometry used in the experiments.

Two test configurations were used: (1) transducers each at fixed locations on the specimen to approximate the glued-on testing configuration, and (2) transducers attached to a dual angle beam wedge assembly to keep the distance between the transmitter and the receiver fixed as a function of load.

5.3 Loading Fixture

The hydraulic mechanical loading fixture, shown in Figure 5.3, is used to apply a uniaxial tensile load to the specimen via a hydraulic cylinder that is coupled to dowel pin grips at the ends of the specimen. A calibrated load cell placed between the cylinder and the specimen is used to determine the applied load. Loads are applied manually using a hand pump fitted with a pressure gauge. A chart was established to relate the pressure gauge reading to the applied static load from the output of the load cell. The experimental procedures require accurately determining the load and making repeatable measurements.

Figure 5.3. Hydraulic loading fixture.

The stress applied to the sample is calculated by dividing the applied load by the sample's cross sectional area. The 7075-T651 aluminum sample cross sectional area at no load is 4.81×10^{-4} m^2 and strains are determined using Young's modulus *E* and Poisson's ratio *v*. For an applied load of 94.3 kN, the longitudinal and lateral strains $(\varepsilon_{long}, \varepsilon_{lat})$ are $\varepsilon_{long} = 0.00280$ and $\varepsilon_{lat} = -9.662\times10^{-4}$.

Loading was done using two different approaches.

1. Incremental Loading Method. The load was increased monotonically over the range of 0 – 95 kN and time shift data were acquired at 11.8 kN increments.
2. End-Point Loading Method. The load was increased from the lower to upper range limit of 95 kN in one step. Data were acquired and the load released back to the lower 0 load limit.

The latter approach evolved over time as the loading techniques were refined to produce more repeatable results.

The loading fixture hydraulic system performed well for the 0 – 95 kN range of loads applied. Several procedures were followed to ensure accuracy and repeatability of the applied load. It was necessary to bleed the hydraulic system to eliminate any air in the lines, which would lead to errors in the applied and actual loads experienced. It was necessary to ensure that the loading fixture maintained its collinear alignment when large loads were applied so that there was no spin or twist in the specimen. For the measurements reported here, alignment was achieved by careful assembly of the fixture, although it could be modified to use a dial indicator to ensure zero spin over the range of loads applied.

5.4 Ultrasonic Instrumentation

Signals were generated, received, amplified and filtered using a commercially available Panametrics 5072PR pulser-receiver, and typical instrument settings are shown in Table 5.1. Gain (attenuation) is set individually for each data set so that about 85% of the oscilloscope amplitude range is filled with the received waveform for the measurement time range of interest.

Table 5.1. Typical 5072PR pulser receiver settings

Pulse Repetition Frequency	Damping (Ohms)	Energy (µJ)	High Pass Filter (kHz)	Low Pass Filter (MHz)
100 Hz	50	13	1	35

5.5 Waveform Acquisition Instrumentation

A Tektronix TDS5034 digital oscilloscope was used to record waveforms. Signals were digitized at a sampling frequency of 5 GHz and the internal waveform averaging feature of the oscilloscope was used to improve the signal to noise level. Typically, 10 waveform averages were used for each measurement. Recorded waveforms were stored and later transferred to another computer for analysis of time shifts. Waveform signals shift in time slightly as a load is applied to the specimen. These time shifts were recorded using the built in cursor features of the TDS5034 to a resolution of approximately ±2 ns to permit an initial evaluation of time shifts as waveforms were acquired.

A considerable amount of effort was dedicated to ensuring that the waveform was saved at the specific load required because the system used a manual pump without a control system, and hence loads had to be set manually. This step proved challenging as synchronizing the exact load and saving waveforms was tedious.

5.6 Measurement of Time Shifts

The processing of the received signals to obtain time shifts is critical to the TOEC recovery process. Signals are digitized and stored, and these recorded signals are transferred to a PC for analysis with Matlab software. Data analysis consists of accurately measuring the time shift of the desired echo for each ultrasonic signal. Once the correct echo set has been identified, a time window is used to gate that specific echo. The time shift between the signals under the various loading conditions, with zero load as a baseline or reference, is calculated from the time of the peak of the cross-correlation function of the two signals. This time shift is referred to as the "delta time of flight." Since both the reference and echoes at specific load have similar shapes, the cross-correlation method provides an accurate determination of the time shift between the echoes, which is not affected by small changes in the amplitudes of the echoes. The cross correlation program results are cross checked with the manual readings recorded at the time of the measurement from the oscilloscope screen to ensure that the correct echoes were selected for analysis.

The time resolution of the raw signals is 0.2 ns (5GHz). Time shifts are calculated to a resolution of 0.025 ns by interpolating the output of the cross correlation via piecewise cubic spline interpolation. Because there are many factors that affect the actual time shifts with load, as is discussed in a later section, the overall repeatability of

time shift measurements in on the order of ±1ns. This repeatability is not limited by the sampling frequency or the signal processing. For the incremental load method, time shift versus load data are then fit to a straight line and the slope obtained is used for determination of the acoustoelastic constants.

5.7 Transducers and Angle Beam Wedges

Individual angle beam wedges were purchased to generate the desired refracted angles for samples of 7075 aluminum. Calculations and adjustments were then made to test other materials. Careful characterization of wedges is a critical step in this angle beam work. Perspex wedges were designed to generate the desired refracted angles for both L and S waves.

The 2L+1SV solution requires both L and SV wedges. Figure 5.4 shows propagation paths of 2, 3 and 4 V paths or skips through the material. The transmitter sends a pure L wave incident at the Perspex/sample interface at an oblique angle. If the incident wave in the wedge is between the first and second critical angles, only an SV refracted wave is generated in the sample. If an L wave is desired, the incident angle must be below the first critical angle. Then, both L and SV refracted waves are generated, and the desired L wave echo must be identified within a waveform which also contains echoes from shear wave modes.

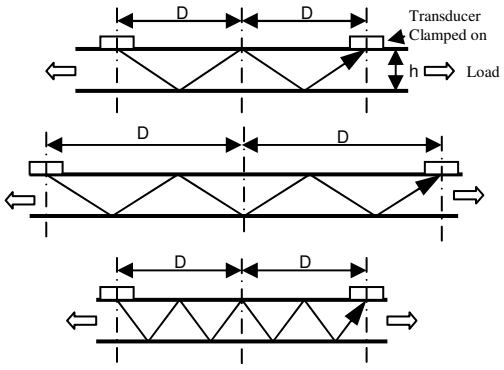

Figure 5.4. Propagation paths corresponding to 2V-SV, 3V-L and 4V-L.

5.7.1 Attached Configurations (Variable Separation Distance)

Table 5.2 shows transducer wedge specifications that were used for the attached transducer tests. Two longitudinal and two shear wedge pairs were used for attached transducer tests on 7075-T6 aluminum and low carbon steel. Refracted angles were checked using a 7075-T6 aluminum angle beam calibration block. The refracted angles listed for low carbon steel were then calculated using well-known acoustic velocities for 7075 aluminum and low carbon steel.

Table 5.2. Attached tests Perspex wedge angles.

Wedge Set	Angle AL7075	Angle LCS		Wedge	Angle AL7075	Angle LCS
L #1	45	42.2		SV #3	42.2	45
L #2	60	55.4		SV #4	63.2	70

Most of the wedges of Table 5.2 were custom fabricated from Olympus Accupath miniature wedges to attain desired refracted angles; a photo is shown in Figure 5.5. These wedges are used with Olympus miniature screw-in transducers, V543-SM (5 MHz) and V544-SM (10 MHz), with 0.25" element diameters.

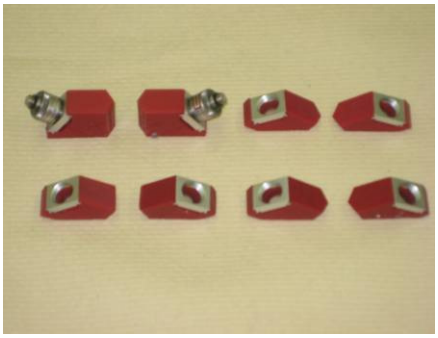

Figure 5.5. Wedge pairs used for attached tests.

An adjustable clamp with rubber jaws was used to hold each wedge at a fixed/known position during the "glued on" tests. Actual glued on wedges were not used because of the difficulty encountered in removing wedges after testing without destroying the wedges.

5.7.2 Floating Configurations (Fixed Separation Distance)

In the floating tests, for the L and SV measurements, in order to keep the separation distance fixed, two Technisonic Research fingertip wedges were bonded together using a rigid epoxy to bridge the gap between them. The distance was set to generate the desired number of V paths in the 7075 aluminum specimens. The pair is then one solid piece as shown in Figure 5.6 and can be clamped to the sample as an integrated unit. These wedges were used with Technisonic Research removable fingertip transducers, 5 MHz, with an element diameter of 0.25". The same wedges and transducers were used for all samples for the floating test configuration.

Implementation of the SH wave measurements requires shear wave transducers directly attached to a wedge that is machined to the desired incident angle. An SH wedge block was made from an aluminum block with the same material properties as the

aluminum sample. A photo of the setup is shown in Figure 5.7. The use of an aluminum wedge results in no refraction at the wedge-sample interface for aluminum specimens, and very little refraction for low carbon steel specimens.

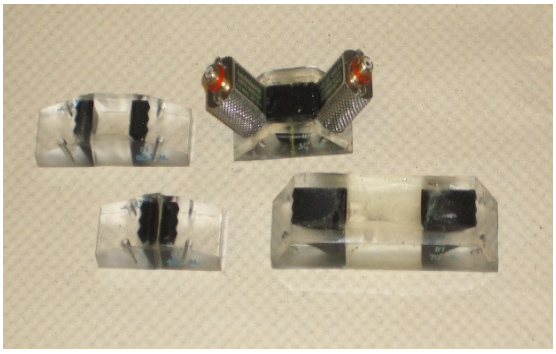

Figure 5.6. Perspex wedge pairs used for the L and SV floating angle beam measurements

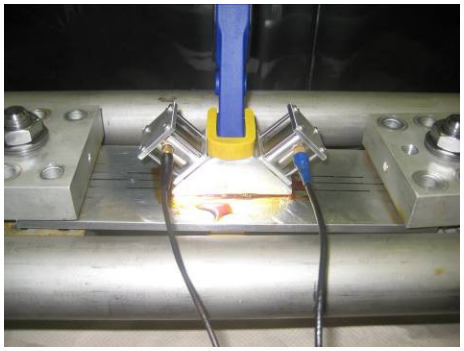

Figure 5.7. Aluminum wedge block used for SH angle beam measurements.

Wedge characterization details and expected times-of-flight are shown in Table 5.3 for all wedges and wedge pairs used for the L, SV and SH floating configuration. Times-of-flight were obtained using calculations as outlined in the following example. Consider a 1V-L path with a refracted angle of 60 degrees, a separation distance of 2*D*, and a sample thickness of h = 6.26 mm. Further, assume the wave propagates along straight lines for the full V path. The distance 2*D* is calculated as,

$$2D = 2h\tan(\theta) = 2(6.26\text{ mm})\tan(60^\circ) = 21.697\text{ mm}. \quad (5.1)$$

Taking into account the actual ultrasonic beam exit point from the wedge and a measured distance of 5.276 mm from this exit point to the front edge of the wedge, a 1V-L path corresponds to a front edge-to-front edge separation distance of 11.179 mm (21.697mm – 2×5.276mm). The total transit time from generation of the transmit pulse to recording of the received echo, time of flight (TOF), is next calculated using actual wedge wave path dimensions and the calculated V path length,

$$\text{TOF} = \frac{\text{Path}_{\text{wedge1}} + \text{Path}_{\text{wedge2}}}{c_{Perspex}} + \frac{\text{Vpath}}{c_{AL}}, \quad (5.2)$$

where $c_{Perspex}$ is the longitudinal wave velocity of Perspex (2.72 mm/μs) and c_{AL} is the longitudinal wave velocity of 7075-T651 aluminum (6.21 mm/μs).

Table 5.3. Wedge angles and expected times-of-flight for floating configuration wedge pairs

Wedge Type	Angle 7075AL (degrees)	Angle LCS (degrees)	Wedge#1 Path (mm)	Wedge#2 Path (mm)	Wedge Path (mm)	Individual Wedge Path TOF (μs)
45L	45	42.2	8.5	8.5	17.1	3.1
60L	60	55.4	8.2	8.2	16.5	3.0
45SV	45	47.9	7.1	7.1	14.2	2.6
70SV	70	63.2	12.5	12.5	25.0	4.6

5.8 Fixed Transducer Configuration Measurement Procedure

The 2L+1SV solution is experimentally explored in the fixed transducer configuration. Two 5 MHz transducers, Olympus V543, are first coupled to the appropriate wedge using Olympus A (propylene glycol), then the wedge/transducer assembly is coupled to the sample using the same couplant. When the transducer/wedge

pair is physically glued to the sample, there is no need for a holding fixture. However, it is challenging and time consuming to remove a glued wedge from the sample, and sometimes wedges were damaged during the removal process. Hence clamps were used to hold assemblies in an intermediate step. Specifically, two holding clamps are used, one for the transmitter and the other for the receiver. Guide lines were scratched lightly in the surface of the sample to ensure that the transducers were aimed directly at each other with the beam path along the major axis of the specimen. Factors such as transducer beam skew and transducer-to-transducer refracted angle variations can vary transducer placement and hence the quality of the signal received.

Figure 5.8 is the measurement setup, which shows the specimen held in the loading fixture with the wedges individually coupled and clamped to the specimen. Note that for the attached transducer configuration, the transmitter and receiver separation distance varies with the applied load. The transducer/wedge position and alignment are based upon calculated distances for the mode, refracted angle, and number of V paths desired as was discussed previously. One disadvantage of this setup is that the size of the wedges and clamps restricts the minimum separation distance between assemblies and requires the use of multiple V paths to obtain an integral number of V paths between the wedge pairs. Clamping forces are much less than the load applied to the specimen and thus do not perturb the state of stress in the specimen. The method shown in Figure 5.8 is used for the final tests because the transducers were not glued in place.

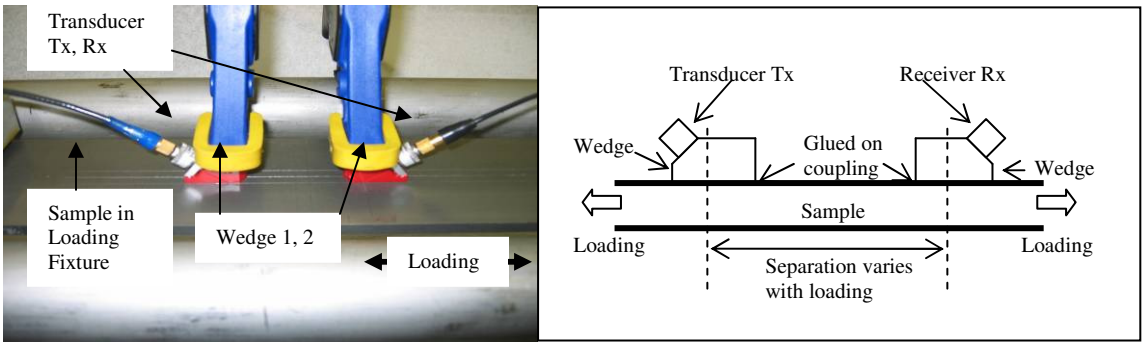

(a) (b)

Figure 5.8. (a) Attached configuration angle-beam measurement setup (b) Drawing of one possible attached transducer assembly.

Time shift measurements were made by monotonically loading the specimen over a predetermined range and manually recording the actual load and resulting time shift relative to the unloaded state or baseline at each load increment. The loading and data capture were synchronized manually. The general procedure, once the sample is placed in the fixture, is to increase the load in nominal 11.8 kN increments from zero load to a full load of 95 kN and the later corresponds a stress level of approximately 195 MPa in all the specimens that were tested. The waveform is captured and the actual load recorded at each load step. In order to check for hysteresis, some readings were also taken at the same load increments during the unloading cycle.

Table 5.4 gives a summary of measurement configurations and Table 5.5 gives the expected arrival times for 7075 aluminum. The arrival times account for propagation through the wedges. The wedges available result in two sets of data for recovery of TOECs by using the 45SV and the 70SV wedges in the 2L+1SV solution.

Table 5.4. Summary of angle beam measurement configurations for aluminum and low carbon steel (LCS) 6.32 mm thick with Perspex wedges.

Material	Wave mode	No. of V paths	Incident angle θ_i	Refracted angle θ_R	Path length (mm)	Transducer separation 2D (mm)
AL7075	SV	2	53.0	64.6	56.0	49.9
	SV	2	36.4	42.2	34.1	22.9
	L	3	22.3	60.0	75.8	65.7
	L	4	18.1	45.0	71.5	50.6
	L	3	24.3	70.0	110.9	104.2
LCS	SV	2	53.0	70.0	74.4	69.9
	SV	2	36.4	45.0	35.7	25.3
	L	3	22.3	55.4	67.2	55.3
	L	4	18.1	42.2	68.8	46.3
	L	3	24.3	63.3	84.8	75.7

Table 5.5. Expected times-of-flight for the 7075 aluminum measurements for all wedge pairs.

AL Wedge Type	Wedge#1 Path (mm)	Wedge#2 Path (mm)	Total Wedge Path	Sample Path (mm)	TOF (μs) AL7075
2V-64.6SV	12.00	12.00	24.00	55.97	26.43
4V-45L	5.17	5.17	10.34	71.50	15.32
3V-60L	6.00	6.00	12.00	75.84	16.62
3V-70L	6.50	6.50	13.00	110.87	22.64

5.9 Floating Transducer Configuration Measurement Procedure

The majority of the measurements made in this research utilized the floating transducer configuration as it proved to be much less labor intensive. The wave propagation description is the same as in the attached case with the primary difference being that there is a fixed separation distance between transmitter and receiver even when

loads are applied. Three floating pair solutions are considered experimentally, namely the 2L+1SV, 1L+1SV+1SH and the 2L+1SH solutions.

A single fixture is required to hold the transducer/wedge assemblies in contact with the sample while waveforms are acquired. The fixture design allows alignment of the transducer with respect to the face of the sample and ensures that the transducer assembly is perpendicular to the sample. A photograph of the specimen with one transducer pair is shown in Figure 5.9 where an integrated assembly consisting of two wedges and two transducers is clamped against the specimen. Clamping shown in Figure 5.9 is with a rubber tipped C-clamp and forces are assumed small and do not perturb the state of stress in the specimen. The transducer-to-transducer spacing remains constant and the entire dual-transducer/wedge assembly "slides" along the specimen as it is loaded after being coupled with light weight oil. The transducer assembly is placed in the center of the sample and aligned with marks drawn on the specimen surface to assure proper alignment. This mounting configuration, although not suitable for in situ measurements, permits evaluation of the floating method in the laboratory.

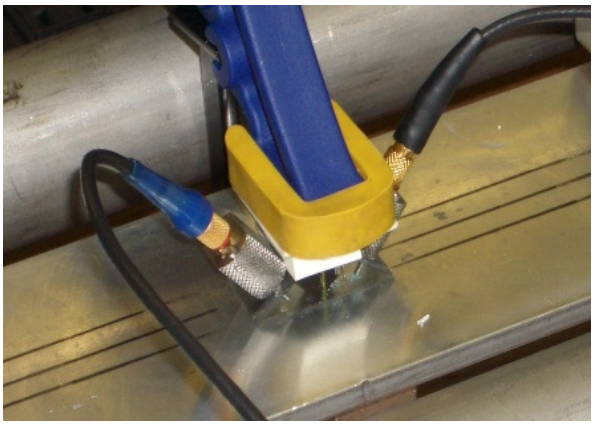

Figure 5.9. Floating configuration angle-beam measurement setup showing the transducers and aluminum sample.

Three different sets of transducer pairs were used at various development stages.

1. Two 5 MHz center frequency with 0.25” element diameter from Panametrics.
2. Two 5 MHz center frequency from Technosonics.
3. Panametrics 5 and 10 MHz shear wave transducers.

Figure 5.10 shows earlier transducer assemblies used in the floating tests.

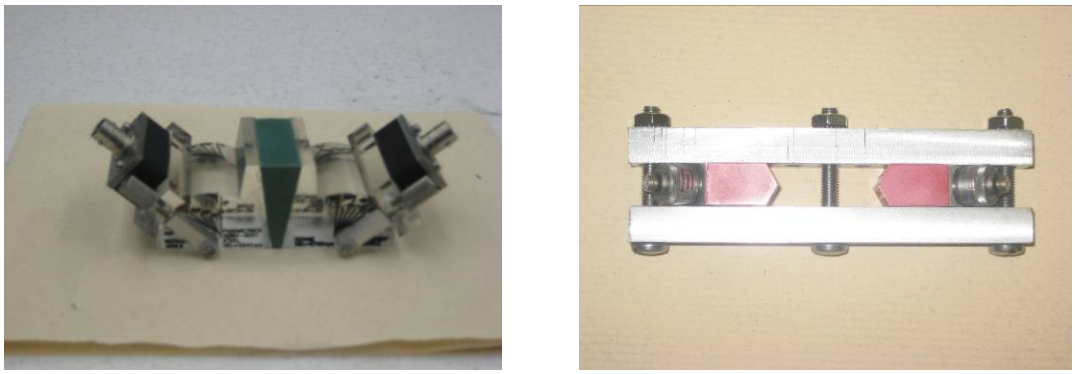

Figure 5.10. Floating pair assembly with variable angle adjustments (left) and floating pair assembly with wedges clamped together to maintain separation distance (right).

The two loading approaches described previously were used to acquire time shift data in the floating configuration. The first approach, the incremental load method, is the same as that described in the attached case where data were taken at 11.8 kN increments over the loading range. Later in this work the second approach, the end-point load method, was used to improve measurement repeatability. The sample was quickly loaded to the maximum load followed by unloading the specimen back to zero load. This procedure minimized time shifts from other factors, such as from the relaxation of stress within the wedge assembly and gradual couplant thickness variations.

The final procedure used for the floating pair measurements is as follows:

1. Record the waveform from the unloaded specimen
2. Quickly load the specimen to a precalculated maximum

3. Record the actual load and waveform
4. Release the load
5. Record the waveform at the nominal zero-load state.

Steps 2-5 are then repeated four more times in succession, resulting in a total of nine stored waveforms.

Time shifts are calculated using the same data analysis procedures as discussed for the attached pair tests. As before, time shifts are calculated to a resolution of 0.025 ns from the interpolated cross correlation between waveforms captured at various load conditions. In all, a total of eight time shifts are calculated, i.e., four for loading and four for unloading. Experience has shown that the unloading segments yield the most consistent and repeatable data, so these four time shifts are averaged to obtain the final time shift. The repeatability/accuracy of the time shift from the floating transducer tests is estimated to be about ±1ns. The transducer wedge assembly is removed, recoupled and replaced after each test to ensure transducer coupling consistency. A sample of a time shift data set from a floating transducer test is shown in Figure 5.11.

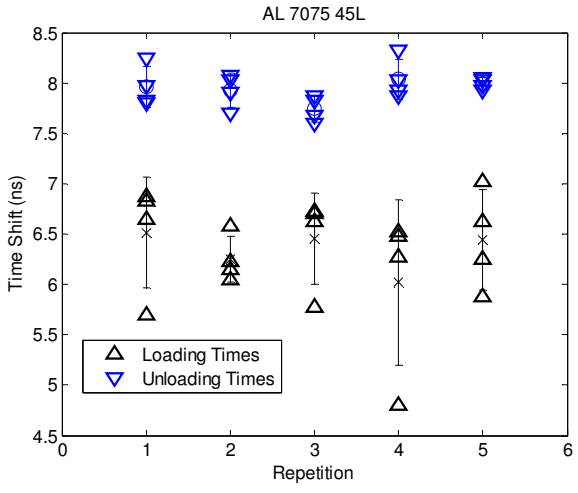

Figure 5.11. Typical set of time shift data results for 45L wave signals

For each measurement, five sets of data were taken, each having nine waveforms. Table 5.6 gives a summary of 2L+1SV measurement configurations for all samples using the first loading approach with multiple V paths. Table 5.7 gives a summary using the second loading approach for the 2L+1SV, 2L+1SH and 1L+1SV+1SH solutions. Single V paths are used for these measurements since longer paths made it difficult to distinguish between echoes from various propagation modes.

Table 5.6. Summary of 2L+1SV angle beam measurement configurations using the incremental load method with multiple V paths.

Material	**Wave mode**	**Incident angle θ_i**	**Refracted angle θ_R**	**Path Length (mm)**	**Transducer Separation *2D* (mm)**
AL7075-T6 6.26 mm	2V-SV	39.2	45.0	35.4	25.0
	1V-SV	57.2	70.0	36.6	34.4
	4V-L	17.7	45.0	70.8	50.1
	3V-L	21.8	60.0	75.1	65.1
AL7075-T651 6.15 mm	2V-SV	39.2	45.0	34.8	24.6
	1V-SV	57.2	70.0	35.9	33.8
	4V-L	17.7	45.0	69.6	50.1
	3V-L	21.8	60.0	73.8	63.9
AL2024 6.36 mm	2V-SV	39.2	45.5	36.3	25.9
	1V-SV	57.2	71.5	40.1	38.0
	3V-L	17.7	43.7	52.8	36.5
	2V-L	21.8	57.8	47.7	40.5
Low Carbon Steel 6.32 mm	2V-SV	39.2	47.9	37.7	28.0
	1V-SV	57.2	80.6	77.3	76.3
	3V-L	17.7	41.0	50.3	33.0
	2V-L	21.8	53.6	42.6	34.3

Table 5.7. Summary of 2L+1SV, 2L+1SH and 1L+1SV+1SH angle beam measurement configurations using the end-point load method with single V paths.

Materials	Wave mode	Incident angle θ_i	Refracted angle θ_R	Path Length (mm)	Transducer Separation *2D* (mm)
AL7075-T6 6.26mm, AL7075-T651 6.26mm, AL2024 6.36mm	SV	39.2	45.0	17.7	12.5
	SV	57.2	70.0	36.6	34.4
	L	17.7	45.0	17.7	12.5
	L	21.8	60.0	25.0	21.7
	SH	39.2	45.0	17.7	12.5
Low Carbon Steel 6.32mm,	SV	39.2	47.9	18.8	13.9
	SV	57.2	80.6	77.4	76.3
	L	17.7	41.0	16.7	10.9
	L	21.8	53.6	21.3	17.1

5.10 Other Measurement Issues

A critical account of all geometrical parameters is important. A micrometer was used to measure the sample thickness at no load to an accuracy of ±0.01mm. Measurements were made at least six times at several positions on the sample in order to gauge the true specimen thickness.

Sensitivity analysis showed that separation distances were the largest contributor to the overall uncertainty in TOEC recovery. For any given refracted angle and V path configuration, the ideal wedge separation distance is calculated based on the assumption that the wave propagation through the material can be represented by straight lines. The challenge lies in finding the true center of the beam and the exact point where the wave leaves the wedge in order to accurately determine separation distance. Attempts with a pinducer (very small transducer) were made to pick up the true center of the beam energy from each wedge, but it was found that the manufacturer's mark for the beam exit point on the wedge was the most consistent means of determining the correct exit point. As

shown in Figure 5.12, all separation distances were measured through a low power microscope with the wedge assembly positioned on a precision linear motion table with a micrometer lead screw. This proved to be a repeatable technique for determining wedge separation distance measurements. The same system was also used to measure the dimensions of all wedges used in this study.

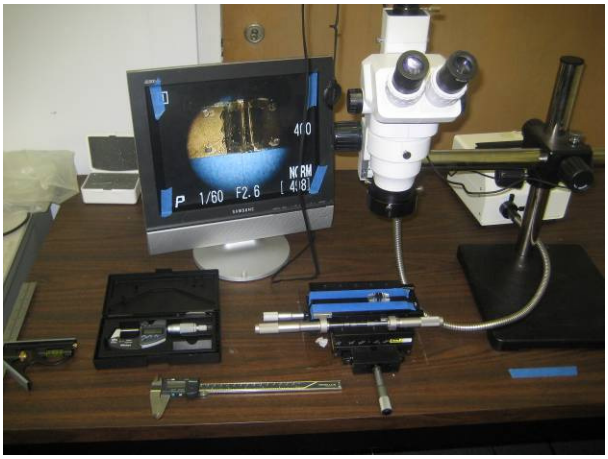

Figure 5.12. Precision linear slide, microscope, calipers and micrometer used for wedge distance separation and specimen thickness measurements.

As the number of V paths increases, the individual echo of interest becomes more challenging to distinguish, particularly for L wave measurements. The persistence mode on the oscilloscope was used to determine the exact position of each signal peak as transducer separation was varied. Chapter 4 showed that as the number of V paths increases, the overall uncertainty becomes significantly lower. Ideally these two factors should be explored to find the best number of V paths which give clear echoes. Later floating tests were limited to single V paths to clearly distinguish received echoes, which does not result in the lowest uncertaintly. All wedge angles were verified using an angle beam calibration block fabricated from 7075-T6 aluminum.

The same physical transducer and wedge were matched each time for similar tests repeated on the same and different materials. Additionally, the same transducer/wedge assembly was always used for transmit and the other for receive for all wedge assembly pairs.

Another factor that affects the performance and accuracy of the technique is that both front and backwall surfaces must be smooth and parallel. If the surface is rough, then the micro variations in thickness will cause the signal to be distorted and may affect the accuracy of the time measurements.

The transducer wedge assembly was removed and replaced after each test to ensure consistency in the measurement process since a major source of error in contact ultrasonics experiments is consistency of the transducer coupling, especially for TOF measurements. This is due to the ability of the operator to consistently reproduce the couplant layer thickness from test to test.

Clamping reproducibility is another factor which affects accuracy of TOF measurements. Any change in clamping conditions can affect the couplant layer thickness, which likewise affects reproducibility of TOF measurements. Specifically, as clamping pressure is increased the couplant layer decreases, which reduces the TOF and slightly shifts the received waveform to the left on the oscilloscope screen, and when the clamp is released the signal shifts back to the right. Thus attempts were made to ensure clamping pressure reproducibility by using the same zero crossing point of the received signal on the oscilloscope screen to determine how tightly to squeeze/hold the wedges. Wedges were also ‘rung in’ to provide an even, repeatable layer between surfaces and a consistent amount of couplant was used. It was determined that four drops of the light oil

was sufficient to provide good coupling while minimizing the amount of excess oil that is squeezed out of the gap.

Over time, constant clamp pressure eventually squeezes all of the couplant out between the wedge and the sample, especially when working with the viscous shear wave couplant used for the SH measurements. For these measurements, special care has to be taken when working with the couplant as it is very viscous and application of a uniform layer can be challenging.

Temperature variations also affect TOF measurements and a detailed account of temperature effect of acoustic wave velocity is given in [38]. Since measurements made here are differential in nature, i.e., TOF differences due to loading, there is no appreciable effect of temperature on the ΔTOF results if the load and unload waveforms are recorded at the same temperature. Care was taken to accomplish this, however, as a sample was loaded from zero load to maximum load then returned to zero load rapidly, a very repeatable temperature change of about 0.5 °F was observed. Thus, for completeness, temperatures were recorded from all experiments from a thermocouple attached to the sample close to the transducer/wedge assembly.

CHAPTER 6

RESULTS: TOEC RECOVERY FOR ATTACHED TRANSDUCERS

In the previous three chapters, TOEC recovery theory was developed and methods outlined for experimental implementations. Experimental investigations were carried out with multiple V paths on specimens of 7075 aluminum and low carbon steel, both with a thickness of 6.32 mm, width 76.32 mm, and surfaces parallel and smooth (Figure 3.1). Experimental results are presented in this chapter for the attached transducer configuration using the 2L+1SV solution. The maximum applied stress was 194.3 MPa, which is well below the yield strength of both materials.

6.1 2L+1SV Forward Problem Results

Experiments were conducted using the incremental load method described in Chapter 5. Typical waveforms are shown in Figure 6.1 for zero load and the maximum applied load of 194 MPa for SV waves with a single 'V' path.

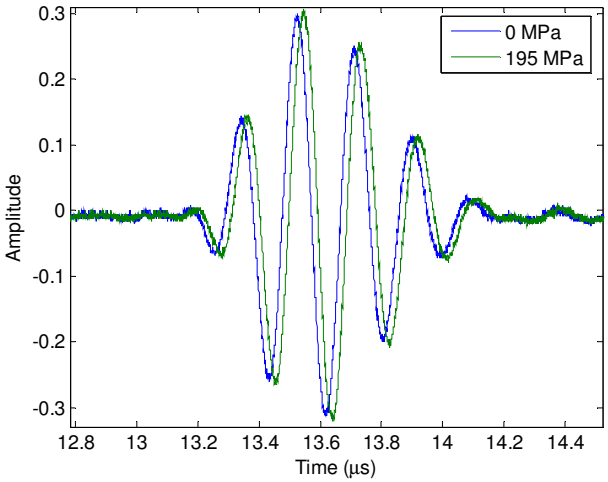

Figure 6.1. Typical SV waveforms at zero load and the maximum load (single V configuration) used for time delay measurement.

Theoretical time shift vs. load values were calculated using the parameters listed in Table 6.1 for both low carbon steel (LCS) and 7075 aluminum. The theoretical time shifts are based on the linearized theory as described in Section 4.2. Experimental time shift versus load curves are shown and compared to theoretical curves in Figures 6.2, 6.3 and 6.4 for the three wave mode configurations and the two materials.

Table 6.1. Parameters for calculating time shift vs. load curves

Parameter	Variable Name	Value for 7075AL	Value for LCS
TOEC #1	l	-252.2×10^9 Pa	-461.0×10^9 Pa
TOEC #2	m	-324.9×10^9 Pa	-636.0×10^9 Pa
TOEC #3	n	-351.2×10^9 Pa	-708.0×10^9 Pa
Sample Thickness	h	6.26 mm	6.26 mm
Sample Width	w	76.29 mm	76.29 mm
45° L # V Paths	N_V	4	4
70° L # V Paths	N_V	3	3
63.2° SV # V Paths	N_V	2	2
Lambda	λ	54.9 GPa	111 GPa
Mu	μ	26.5 GPa	82.1 GPa
Density	ρ	2800 kg/m^3	7800 kg/m^3
Force	F	94,298 N	94,298 N

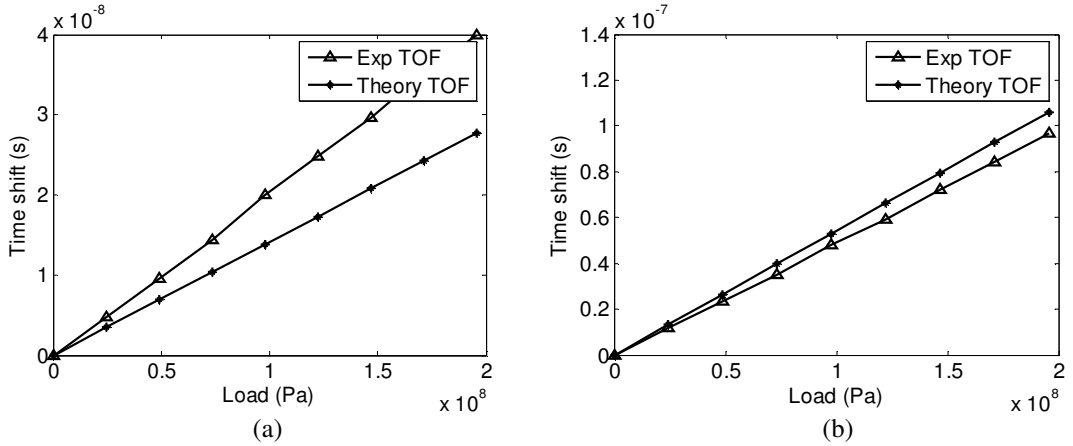

Figure 6.2. Shear vertical double V (2V-SV) time shift vs. load curves for (a) low carbon steel and (b) 7075 aluminum.

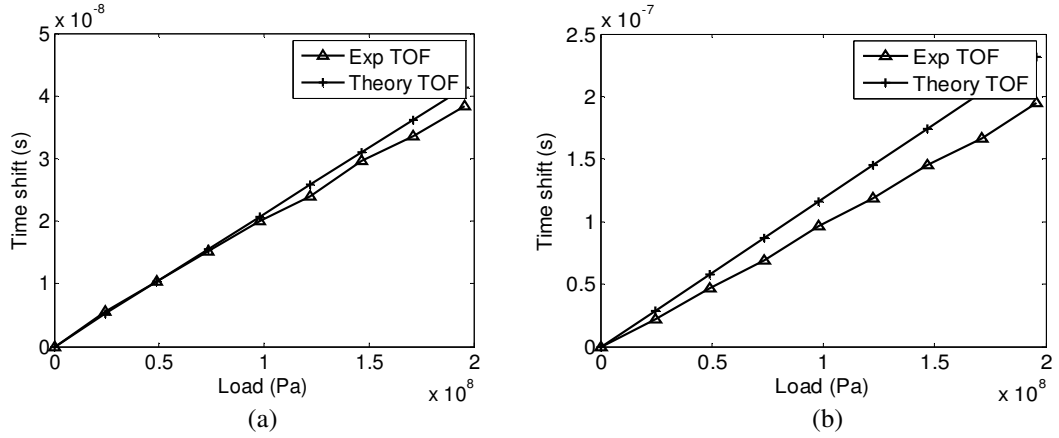

Figure 6.3. Longitudinal triple V (3V-L) time shift vs. load curves for (a) low carbon steel and (b) 7075 aluminum.

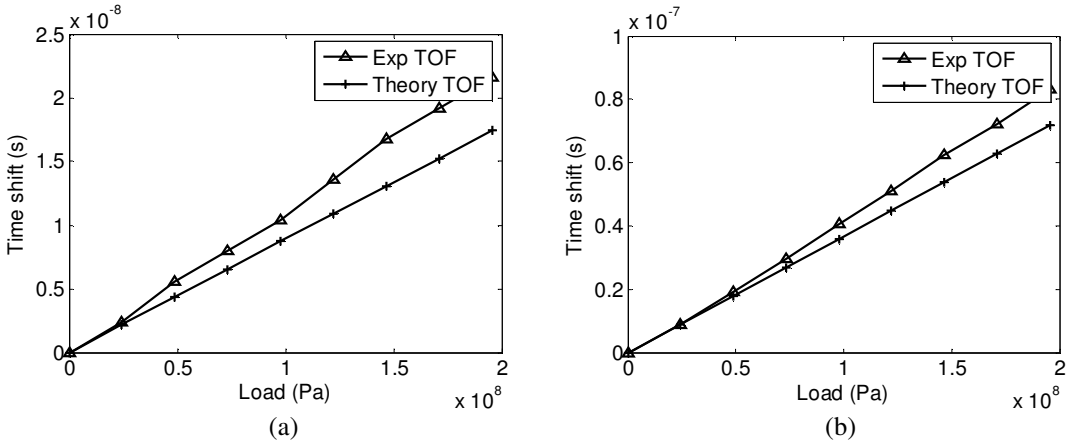

Figure 6.4. Longitudinal 4V (4V-L) time shift vs. load curves for (a) low carbon steel and (b) 7075 aluminum.

Table 6.2 summarizes experimental and theoretical time shifts at the maximum load, and provide a breakdown of the theoretical time shifts into geometrical and acoustoelastic components.

Table 6.2. Time shift analysis at maximum load of 194.26 MPa for 7075 aluminum and LCS.

Material	Wave Mode	Ref Angle (degrees)	Experiment Time Shift (ns)	Theoretical Time Shift (ns)	Theory Time Shift Due to Geometry (ns)	Theoretical Time Shift Due to AE (ns)
Aluminum 7075	2V-SV	63.2	96.8	105.4	36.3	69.1
	3V-L	70.0	195.2	230.5	41.3	189.2
	4V-L	45.0	83.2	71.4	10.5	60.9
Low Carbon Steel	2V-SV	70.0	40.0	27.5	18.6	8.9
	3V-L	63.2	38.4	41.0	10.1	30.9
	4V-L	42.2	21.6	17.2	3.2	14.0

6.2 TOECs Recovered using the 2L+1SV Solution

TOEC values recovered from the time shift data of Table 6.2 for both materials are shown in Table 6.3 below. These results are compared to literature values for similar materials.

Table 6.3. Comparison of recovered TOECs for 7075aluminum and low carbon steel to published values.

Material	TOECs	Present work (GPa)	Prior Work (Gpa)	
Aluminum 7075	*l*	-597.3	-252.2*	-311.0^
	m	-208.8	-325.0*	-401.0^
	n	-517.7	-351.2*	-408.0^
Low Carbon Steel	*l*	-849.5	-461.0**	-328.0^^
	m	-517.7	-636.0**	-595.0^^
	n	-1780.6	-708.0**	-668.0^^

*7075-T651 Aluminum [44]
**Steel Hecla 37 [42]
^Aluminum 2S [42]
^^Steel Hecla 17 [42]

6.3 Section Summary

The experiments show that the acoustoelastic effect in steel is much smaller than in aluminum, which agrees with the results of Smith [42]. The time shifts changed linearly with the applied stress for both materials as the theory predicts. There are deviations between the measured and expected values that have to be further explored. In examining the resulting TOECs of both materials derived from time shift measurements, note that both the 7075 aluminum and low carbon steel materials used for this study may be slightly different alloys than those characterized in the literature studies quoted. Earlier numerical tests showed that the *m* TOEC was the least sensitive in the 2L+1SV solution to the uncertainty in the time of flight measurements (approximately +/- 1ns), and this same observation is reflected in the values for *m* reported in Table 6.2, as *m* values are closest to the expected values. The Fukuoka and Toda results showed a large scatter in the *l* parameter [78], which may be a factor in the deviations observed, since the *l* value has the largest standard deviation in all cases shown.

CHAPTER 7

RESULTS: TOEC RECOVERY FOR FLOATING TRANSDUCERS

The process of determining TOECs using the floating transducer attachment method was carried out experimentally by measuring load-dependent time shifts for specific angle-beam configurations. Measured and calculated time shifts for the forward problem are compared, and the recovered TOECs are compared to literature values. The sensitivity analysis performed earlier for the floating case evaluated the effect of measurement errors in all input parameters on the recovered TOECs. Three solutions were evaluated experimentally using the floating case: the 2L+1SV, 2L+1SH and the 1L+1SV+1SH. The majority of measurements reported are with the 2L+1SV solution. Dimensions of samples and maximum stress values are shown in Table 7.1.

Table 7.1. Specimens used for floating transducer experiments.

Material	Thickness (mm)	Width (mm)	Max Load (MPa)
AL7075-T6	6.26	76.30	194.3
AL7075-T651	6.16	51.13	261.9
AL2024	6.36	76.29	194.3
Low Carbon Steel	6.35	76.29	194.3

7.1 2L+1SV Forward Problem Results

Experimental results are presented here for the forward problem of determining time shifts for applied loads. As discussed earlier in chapter 5, two loading methods were used in making time shift vs. load measurements.

1. Incremental Loading Method. Waveforms were recorded at fixed increments from zero load to maximum load.
2. Endpoint Loading Method. Signals were recorded at zero and maximum loads.

Typical L, SV and SH waveforms are shown in Figure 7.1 for the single V floating case applied to the AL7075-T6 sample. The zoomed views highlight the echoes of interest.

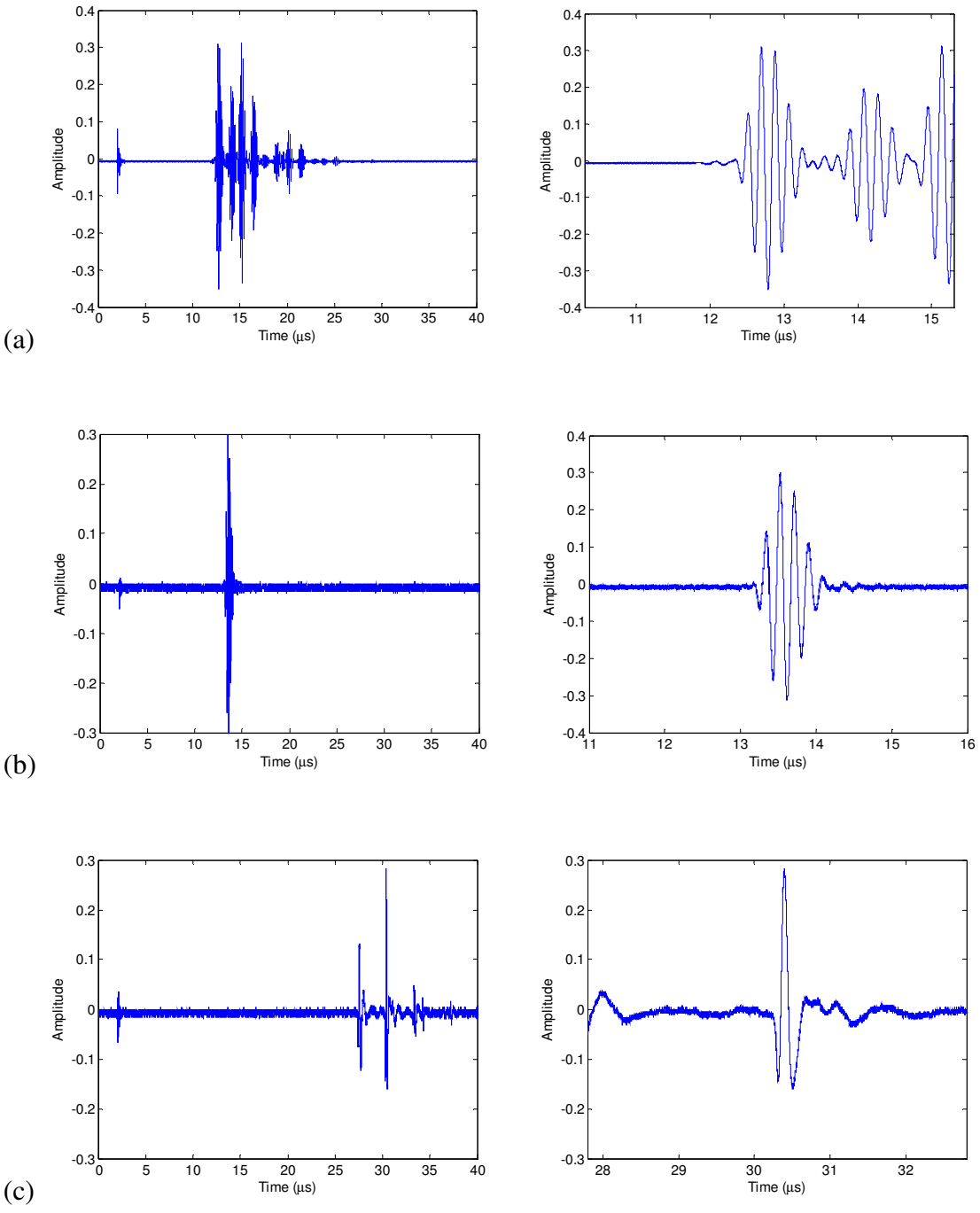

Figure 7.1. Typical waveforms showing echoes of interest for (a) L, (b) SV and (c) SH wave modes.

7.1.1 Incremental Loading Method

For this loading method, data are acquired over a range of 0-194 MPa at increments of 24.5 MPa. Materials tested are 7075-T6 and 7075-T651 aluminum, 2024 aluminum, and low carbon steel. Tests were done using both single and multiple V path configurations. Theoretical time shift vs. load values were calculated for single and multiple V paths using the parameters listed in Table 7.2 for the four materials. The theoretical time shifts are based on the linearized theory as described in Section 4.2.1.

Table 7.2. Parameters for calculating time shift vs. load curves

Parameter	Variable Name	Values for 7075-T6 AL	Values for 7075-T651 AL	Values for 2024 AL	Values for LCS
TOEC #1	l	-252.2×10^9 Pa	-252.2×10^9 Pa	-252.2×10^9 Pa	-461.0×10^9 Pa
TOEC #2	m	-324.9×10^9 Pa	-324.9×10^9 Pa	-324.9×10^9 Pa	-636.0×10^9 Pa
TOEC #3	n	-351.2×10^9 Pa	-351.2×10^9 Pa	-351.2×10^9 Pa	-708.0×10^9 Pa
Sample Thickness	h	6.26 mm	6.16 mm	6.36 mm	6.26 mm
Sample Width	w	76.29 mm	51.13 mm	76.29 mm	76.29 mm
Lambda	λ	54.9 GPa	54.9 GPa	56.93 GPa	111 GPa
Mu	μ	26.5 GPa	26.5 GPa	27.7 GPa	82.1 GPa
Density	ρ	2800 kg/m^3	2800 kg/m^3	2780 kg/m^3	7800 kg/m^3
Force	F	94,298 N	82,510 N	94,298 N	94,298 N

Theoretical and experimental time shift vs. load curves are shown in Figures 7.2 and 7.3 for 7075-T6 using the 2L+1SV solution with multiple and single V paths, respectively. Constants l, m and n as shown in Table 7.2 were previously characterized for AL7075-T651 by Stobbe [44] using conventional ultrasonic methods (i.e., beam paths perpendicular to the loading direction). These experiments were done with the transducer pairs shown in Figures 5.8 and 5.9. The corresponding curves for 7075-T651 are shown in Figures 7.4 and 7.5, those for 2024 aluminum in Figures 7.6 and 7.7, and those for low carbon steel in Figures 7.8 and 7.9.

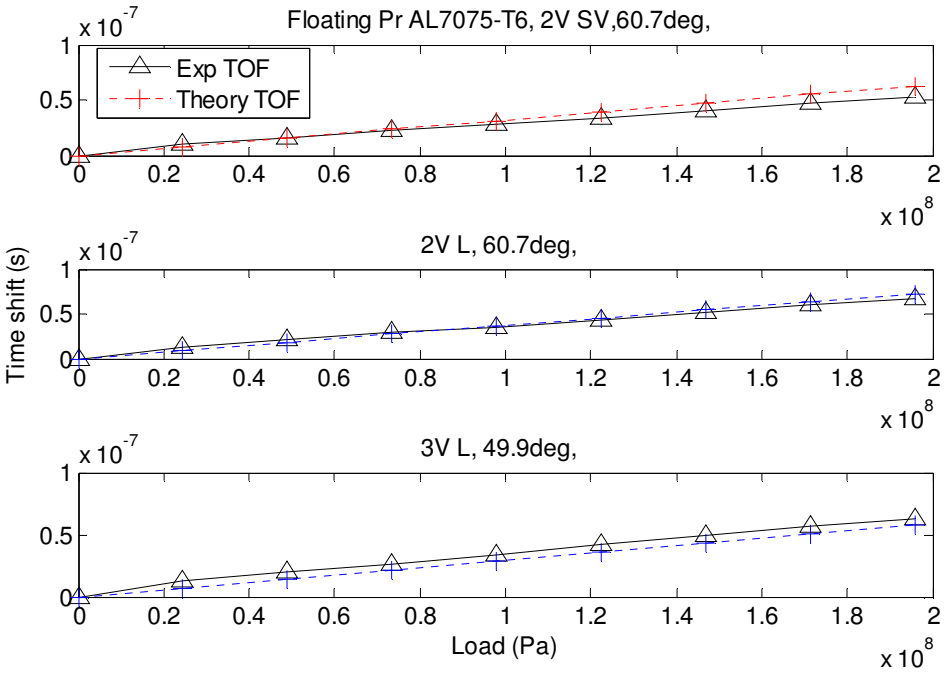

Figure 7.2. Floating 2L+1SV time shift vs. load curves for 7075-T6 aluminum with multiple V paths.

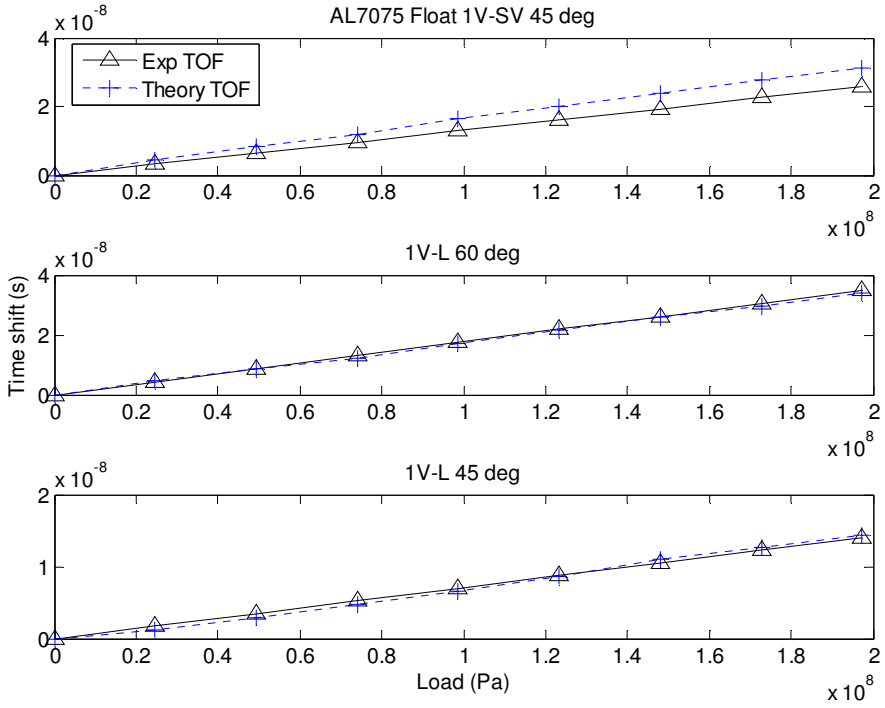

Figure 7.3. Floating 2L+1SV time shift vs. load curves for 7075-T6 aluminum with single V paths.

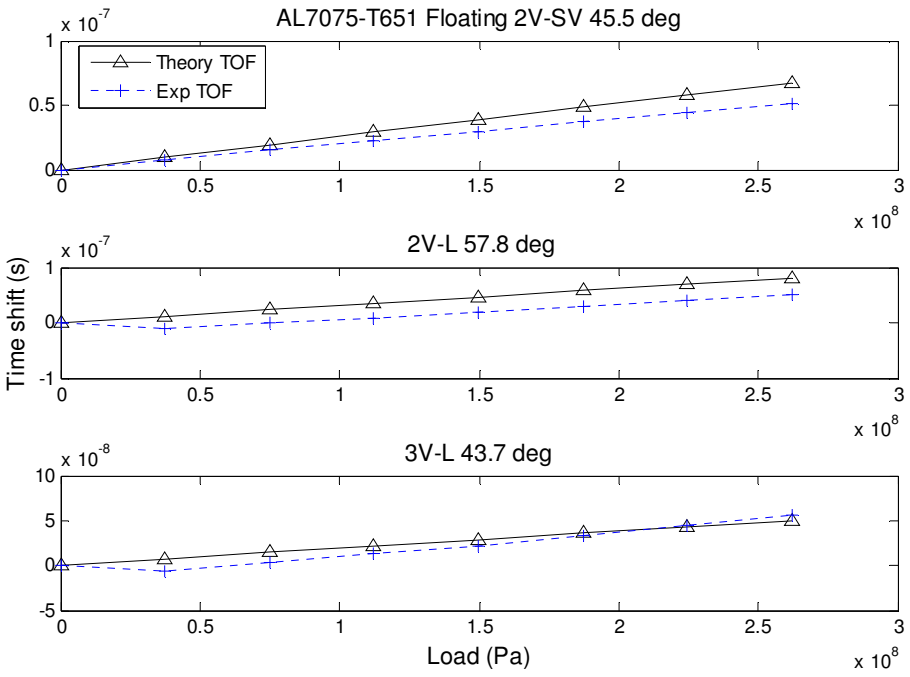

Figure 7.4. Floating 2L+1SV time shift vs. load curves for 7075-T651 aluminum with multiple V paths.

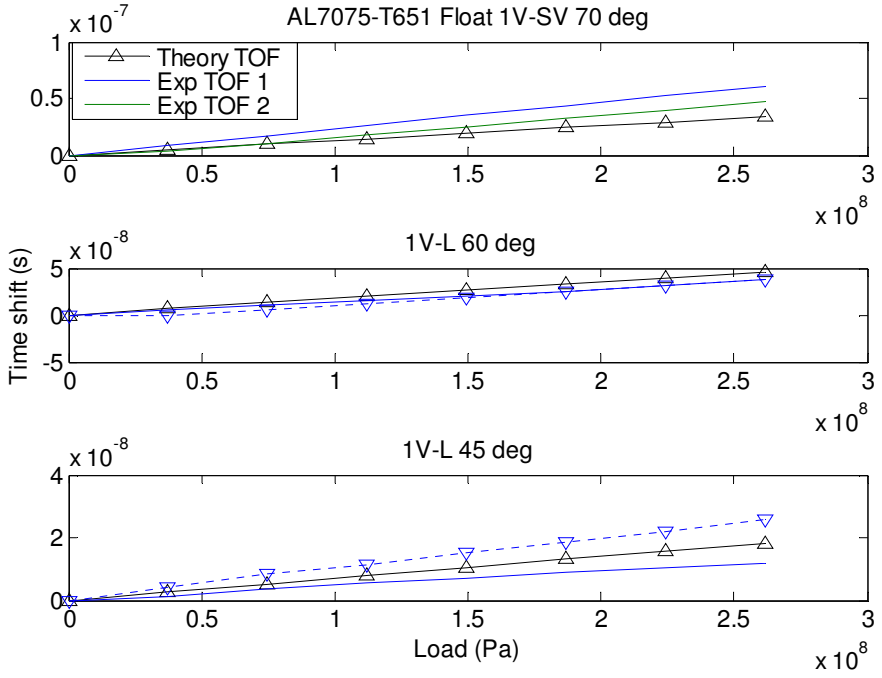

Figure 7.5. Floating 2L+1SV time shift vs. load for 7075-T651 aluminum with single V Paths

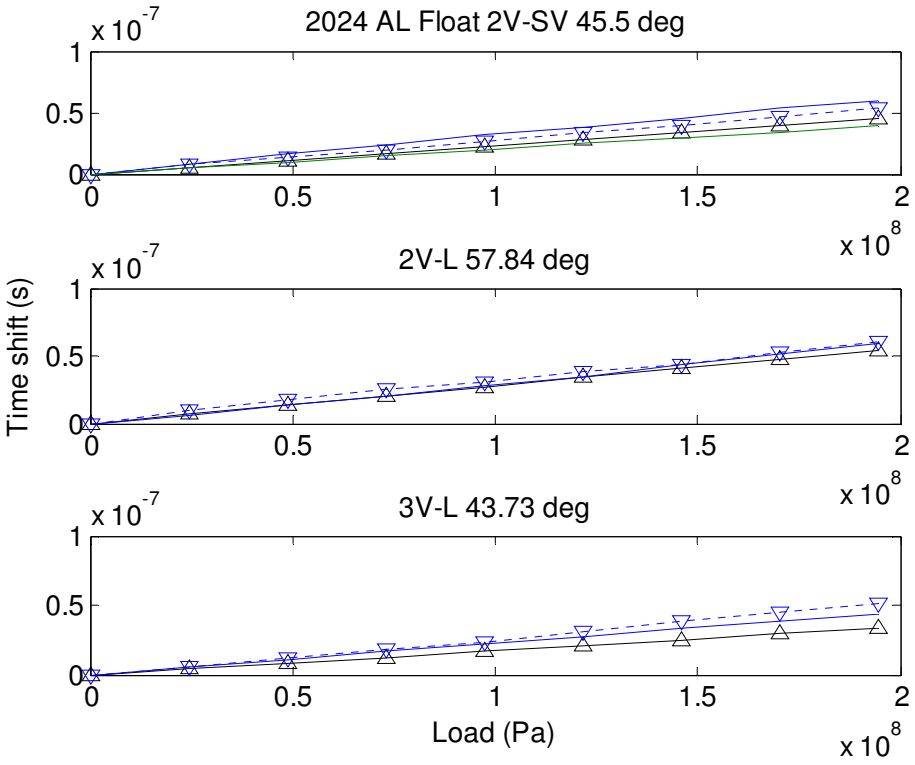

Figure 7.6. Floating 2L+1SV time shift vs. load curves for 2024 aluminum with multiple V paths.

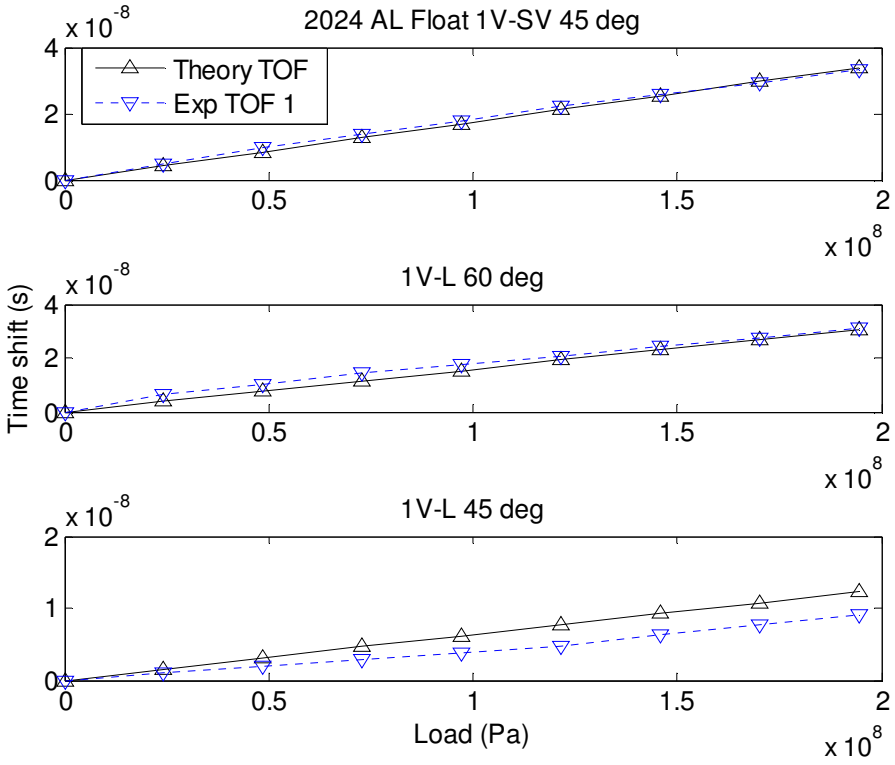

Figure 7.7. Floating 2L+1SV time shift vs. load curves for 2024 aluminum with single V paths.

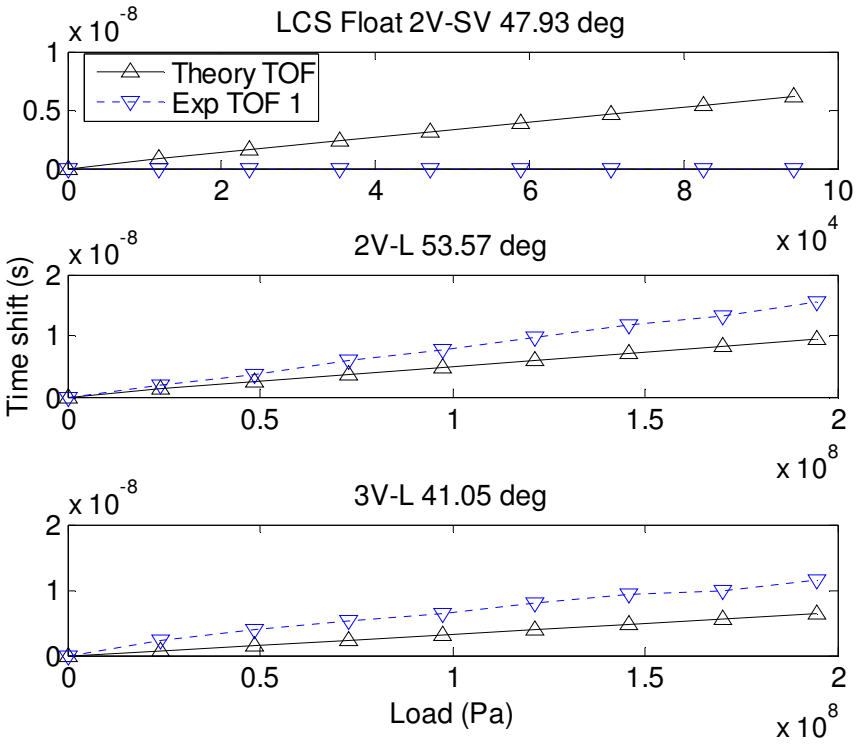

Figure 7.8. Floating 2L+1SV time shift vs. load curves for low carbon steel with multiple V paths.

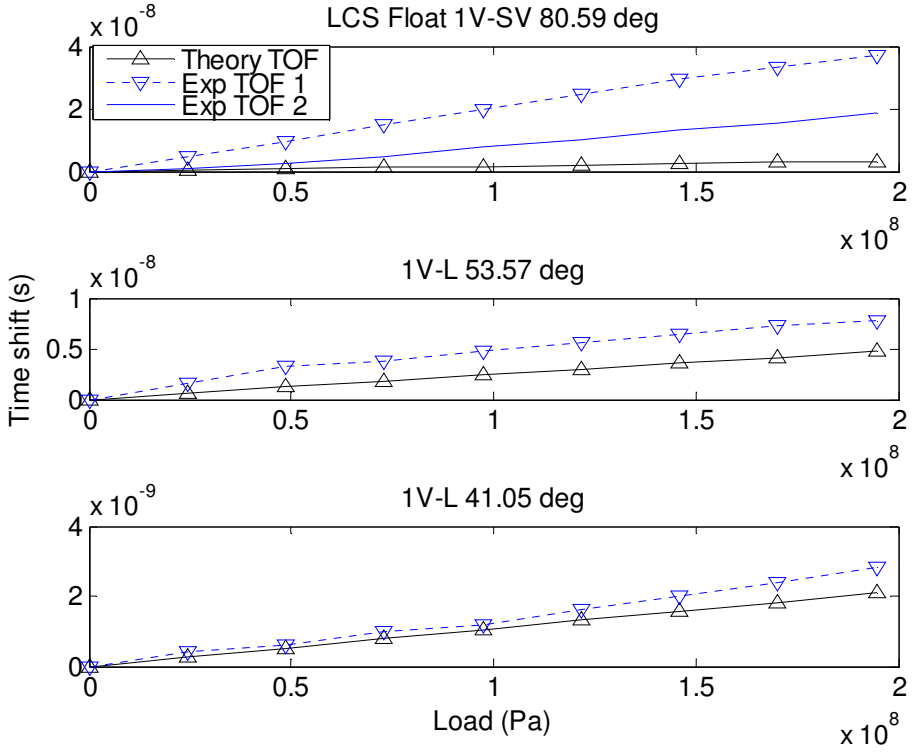

Figure 7.9. Floating 2L+1SV time shift vs. load curves for low carbon steel with single V paths.

7.1.2 Endpoint Loading Method

Most of the data recorded for the endpoint loading method were from the 7075-T6 aluminum coupon with a thickness of 6.26 mm and a width of 76.3 mm (see Table 7.1 for all parameters). The maximum applied stress was 194 MPa, which is well below the yield strength such there is no plastic deformation. As previously described, a total of nine waveforms were recorded for each measurement repetition, and measurements were repeated five times. Data are shown in Figure 7.10. The points labeled "Loading Times" were recorded between the zero point and the next maximum load point, and those labeled "Unloading Times" were recorded between the maximum load point and the next zero point. The time shift values used for further computations are those taken during unloading ("Unloading Times") since this data proved to be more consistent than the data taken during loading. Wedges were removed and reclamped after each repetition.

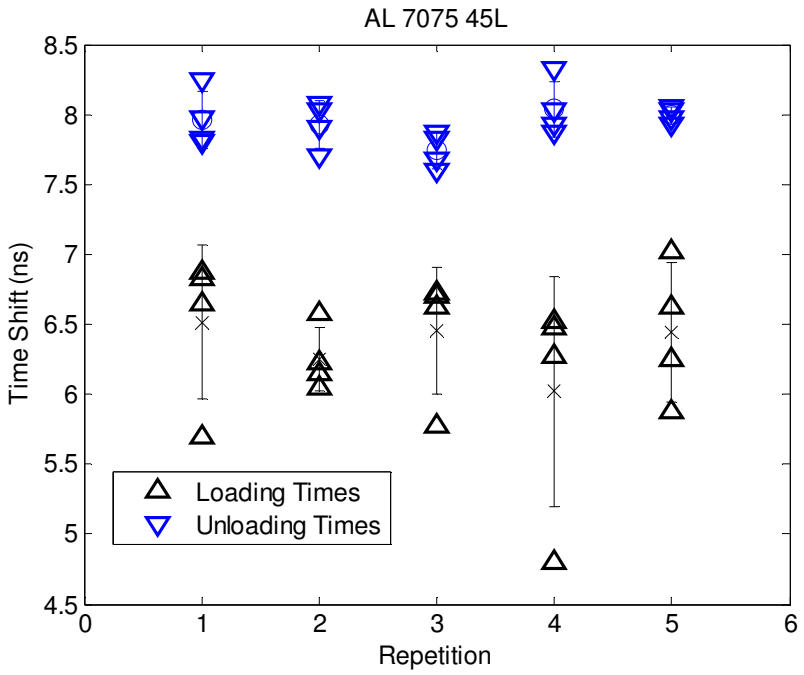

Figure 7.10. Data from the 45L floating wedge pair on aluminum 7075-T6 sample for five repetitions.

Table 7.3 gives details of the forward problem time shift data for 7075-T6 aluminum, 7075-T651 aluminum, and 2024 aluminum. Experimental values reported are the total time shift in time-of-flight data between a maximum applied stress of 194MPa and a zero load reference point. The reported mean is the average of four measurement cycles. Each 2L+2SV set can yield two sets of TOECs. The theoretical time shifts are calculated from data in Table 4 3.

Table 7.3. 2L+1SV time shift data obtained with the endpoint loading method.

Material	Wave Type Ref Angle	Transducer Separation (mm)	Experimental Time Shift (ns)	
			Mean	StdDev
AL7075-T6	70SV 60L 45L 45SV	34.418	28.185	0.415
		21.697	24.105	0.251
		12.527	7.933	0.177
		12.527	21.831	0.241
	70SV 60L 45L 45SV	34.418	28.479	0.282
		21.697	23.302	0.562
		12.527	7.401	0.301
		12.527	21.631	0.357
	70SV 60L 45L 45SV	34.418	27.657	0.293
		21.697	24.101	0.235
		12.527	7.222	0.261
		12.527	21.829	0.289
AL7075-T651	70SV 60L 45L 45L 45SV	33.849	50.541	0.392
		21.339	30.417	0.579
		12.320	11.381	0.715
		12.320	10.415	0.935
		12.320	16.889	0.363
AL2024	70SV 60L 45L 45SV	34.948	24.966	0.329
		22.032	23.208	0.394
		12.720	5.310	0.839
		12.720	19.915	0.325

7.2 1L+1SV+1SH Forward Problem Results using Endpoint Loading Method

Numerical results shown in Chapter 4 indicated that the 1L+1SV+1SH offered the lowest uncertainty for the recovery of TOECs. Thus, a measurement was added using a 45 degree SH wave floating wedge that is described in Section 5.7.2. Measurement results are shown in Table 7.4 for 7075-T6 aluminum, 7075-T651 aluminum and 2024 aluminum using this configuration which involved one SH refracted shear wave set of measurements. This configuration using shear wave transducers was also used to make 45 degree SV measurements by rotating the transducer 90 degrees on the back of the wedge, and these measurements are used as an independent check of prior 45 degree SV measurements made using longitudinal mode transducers and refracted angle wedges. The remaining L and SV data shown in Table 7.4, not bolded, are the same as the values reported in the previous section.

Table 7.4. 1L+1SV+1SH time shift data obtained with the endpoint loading method.

Material	Wave Type Ref Angle	Transducer Separation (mm)	Experimental Time Shift (ns)	
			Mean	StdDev
AL7075-T6	70SV 60L 45L 45SV **45SV 45SH 45SH**	34.418	28.185	0.415
		21.697	24.105	0.251
		12.527	7.933	0.177
		12.527	21.831	0.241
		12.700	**22.302**	**0.630**
		12.700	**-1.870**	**0.444**
		12.700	**-0.351**	**0.306**
	70SV 60L 45L 45SV **45SV 45SH 45SH**	34.418	28.479	0.282
		21.697	23.302	0.562
		12.527	7.401	0.301
		12.527	21.631	0.357
		12.700	**22.302**	**0.630**
		12.700	**-1.870**	**0.444**
		12.700	**-0.351**	**0.306**
	70SV 60L 45L 45SV **45SV 45SH 45SH**	34.418	27.657	0.293
		21.697	24.101	0.235
		12.527	7.222	0.261
		12.527	21.829	0.289
		12.700	**22.302**	**0.630**
		12.700	**-1.870**	**0.444**
		12.700	**-0.351**	**0.306**
AL7075-T651	70SV 60L 45L 45L 45SV **45SV 45SH**	33.849	50.541	0.392
		21.339	30.417	0.579
		12.320	11.381	0.715
		12.320	10.415	0.935
		12.320	16.889	0.363
		12.700	**16.658**	**1.560**
		12.700	**-5.721**	**0.477**
AL2024	70SV 60L 45L 45SV **45SV 45SH 45SH**	34.948	24.966	0.329
		22.032	23.208	0.394
		12.720	5.310	0.839
		12.720	19.915	0.325
		12.700	**19.506**	**0.204**
		12.700	**0.201**	**0.322**
		12.700	**-0.406**	**0.239**

7.3 2L+1SH Forward Problem Results using Endpoint Loading Method

The single SH measurement allows the recovery of TOECs via the 2L+1SH solution. The forward problem data is arranged for this solution in Table 7.5 for all three materials.

Table 7.5. 2L+1SH time shift data obtained with the endpoint loading method.

Material	Wave Type Ref Angle	Transducer Separation (mm)	Experimental Time Shift (ns)	
			Mean	StdDev
AL7075-T6	60L 45L **45SH** **45SH**	21.697	24.105	0.251
		12.527	7.933	0.177
		12.700	**-1.870**	**0.444**
		12.700	**-0.351**	**0.306**
	60L 45L **45SH** **45SH**	21.697	23.302	0.562
		12.527	7.401	0.301
		12.700	**-1.870**	**0.444**
		12.700	**-0.351**	**0.306**
	60L 45L **45SH** **45SH**	21.697	24.101	0.235
		12.527	7.222	0.261
		12.700	**-1.870**	**0.444**
		12.700	**-0.351**	**0.306**
AL7075-T651	60L 45L 45L **45SH**	21.339	30.417	0.579
		12.320	11.381	0.715
		12.320	10.415	0.935
		12.700	**-5.721**	**0.477**
AL2024	60L 45L **45SH** **45SH**	22.032	23.208	0.394
		12.720	5.310	0.839
		12.700	**0.201**	**0.322**
		12.700	**-0.406**	**0.239**

7.4 TOECs Recovered from the 2L+1SV Configuration

Most of the experiments performed utilized the 2L+1SV configuration. Results are presented for the floating case using both loading approaches.

7.4.1 Incremental Loading Method

The incremental loading method was done for both single and multiple V path configurations. Table 7.6 summarizes recovered TOECs for three materials utilizing the 2L+1SV solution.

Table 7.6. 2L+1SV experimental TOECs recovered using the incremental loading method.

Material	VPath & Refracted Ang	Experimental TOECs recovered		
		l	***m***	***n***
AL7075-T6	2V-SV (60) 2V-L (60) 3V-L (50)	-561.92	-232.81	-464.15
	2V-SV (71) 2V-SV (46) 2V-L (58) 3V-L (44)	-332.17 -332.17	-276.86 -276.86	-351.42 -376.43
	1V-SV (45) 1V-SV (70) 1V-L (60) 1V-L (45)	-312.90 -312.90	-303.41 -303.41	-418.55 -499.67
AL7075-T651	2V-SV (46) 2V-L (58) 3V-L (44)	-728.20	-103.37	-654.18
	1V-SV (70) 1V-SV (45) 1V-L (60) 1V-L (45)	-919.20 -919.20	-115.40 -115.40	-826.10 -809.16
AL2024	2V-SV (46) 2V-L (58) 3V-L (44)	-491.92	-283.75	-526.64
Low Carbon Steel	2V-SV (48) 2V-L (54) 3V-L (41)	-615.57	-716.60	433.02
	1V-SV (81) 1V-SV (48) 1V-L (54) 1V-L (41)	-96.99 -96.99	-918.57 -918.57	945.44 -490.62

7.4.2 Endpoint Loading Method

Only single V path arrangements were used in the second loading approach for TOEC recovery. TOECs resulting from the 2L+1SV time shift measurements shown in

Section 7.1.2 are presented in Table 7.6 for 7075-T6, 7075-T651 and 2024 aluminum. The wedge pairs were removed and reclamped after each cycle and the individual measurements were averaged to obtain the time shift waves listed in Table 7.7. The wedge pairs are constructed with a transducer separation suitable for a thickness of 6.26mm, whereas the thickness of the specimens varies somewhat.

Table 7.7. 2L+1SV experimental TOECs recovered using the endpoint loading method.

Material	Wave Type Ref Angle	Time shift (ns)	TOECs (GPa)		
			l	***m***	***n***
AL7075-T6	70SV	28.185	-65.19 -65.19	-292.60 -292.60	-294.22 -334.54
	60L	24.105			
	45L	7.933			
	45SV	21.831			
	70SV	28.479	-44.48 -44.48	-291.86 -291.86	-298.41 -332.02
	60L	23.302			
	45L	7.401			
	45SV	21.631			
	70SV	27.657	-6.26 -6.26	-306.97 -306.97	-61.45 -306.73
	60L	24.101			
	45L	7.222			
	45SV	21.829			
AL7075-T651	70SV	50.541	-142.89 -80.53	-264.04 -279.10	-330.95 -301.87
	60L	30.417			
	45L	11.381			
	45L	10.415			
	45SV	16.889			
AL2024	70SV	24.966	150.01 150.01	-364.24 -364.24	-226.09 -179.04
	60L	23.208			
	45L	5.310			
	45SV	19.915			

7.5 TOECs Recovered from the 1L+1SV+1SH Configuration

The 1L+1SV+1SH configuration uses a single 45 SH measurement combined with previous L and SV time shift data. Recovered TOECs are shown in Table 7.8. This combination leads to the recovery of four sets of TOEC data in each trial for all three materials.

Table 7.8. 1L+1SV+1SH experimental TOECs recovered using the endpoint loading method.

Material	1L+1SV+1SH			TOECs (GPa)		
	L	**SV**	**SH**	***l***	***m***	***n***
AL7075-T6	45	45	45	-57.49	-296.37	-327.24
	45	70	45	-78.27	-286.16	-306.62
	60	45	45	-49.73	-296.37	-327.24
	60	70	45	-91.46	-286.16	-306.62
	45	45	45	-37.33	-295.37	-325.24
	45	70	45	-54.64	-286.87	-308.05
	60	45	45	-30.11	-295.37	-325.24
	60	70	45	-64.89	-286.87	-308.05
	45	45	45	-27.86	-296.36	-327.22
	45	70	45	-51.19	-284.90	-304.06
	60	45	45	-49.66	-296.36	-327.22
	60	70	45	-96.52	-284.90	-304.06
AL7075-T651	45	45	45	-221.34	-231.96	-277.23
	45	70	45	-99.10	-292.00	-395.20
	60	45	45	-289.48	-231.96	-277.23
	60	70	45	-43.97	-292.00	-395.20
AL2024	45	45	45	41.24	-309.96	-329.24
	45	70	45	17.25	-298.13	-305.89
	60	45	45	-67.35	-309.96	-329.24
	60	70	45	-115.50	-298.13	-305.89

7.6 TOECs Recovered from the 2L+1SH Configuration

TOECs recovered using the time shift data in Section 7.3 are shown in Table 7.9 for the 2L+1SH solution for all three aluminum alloys studied.

Table 7.9. 2L+1SH experimental TOECs recovered using the endpoint loading method.

Material	Wave Type Ref Angle	Time shift (ns)	TOECs (GPa)		
			l	***m***	***n***
AL7075-T6	60L	24.105	-65.19 -65.19	-292.59 -292.59	-319.60 -350.55
	45L	7.933			
	45SH	-0.351			
	45SH	-1.870			
	60L	23.302	-44.48 -44.48	-291.86 -291.86	-318.13 -349.08
	45L	7.401			
	45SH	-0.351			
	45SH	-1.870			
	60L	24.101	-6.26 -6.26	-306.97 -306.97	-348.66 -379.61
	45L	7.222			
	45SH	-0.351			
	45SH	-1.870			
AL7075-T651	60L	30.417	-142.90 -80.67	-263.70 -278.73	-348.28 -379.74
	45L	11.381			
	45L	10.415			
	45SH	-5.721			
AL2024	60L	23.208	149.10 149.10	-363.15 -363.15	-446.92 -442.36
	45L	5.310			
	45SH	-0.406			
	45SH	0.201			

7.7 Section Summary

Three well-posed solutions have being used to recover TOECs for several aluminum alloys using two loading approaches and different V path arrangements. Forward problem results were presented at the start of the chapter where theoretical values are calculated using published data and assumptions are made that materials tested are the same as those published. Overall the TOECs recovered are in agreement with the general guidelines for TOECs. Trends which appeared in the sensitivity analysis have being verified experimentally.

CHAPTER 8

DISCUSSION

In this chapter, the major results of the research are summarized and reviewed. These results include procedures developed for one-sided TOEC recovery and the recovery of TOECs for specific materials. This work provides a comprehensive foundation for the development of one-sided contact techniques for TOEC recovery. Limitations of the present work are the requirement of a backwall, smooth parallel faced specimen.

8.1 Review of Development Procedure

Acoustoelasticity theory has been extended and developed for a one-sided approach to TOEC recovery. The solution proposed here for the inverse problem is deterministic in that three measurements are required to determine the three acoustoelastic constants. The solution for all well-posed problems leading to the recovery of TOECs for isotropic materials was verified numerically and three of these solutions 2L+1SV, 2L+1SH and 1L+1SV+1SH were investigated experimentally.

Two measurement approaches were used during testing to measure time-of-flight changes as a function of applied loads. The first was the incremental loading method and the second was the endpoint loading method, and both are described in Section 5.3. The second loading method was developed in an attempt to make more consistent measurements. Repeatability of the procedure was assessed by making the same measurements repeatedly on the same specimen. Transducers were removed and replaced each time over a set of five trials.

In developing the theory, time shift equations were derived in both the initial and natural system and were used to cross check each other and verify theory. Any differences though small were accounted for along with any linearization errors in the recovery of TOECs. In this angle beam work 0 and 90 degrees are viewed as special cases and equations reduce to traditional equations by Hughes and Kelly in the literature. A series of ultrasonic measurements was conducted on several aluminum alloys with the measurement system described in Chapter 5. The existing system involves manual load control, however more reliable measurements were obtained when using the second loading approach, i.e., end point load method.

The 2L+1SV test configuration was mostly used throughout this work because of the initial availability of wedges. Upon completion of the numerical sensitivity study, it was noted that this configuration has the highest uncertainty for both the attached and floating cases, and that TOEC recovery results could be improved through additional tests with other wave mode (i.e., SH waves) and refracted angle choices. Trends seen in the numerical exercise were confirmed experimentally with the largest scatter being observed for *l* and lowest scatter for *m*.

The 1L+1SV+1SH solution was tried experimentally in the floating case with a single V path arrangement. This solution offers the best uncertainty from the numerical exercises. A single SH measurement was performed and combined with previous L and SV measurements. The experimental results of this solution partially confirmed that any angle can be used as there was less scatter for TOECs for AL7075-T6 reported in Table 7.8 as compared to those reported in Tables 7.7 and 7.9 for the other configurations.

Furthermore, TOECs recovered for 7075-T6 aluminum with this configuration are in reasonable agreement with published values.

The 2L+1SH solution was also investigated by combining the SH measurement with two previous L wave measurements. SH measurements were confirmed by making additional SV measurements with the same wedge block by rotating shear transducers by 90 degrees. This additional data is then compared to previous SV time shifts at the same refracted angle. TOECs recovered for 7075-T6 aluminum for this configuration are also in reasonable agreement with published values.

Table 7.6, which is for the 2L+1SV configuration with the incremental loading methods, shows instances where l values swing positive. This can be explained due to the large uncertainty associated with the l TOEC and is expected if accuracy isn't consistent on L wave time shift measurements. Overall total time shifts are small and were found to be smaller in steel than aluminum, time shifts for the attached case are larger than the corresponding floating case. All of these trends are expected from theory using published values for TOECs for 7075-T6 aluminum.

A major drawback of the attached wedge approach is the acoustoelastic effect experienced in the wedges when they are glued to the sample. For damage tracking applications, the absolute value are not as important as the relative values and more work needs to be done to possibly isolate this effect and apply the technique in the context of structural health monitoring.

For a direct comparison of methods based on tests done in this research, refer to Table 8.1. For 7075-T6 aluminum, the three best sets of constants for the floating case are averaged and compared to the single attached result. Overall the average value for the

floating case is closer to that realized in a recent characterization using traditional methods [44]. This comparison is not conclusive since more attached tests are required to support this experimentally.

Table 8.1. Summary of recovered TOECs for 7075-T6 aluminum.

Method	Solution	TOECs			Average TOECs		
		l	***m***	***n***	***l***	***m***	***n***
Floating	2L+1SV	-65.19	-292.60	-334.54	-80.85	-288.75	-319.40
	2L+1SH	-65.19	-292.59	-319.60			
	1L+1SV+1SH	-96.52	-284.90	-304.06			
Attached	2L+1SV	-597.3	-208.8	-517.7	-597.3	-208.8	-517.7

8.2 Evaluation of Numerical Exercises

The main categories in the sensitivity analysis were time shifts, geometrical parameters, material properties and load. This exercise showed that the major factors which affect the sensitivity of the TOECs obtained are the transducer separations and time shifts. The effect of small errors in time shift measurements can change TOECs dramatically. The accuracy of the measurement setup to account for transducer separation is estimated at ±0.5 mm. Use of this value in the sensitivity analysis of Chapter 4 showed the need for closer tolerances on separation distances. Differences in material properties for the aluminum alloys used here compared to those of quoted literature sources probably also contributes to differences in reported TOEC values.

Experimental exercises used single and multiple V paths, though a numerical exercise showed that multiple V paths reduced uncertainty. However, a single V path was used where possible because echoes from various wave modes were easier to distinguish compared to multiple V path signals.

Numerical exercises and theory developed did not account for off axis propagation. However, care was taken to assure that the beam path was along the loading direction for all tests conducted.

The sensitivity analysis indicates that additional L measurements may be needed to reduce the uncertainty in *l*, which would reduce the effect of measurement errors at the expense of experimental complexity. The best well-posed configuration is the floating 1L+1SV+1SH where it was shown that any angle combination can be used.

Mention must be made of the refracted angle choices to avoid in the case of the 2L+1SV, 2L+1SH and 2SH+1L test configurations. The general approach is to specify refracted angle values for the same wave mode as far apart as physically possible.

The numerical sensitivity analysis showed the importance of selecting the best angles and solution for TOEC recovery, and the numerical results confirm the validity and self consistency of the proposed procedure of determining TOECs from load dependent time shifts.

8.3 Review of TOECs Recovered

Many of the forward problem time shifts shown in Chapters 6 and 7 for both the attached and floating cases are in reasonable agreement with those calculated using literature TOEC values for samples included, and TOECs recovered using these time shift values are also in reasonable agreement. This is illustrated in Table 8.2 and Figure 8.1 for the floating case where the best TOECs recovered for 7075 aluminum in this work are shown and compared to other published values.

Table 8.2. Summary of experimentally determined TOECs and literature values.

TOEC	Present Work AL7075 (GPa)	Stobbe AL7075 (GPa)	Dubuget AL7075 (GPa)	Dubuget AL7010 (GPa)	Smith AL 2S (GPa)
l	-65.2	-252.2	-126 ± 15	-103 ± 15	-311
m	-292.6	-325.0	-320 ± 10	-279 ± 10	-401
n	-334.5	-351.2	-282 ± 6	-333 ± 6	-408

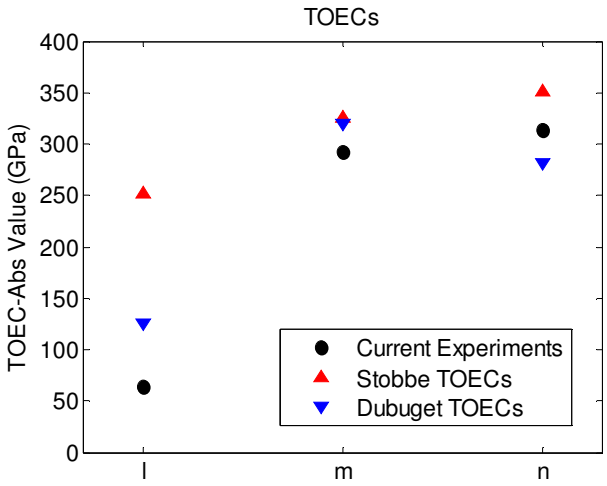

Figure 8.1. Recovered TOECs, floating 2L+1SV compared to literature values.

Figure 8.2 shows measured time shifts compared to those calculated using TOECs for 7075 reported by Stobbe [44] and Dubuget et al. [55]. The trends of the time shifts are in good agreement, although the measured values are smaller than the calculated ones except for the 45° shear vertical wave configuration. Note that there is considerably more scatter in the values for *l* compared to *m* and *n* for all solutions. Results in Table 8.2 show that the value of *l* from this work is lower than the other two reported values. This is consistent with the sensitivity analysis showing that *l* has the largest uncertainty, which is in agreement with [55].

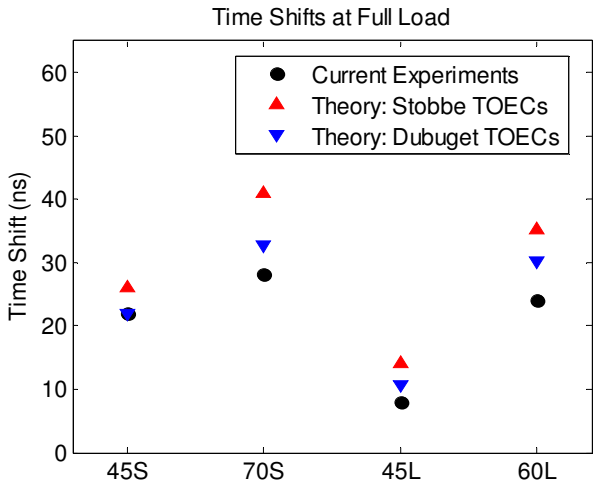

Figure 8.2. Time shift floating 2L+1SV data compared to those calculated from literature values of TOECs at maximum load.

For verification and validation of results, at a minimum, constants reported are the same order of magnitude as those published for materials involved and are an order higher than SOECs. The results also fulfill the general TOEC criteria where $C_{ijk} < 0$. Cernoch [29] states an additional criterion of $C_{111} < C_{112} < C_{123}$. Based on TOEC relationships between the Brugger and Murnaghan constants, the Murnaghan equivalent is $(l + 2m) < l < (l - m + n/2)$. Table 8.3 gives a summary of the best TOECs recovered and results of checking with the criteria above.

Table 8.3. General criteria test of AL7075 TOECs recovered

Method	**Solution**	**TOECs**			**General Criteria**	
		l	***m***	***n***	$C_{ijk}<0$	$l+2m<l<l-m+n/2$
Floating	2L+1SV	-65.19	-292.60	-334.54	met	met
	2L+1SH	-65.19	-292.59	-319.60	met	met
	1L+1SV+1SH	-96.52	-284.90	-304.06	met	met
Attached	2L+1SV	-597.30	-208.80	-517.70	met	**not met**

The sensitivity analysis shows that all of the resulting TOECs are very sensitive to errors in the L wave time shifts and separation distances; at times the uncertainty in l is similar in magnitude to l itself. The analysis also confirms that only n has errors due to the SV time shift and separation distance because the two L-wave measurements are sufficient to perfectly recover l and m in the 2L+1SV and 2L+1SH solutions.

The attached method yielded TOECs for two materials, however the results are not in close agreement to the literature values provided they are the same alloys, and furthermore data were not repeatable.

CHAPTER 9

CONCLUSIONS AND FUTURE WORK

9.1 Conclusions

The research objective was to develop theory and provide implementation for a new one-sided angle-beam ultrasonic method for measuring TOECs of a homogeneous, isotropic material using the acoustoelastic effect. From the research conducted it can be concluded that angle beam methods are viable for measuring TOECs.

Two transducer configurations were considered: (1) attached (glued-on) transducers suitable for in situ monitoring, and (2) floating (oil-coupled) transducers suitable for single measurements. A detailed sensitivity analysis was carried out and the best configuration, wave mode combinations and geometry was selected to be the floating 1L+1SV+1SH. The use of this solution permits the use of any refracted angle combination.

There are significant experimental issues that have being partially addressed in this thesis. More work is required as some of the challenges included developing repeatable techniques for measuring transducer spacing and acquiring time shift data. Another factor is that very careful measurements are required since the acoustoelastic effect is typically very small, which results in small time shifts under externally applied loads.

Results were verified by comparing the measured TOECs to published values from other techniques for several materials. These results fulfilled the general criteria for TOECs and are in reasonable agreement with the literature.

General theory has been developed for relating sets of measured bulk wave acoustoelastic constants of a homogeneous, isotropic material to TOECs where the direction of propagation is at an angle to the loading direction. This theory yielded four well-posed solutions, and three have been experimentally applied, namely the 2L+1SV, 2L+1SH and 1L+1SV+1SH wave mode combinations. Both the forward and inverse problems have been considered, where the forward problem is to calculate measured time shifts given the TOECs, and the inverse problem is to calculate the TOECs from the measured time shifts, i.e., recovery of TOECs from measurement time shift data.

Solution to this inverse problem involved making some linearization assumptions and any small errors due to this assumption have been evaluated. Generally, these linearization errors are much less than the variability in reported TOEC values.

One use of TOEC measurements is the tracking of damage progression during metal fatigue, for which reliably tracking changes in TOEC values is more important than the actual TOEC values. In this context the linearization assumptions made in the inverse problem solution are of little consequence. However, it is critically important to take careful, repeatable measurements. This is compounded by the fact that the nonlinear effect is small for some materials.

9.2 Recommendations for Future Work

The background review coupled with this work has provided insight to the challenges faced in making acoustoelasticity measurements. Data is generally lacking on TOEC values for many materials and there is usually considerable uncertainty in parameters that are reported. There is also uncertainty regarding the reported uncertainty because there are no published results that include an uncertainty analysis. Thus,

continued development of the one-sided method is recommended to improve measurement accuracy so that a robust method will be available for determining TOEC values. To accomplish this goal, some recommendations for future work include:

1. Extension of the theory developed here to off angle propagation directions, with respect to the loading direction.
2. An additional SH measurement would enable investigation of the 1L + 2SH solution for completeness of the well-posed solutions presented in this thesis. Once complete, then a search for the optimum number of measurements in an over determined scenario could be addressed.
3. Additional measurements would be useful on well characterized materials with respect to microstructure, dislocation density, etc. This would be an important step in reducing variability of reported TOEC values. Earlier work reports that aluminum has a strong dependence with rolling direction for TOEC values.
4. Tedious measurements can be expedited by making multiple mode measurements simultaneously from multi-configuration wedge assemblies loaded in a tensile testing machine. The use of a tensile testing machine will answer the question about the effect of loading and unloading times.
5. Extend the testing to other engineering materials and conduct tests to track TOEC changes with damage progression during fatigue loading.
6. Develop methods to control and measure the actual thickness of the couplant layer between the wedge and the specimen. This will probably involve the use of multimode wedges that can be attached repeatable with a very consistent, minimal clamping force.

7. Develop the one-sided TOEC measurement method for use in structural health monitoring applications. The challenge will be finding wedge materials and adhesives that will not mask or cause severe variations in the nonlinear effects being measured.

In summary, although the theory for a one-sided contact angle-beam method for determining TOECs is developed, experimental techniques are the limiting factor and future work must concentrate on improving accuracy and reliability of the overall measurement process.

REFERENCES

[1] S. Sathish, J. Frouin, and J. K. Na, "Early Detection of Fatigue Damage in Ti-6Al-4V with Nonlinear Acoustics," *Heidelberg, Springer-Verlag Berlin Heidelberg,* 2004.

[2] A. G. Every and W. Sachse, "Determination of the elastic constants of anisotropic solids from acoustic-wave group-velocity measurements," *Physical Review B (Condensed Matter),* vol. 42, pp. 8196-205, 1990.

[3] J. Krautkramer and H. Krautkramer, *Ultrasonic Testing of Materials*: Berlin; New York : Springer-Verlag, 1983.

[4] R. B. Thompson and D. O. Thompson, "Ultrasonics in nondestructive evaluation," *Proceedings of the IEEE,* vol. 73, pp. 1716-55, 1985.

[5] J. D. Achenbach, *Wave Propagation in Elastic Solids*, 1st ed.: North Holland, 1975.

[6] J. L. Rose, *Ultrasonic Waves in Solid Media*. Cambridge UK: Cambridge University Press, 1999.

[7] J. H. Cantrell, "Fundamentals and applications of nonlinear ultrasonic nondestructive evaluation," in *Ultrasonic Nondestructive Evaluation*, T. Kundu, Ed.: CRC Press, 2004.

[8] K. E. A. Van Den Abeele, A. Sutin, J. Carmeliet, and P. A. Johnson, "Micro-damage diagnostics using nonlinear elastic wave spectroscopy (NEWS)," *NDT and E International,* vol. 34, pp. 239-248, 2001.

[9] J. H. Cantrell and W. T. Yost, "Nonlinear ultrasonic characterization of fatigue microstructures," in *International Journal of Fatigue*, Hyannis, MA, USA, 2001, pp. 487-490.

[10] J.-Y. Kim, L. J. Jacobs, J. Qu, and J. W. Littles, "Experimental characterization of fatigue damage in a nickel-base superalloy using nonlinear ultrasonic waves," *Journal of the Acoustical Society of America,* vol. 120, pp. 1266-1273, 2006.

[11] T. Suzuki, A. Hikata, and C. Elbaum, "Anharmonicity due to glide motion of dislocations," *Journal of Applied Physics,* vol. 35, p. 2761, 1964.

[12] A. Hikata, B. B. Chick, and C. Elbaum, "Effect of dislocations on finite amplitude ultrasonic waves in aluminum," *Applied Physics Letters,* vol. 3, 1963.

[13] M. A. Biot, "Influence of initial stress on elastic waves," *Journal of Applied Physics,* vol. 11, pp. 522-528, 1940.

[14] F. Lingvall, P. Wu, and T. Stepinski, "Inspection of copper canisters for spent nuclear fuel by means of ultrasound nonlinear acoustics, synthetic aperture imaging," Technical Report, Uppsala University, Stockholm, Sweden 2003.

[15] A. N. Norris, "Finite amplitude waves in solids," in *Nonlinear Acoustics*, M. F. Hamilton and D. T. Blackstock, Eds.: Academic Press, New York, 1998, pp. 263-277.

[16] S. Suresh, *Fatigue of Materials*, 2 ed.: Cambridge University Press, 1998.

[17] D. S. Drumheller, *Introduction to Wave Propagation in Nonlinear Fluids and Solids*. Camridge, UK: Cambridge University Press, 1998.

[18] P. B. Nagy, "Fatigue damage assessment by nonlinear ultrasonic material characterization," *Ultrasonics,* vol. 36, pp. 375-381, 1998.
[19] H. Yang, W. T. Yost, and J. H. Cantrell, "Effect of aging on the third-order elastic moduli of 18 Ni maraging steel," Denver, CO, USA, 1987, pp. 1131-1135.
[20] J. H. Cantrell and K. Salama, "Acoustoelastic characterisation of materials," *International Materials Reviews,* vol. 36, pp. 125-145, 1991.
[21] D. I. Crecraft, "The measurement of applied and residual stresses in metals using ultrasonic waves," *Journal of Sound and Vibration,* vol. 5, pp. 173-192, 1967.
[22] R. R. Rao and A. Padmaja, "Effective second-order elastic constants of a strained cubic crystal in the finite strain theory," *Journal of Applied Physics,* vol. 64, pp. 3320-3322, 1988.
[23] D. I. Crecraft, "The use of ultrasonics in stress analysis," *Strain,* vol. 1, pp. 4-8, 1965.
[24] R. A. Toupin and B. Bernstein, "Sound waves in deformed perfectly elastic materials. Acoustoelastic effect," *Journal of the Acoustical Society of America,* vol. 33, pp. 216-225, 1961.
[25] P. L. Gould, *Introduction to Linear Elasticity*: Springer Verlag, 1994.
[26] L. E. Malvern, *Introduction to the Mechanics of a Continuum Medium*. Englewood Cliffs, NJ: Prentice-Hall, 1969.
[27] K. Brugger, "Thermodynamic Definition of Higher Order Elastic Coefficients," *Physical Review,* vol. 133, p. A1611, 1964.
[28] K. P. Jayachandran and C. S. Menon, "Third-order elastic constants of the high temperature superconductor Bi2Sr2CaCu2O8," *Journal of Physics and Chemistry of Solids,* vol. 60, pp. 267-271, 1999.
[29] T. Cernoch, M. Landa, V. Novak, P. Sedlak, and P. Sittner, "Acoustic characterization of the elastic properties of austenite phase and martensitic transformations in CuAlNi shape memory alloy," *Journal of Alloys and Compounds,* vol. 378, pp. 140-144, 2004.
[30] L. G. Hwa, Y. J. Wu, W. C. Chao, and C. H. Chen, "Pressure- and temperature-dependence of elastic properties of a ZBLAN glass," *Materials Chemistry and Physics,* vol. 74, pp. 160-166, 2002.
[31] D. S. Hughes and J. L. Kelly, "Second-order elastic deformation of solids," *Physical Review,* vol. 92, pp. 1145-1149, 1953.
[32] F. D. Murnaghan, *Finite Deformation of an Elastic Solid* John Wiley & Sons, Inc., 1951.
[33] R. N. Thurston and K. Brugger, "Third-order elastic constants and the velocity of small amplitude elastic waves in homogeneously stressed media," *Physical Review,* vol. 133, pp. A1604-A1610, 1964.
[34] H. J. McSkimin, "Pulse superposition method for measuring ultrasonic wave velocities in solids," *Journal of the Acoustical Society of America,* vol. 33, pp. 12-16, 1961.
[35] D. I. Crecraft, "Ultrasonic wave velocities in stressed nickel steel," *Nature,* vol. 195, pp. 1193-1194, 1962.
[36] M. Sgalla and D. Vangi, "UCRfr--ultrasonic critical-angle refractometry for stress measurement," *Nondestructive Testing & Evaluation,* vol. 19, pp. 67-77, 2003.

[37] M. Janssen, "Reproducible time-of-flight measurements with a piezoelectric transducer for acoustoelastic stress evaluation," *Experimental Mechanics,* vol. 35, pp. 266-71, 1995.
[38] B. Mi, J. E. Michaels, and T. E. Michaels, "An ultrasonic method for dynamic monitoring of fatigue crack initiation and growth," *Journal of the Acoustical Society of America,* vol. 119, pp. 74-85, 2006.
[39] X. H. Min and H. Kato, "Change in ultrasonic parameters with loading/unloading process in cyclic loading of aluminium alloy," *Materials Science & Engineering A (Structural Materials: Properties, Microstructure and Processing),* vol. A372, pp. 269-277, 2004.
[40] B. O'Neill and R. G. Maev, "Acousto-elastic measurement of the fatigue damage in Waspaloy," *Research in Nondestructive Evaluation,* vol. 17, pp. 121-135, 2006.
[41] E. H. Bogardus, "Third-order elastic constants of Ge, MgO and fused silica," *Journal of Applied Physics,* vol. 36, pp. 2504-2513, 1965.
[42] R. T. Smith, R. Stern, and R. W. B. Stephens, "Third-order elastic moduli of polycrystalline metals from ultrasonic velocity measurements," *Journal of the Acoustical Society of America,* vol. 40, pp. 1002-1008, 1966.
[43] D. M. Egle and D. E. Bray, "Measurement of acoustoelastic and third-order elastic constants for rail steel," *Journal of the Acoustical Society of America,* vol. 60, pp. 741-744, 1976.
[44] D. M. Stobbe, "Acoustoelasticity in 7075-T651 Aluminum and Dependence of Third Order Elastic Constants on Fatigue Damage" Masters Thesis," Georgia Institute of Technology, 2005.
[45] M. Kato, T. Sato, and K. Ando, "Determination of the higher-order elastic compliance constants of metals from measurements of the dependence of ultrasound velocity on stress," *Journal of the Acoustical Society of America,* vol. 101, pp. 2111-2121, 1997.
[46] Y.-H. Pao, W. Sachse, and H. Fukuoka, "Acoustoelasticity and ultrasonic measurements of residual stress," in *Physical Acoustics*. vol. XVII, W. P. Mason and R. N. Thurston, Eds. New York: Academic Press, 1984, pp. 1-143.
[47] R. W. Benson and V. J. Raelson, "Acoustoelasticity," *Product Engineering,* vol. 30, pp. 56-59, 1959.
[48] T. Tokuoka and Y. Iwashimizu, "Acoustical birefringence of ultrasonic waves in deformed isotropic elastic materials," *International Journal of Solids and Structures,* vol. 4, pp. 383-389, 1968.
[49] R. H. Bergman and R. A. Shahbender, "Effect of statically applied stresses on the velocity of propagation of ultrasonic waves," *Journal of Applied Physics,* vol. 29, pp. 1736-1738, 1958.
[50] G. C. Johnson, A. C. Holt, and B. Cunningham, "Ultrasonic Method for Determining Axial Stress in Bolts," *Journal of Testing & Evaluation,* vol. 14, pp. 253-259, 1986.
[51] J. S. Heyman, "NDE in aerospace-requirements for science, sensors and sense," *IEEE Transactions on Ultrasonics, Ferroelectrics and Frequency Control,* vol. 36, pp. 581-6, 1989.

[52] Y. Iwashimizu and K. Kubomura, "Stress-induced rotation of polarization directions of elastic waves in slightly anisotropic materials," *International Journal of Solids and Structures,* vol. 9, pp. 99-114, 1973.
[53] H. R. Dorfi, H. R. Busby, and M. Janssen, "Acoustoelasticity: ultrasonic stress field reconstruction," *Experimental Mechanics,* vol. 36, pp. 325-332, 1996.
[54] N. N. Hsu, "Acoustical birefringence and the use of ultrasonic waves for experimental stress analysis," Los Angeles, CA, USA, 1974, pp. 169-176.
[55] M. Dubuget, R. El Guerjouma, S. Dubois, J. C. Baboux, and A. Vincent, "Characterization of the non-linear elastic properties of aluminium alloys using ultrasonic evaluation under load," in *Materials Science Forum*, Grenoble, France, 1996, pp. 951-956.
[56] A. Bouhadjera, "Determination of third order elastic constants using a simple ultrasonic apparatus," in *3rd World Congress on Ultrasonics* Paris, 2003.
[57] H. R. Dorfi, H. R. Busby, and M. Janssen, "Ultrasonic stress measurements based on the generalized acoustic ratio technique," *International Journal of Solids and Structures,* vol. 33, pp. 1157-1174, 1996.
[58] R. B. King and C. M. Fortunko, "Surface-residual-stress evaluation using horizontally polarized shear waves," *Journal of Applied Physics,* vol. 55, pp. 3978-3983, 1984.
[59] A. Sinaie, "An analytical approach to the oblique-incidence acoustoelasticity," Ph.D Thesis," University of Oklahoma, 1990.
[60] X. Zhao, "Experimental investigation of the separation of texture and residual stress induced anisotropy via oblique incidence acoustoelasticity," Ph.D Thesis," University of Oklahoma, 1994.
[61] D. E. Chimenti, "Guided waves in plates and their use in materials characterization," *Applied Mechanics Reviews,* vol. 50, pp. 247-284, 1997.
[62] T. Berruti, M. M. Gola, and G. A. D. Briggs, "Acoustoelastic measurements on aluminium alloy by means of a contact and a non-contact (LFB acoustic microscopy) technique," *Journal of the Acoustical Society of America,* vol. 103, pp. 1370-1376, 1998.
[63] Y.-C. Lee and S. H. Kuo, "A new point contact surface acoustic wave transducer for measurement of acoustoelastic effect of polymethylmethacrylate," *Ultrasonics, Ferroelectrics and Frequency Control, IEEE Transactions on,* vol. 51, pp. 114-120, 2004.
[64] E. Tanala, G. Bourse, M. Fremiot, and J. F. De Belleval, "Determination of near surface residual stresses on welded joints using ultrasonic methods," *NDT&E International,* vol. 28, pp. 83-88, 1995.
[65] D. Husson, "A perturbation theory for the acoustoelastic effect of surface waves," *Journal of Applied Physics,* vol. 57, pp. 1562-8, 1985.
[66] J. Qu and G. Liu, "Effects of residual stress on guided waves in layered media," in *Review of Progress in Quantitative Nondestructive Evaluation*, 1998, pp. 1635-1642.
[67] J. J. H. Parker, E. F. Kelly, and D. I. Bolef, "An ultrasonic-optical determination of the third order elastic constant c[sub 111] for NaCl single crystals," *Applied Physics Letters,* vol. 5, pp. 7-9, 1964.

[68] V. M. Mathew, C. S. Menon, and K. P. Jayachandran, "Third-order elastic constants and pressure derivatives of the second-order elastic constants of hexagonal boron nitride," *Journal of Materials Science,* vol. 37, pp. 5237-5240, 2002.
[69] F. W. Sheard, "Calculation of the thermal expansion of solids from the third-order elastic constants," *Philosophical Magazine,* vol. 3, pp. 1381-1390, 1958.
[70] B. E. Powell and M. J. Skove, "Relation between isothermal and mixed third-order elastic constants," *Journal of Applied Physics,* vol. 38, pp. 404-405, 1967.
[71] A. Briggs, *Acoustic Microscopy*. New York: Oxford University Press, 1992.
[72] R. B. Mignogna, A. V. Clark, B. B. Rath, and C. L. Vold, "Acoustic stress measurement in aluminum and steel considering differences in texture due to rolled plate thickness," Halifax, NS, Canada, 1983, pp. 201-6.
[73] M. A. Breazeale and J. Philip, "Determination of Third order elastic constants from Ultrasonic Harmonic Generation Measurements," in *Physical Acoustics*. vol. XVII, W. P. Mason and R. N. Thurston, Eds.: Academic Press, 1984, pp. 1-60.
[74] M. Duquennoy, M. Ouaftouh, M. Ourak, and F. Jenot, "Theoretical determination of Rayleigh wave acoustoelastic coefficients: Comparison with experimental values," *Ultrasonics,* vol. 39, pp. 575-583, 2002.
[75] W. T. Yost and M. A. Breazeale, "Ultrasonic nonlinearity parameters and third-order elastic constants of germanium between 300 and 77K," *Physical Review B (Solid State),* vol. 9, pp. 510-516, 1974.
[76] W. T. Yost and M. A. Breazeale, "Adiabatic third-order elastic constants of fused silica [u.s. wave measurement technique]," *Journal of Applied Physics,* vol. 44, pp. 1909-10, 1973.
[77] Y.-H. Pao and U. Gamer, "Acoustoelastic waves in orthotropic media," *Journal of the Acoustical Society of America,* vol. 77, pp. 806-12, 1985.
[78] H. Fukuoka and H. Toda, "Preliminary experiment on acoustoelasticity for stress analysis," *Archives of Mechanics,* vol. 29, pp. 673-86, 1977.